DEVELOPMENT OF COST-EFFECTIVE COMPONENTS FOR DYE-SENSITIZED SOLAR CELLS

Bakhytzhan Baptayev

A thesis submitted in partial fulfillment of the requirements of Nazarbayev University for the degree of Doctor of Philosophy

Supervisors: Dr. Mannix P. Balanay
Dr. Salimgerey Adilov
Prof. Niyazbek Ibrayev

February 2020

ABSTRACT

The commercialization of dye-sensitized solar cells (DSSCs) has been hindered by relatively low efficiency and comparatively high cost of the PV. Hence, further development of DSSC field heavily depends on the bringing down of its cost and improvement of its power converting efficiency. Therefore, we focused on the development of cost-effective methods and components for improving the power converting efficiency (PCE) of DSSCs. In our work we have demonstrated that it is possible to modify the photoanode by using a simple cost-effective technic of surface doping of TiO_2 via soaking the photoanode in 50 mM In^{3+} aqueous solution with acidic pH. Indium surface doping of TiO_2 film resulted in remarkable suppression of charge recombination and improvement of V_{OC} (from 0.77 V of the reference undoped TiO_2 sample to 0.80 V of In surface doped TiO_2 sample) leading to 18% efficiency increase. The overall result is comparable with bulk In doped TiO_2 solar cells and demonstrate effectiveness of surface doping technic. Moreover, we developed a new strategy of suppressing porphyrin dye aggregation in DSSCs which is based on axial complexation of central Zn metal of the porphyrin dyes with pyridine compounds via D-A bonding. This enables the use of long alkyl-chain free porphyrins that are economical and easier to synthesize compared to traditional analogs. Thus, a simple structured ZnP porphyrin dye axially coordinated with 4,4'-bipyridine ligand reduced dye aggregation on TiO_2 surface and led to over 40 % improvement of cell PCE compared to uncoordinated ZnP sensitized cell. Finally, we have prepared several novel Pt-free counter electrodes from less expensive materials like orange fiber derived carbon embedded cobalt sulfide nanoflakes (OFC@Co_xS_y-300) and ternary Cu-Co-S sulfides ($Cu_xCo_yS_z$-3 and $CuCo_2S_4$) which are prepared at lower temperature than Pt-based counter electrode. The developed new composite counter electrode OFC@Co_xS_y-300 based cell outperformed conventional Pt-based DSSCs by almost 7 % in power converting efficiency due to good electrocatalytic activity of the product. Solvothermally prepared ternary copper-cobalt-sulfides as $Cu_xCo_yS_z$-3 and nanostructured flower-shaped $CuCo_2S_4$ counter electrodes demonstrated better electrocatalytic activity than Pt CE leading to improved fill factor and photocurrent. Thus 11 % and 14 % enhancements in PCE compared to Pt-based DSSCs were observed in solar cells made of $Cu_xCo_yS_z$-3 and $CuCo_2S_4$, respectively. The $CuCo_2S_4$ CE demonstrated excellent stability during aging test for 1000 h.

TABLE OF CONTENTS

LIST OF TABLES

LIST OF FIGURES

LIST OF ABBREVIATIONS

1G	fisrt generation
2G	second generation
3G	third generation
AM	air mass
ASTM	American Society for Testing and Materials
BET	Brunauer-Emmett-Teller theory
BJH	Barrett-Joyner-Halenda theory
CB	conduction band
CDCA	chenodeoxycholic acid
CE	counter electrode
CIGS	copper indium gallium selenide
DFT	density functional theory
DMF	N, N-Dimethylformamide
DSSC	dye-sensitized solar cell
EDX	energy dispersive X-ray spectroscopy
EIS	electrical impedance spectroscopy
FE-SEM	field emission scanning electron microscope
FTIR	Fourier-transform infrared spectroscopy
FTO	fluorine-doped tin oxide
FWHM	full width at half maximum
HOMO	highest occupied molecular orbital
HR-XRD	high resolution X-ray diffraction
HTM	hole transporting material
IF	impact factor
ITO	indium tin oxide
LUMO	lowest unoccupied molecular orbital
MTNW	multi-layered TiO2 nanowires
NR	nanorod
NREL	National Renewable Energy Laboratory
NT	nanotube
NW	nanowire
OFC@Co_xS_y	orange fiber derived carbon embedded cobalt sulfide
OPV	organic photovoltaics
PANI	polyaniline

PEDOT	poly(3,4-ethylenedioxythiophene)
PPy	polypyrrole
PSC	perovskite solar cell
PSSC	porphyrin sensitized solar cell
PV	photovoltaic
QSC	quantum dot solar cells
QSS	quasi-solid state
SHE	standard hydrogen electrode
SSE	solid state electrolyte
TBP	tert-butylpyridine
TCO	transparent conducting oxide
TEM	transmission electron microscope
TGA	thermogravimetrical analysis
TPGE	thermoplastic gel electrolyte
UN	United Nations
XPS	X-ray photoelectron spectroscopy
XRD	X-ray diffraction

LIST OF SYMBOLS

A	acceptor
APCE	absorbed-photon-to-current conversion efficiency
d	film thickness
D	donor
D	crystallite size
E_{ads}	adsorption energy
$E_{complex}$	energy of complex
E_F	Fermi levels of the semiconductor in the light
E_{F0}	Fermi levels of the semiconductor in the dark
$E_{ferrocene}$	redox potential of ferrocene
E_g	band-gap energy
E_{ligand}	energies of detached ligand
E_{OX}	first oxidation potential onset
eV	electronvolt
E_{ZnP}	energies of detached porphyrin
F	Faraday constant
FF	fill factor
IPCE	incident-photon-to-current convertion efficiency
I-V	current-voltage relationship
J_0	exchange current density
J_{SC}	short-circuit current density
k	shape factor
kB	Boltzmann constant
L_e	diffusion length
LHE	light harvesting efficiency
mA	milliamps
mM	millimolar
n	number of electrons (or moles)
P_0	input power
PCE	power converting efficiency
P_{MP}	maximum produced power
q	electronic charge
Q	photoinduced charge density
R	universal gas constant

R_{CT}	charge transfer resistance
R_h	resistance of transparent conducting oxide (TCO) layer
R_S	series resistance
R_{Sh}	shunt resistance
R_{TiO2}	recombination resistance
R_W	Nernst diffusion resistance of electrolyte
T	absolute temperature
V	voltage (potential)
V_{OC}	open-circuit voltage
Z_{IMAG}	imaginary part of total impedance
Z_{REAL}	real part of total impedance
β	full width of peaks
ΔG_{inj}	electron injection energy
ΔG_{reg}	dye regeneration energy
η	power converting efficiency
θ	diffraction angle
λ	wavelength
τ_e	electron lifetime
ϕ_{cc}	charge collection efficiency
ϕ_{inj}	electron injection efficiency
ϕ_{reg}	dye regeneration efficiency
Φ_{SUN}	incident photon flux

ACKNOWLEDGEMENTS

All praises and thanks be to Allah Ar-Rahman Ar-Raheem for all of His blessings, especially giving me an opportunity to complete this work. Peace and blessings be to His Prophet Muhammad, his family, followers and to the reader.

I would like to express my gratitude to my supervisor Dr. Mannix P. Balanay who trained me from zero. I thank Dr. Balanay for willingness to share his knowledge and invaluable experience and for his time and patience.

My special thanks go to Dr. Salimgerey Adilov, my co-supervisor, for his kind support and priceless advices. I am deeply indebted to Dr. Adilov for it is him who invited me to the world of science and research. I would also like to extend my gratitude to Professor Niyazbek Ibrayev who agreed to co-supervise me for him being approachable.

I would like to acknowledge with deep thanks my reviewers for their time and patience. Professor Luis R. Rojas-Solorzano for his enormous effort put into PhD Program and for being accessible and helpful throughout my study.

Many thanks to our research group members. To Ainura Aukenova, Miras Kazaliyev, Dauren Kalpakov, Dias Mustazheb for their assistance.

Thanks should also go to my colleagues from National Laboratory Astana.

I very much appreciate the help of our collaborators from Trinity College Dublin, especially Ainur Zhussupbekova and her supervisor Prof. Karsten Fleischerin for helping with XPS analysis.

Words are powerless to express my love and gratitude to my dear Mother for her love, prayers and life-long support. God bless you Mom! I thank my beloved wife Zhanar who believed in me and fully supported me throughout this journey. Of course I thank my lovely daughters Inzhu, Sara and Safiya who when I show up at the front door late after long experiments welcome me with their angelic smiles, endless love and precious hugs. And all my relatives for their kind words of support.

DECLARATION

I declare that the research contained in this thesis, unless otherwise formally indicated within the text, is the original work of the author. The thesis has not been previously submitted to this or any other university for a degree and does not incorporate any material already submitted for a degree.

Signed

Dated

CO-AUTHORSHIP STATEMENT

The dissertation is based on 5 published (or accepted for publishing) research papers including 3 journal articles and 2 conference papers. Chapter 4 is based on the results of a research article entitled “Surface modification of TiO_2 photoanodes with In^{3+} using a simple soaking technique for enhancing the efficiency of dye-sensitized solar cells”. This work was recently accepted for publishing in *Journal of Photochemistry & Photobiology, A: Chemistry* and describes a method of modification of DSSC’s photoanode by a cost efficient simple method of solution treatment. The article was co-authored with Salimgerey Adilov and Mannix P. Balanay [1]. Chapter 5 is the summary of our published research paper with the title “Controlling aggregation using self-assembled axially coordinated pyridine-based ligands on porphyrin analogues for dye-sensitized solar cells” published in *Chemical Physics Letters 730 (2019) 407–410*, which was co-authored with Sang Hee Lee, Dong Hee Kim and Mannix P.Balanay [2]; and a published conference paper (*Eurasian Chemico-Technological Journal, 21(1), 2019, 63-67*) with the title “Control of porphyrin dye aggregation using bis(4-pyridyl)alkanes in dye sensitized solar cells” which was co-authored with A. Rysbekova, D. Kalpakov, A. Aukenova, D. Mustazheb, Z. Salkenova, M. Kazaliyev and M. Balanay [3]. Chapter 6 is written based on the results of a published research paper entitled “Pt-free counter electrode based on orange fiber-derived carbon embedded cobalt sulfide nanoflakes for dye-sensitized solar cells” co-authored with Ainura Aukenova, Dias Mustazheb, Miras Kazaliyev, Mannix P.Balanay (*Journal of Photochemistry & Photobiology A: Chemistry 383 (2019) 111977*) [4]; a published conference paper with the title “Binary Transition Metal Sulfides as an Economical Pt-free Counter Electrodes for Dye-sensitized Solar Cells” (*Materials Today: Proceedings*, DOI: 10.1016/j.matpr.2019.10.170) co-authored with D. Mustazheb and M.P. Balanay [5]. The contribution of the author in all abovementioned works as the first author was the review of literature, conducting experimental parts, analysis and interpretation of the data, preparation of the draft manuscript. The roles of the co-authors were assistance in the experimental parts and edition of the manuscripts.

Chapter 1

1 INTRODUCTION

1.1 Background

Energy has always been the vital element of human life and the key factor of the development of civilizations. The world today is not an exception and in fact, its need for energy has never been as it is now. The world energy demand is increasing as the planet's population is growing fast. UN report states that human population will reach 9.7 billion by 2050 and 11.1 billion in 2100 (Fig.1.1) [6], leading to 124% increase in energy consumption compared to the year 2015 (Fig.1.1) [7]. Traditional fossil fuels which the current world mostly relies on cannot cover the need in future due to the depletion of their resources, the alarming concerns of its damage to the environment and global warming which is believed to be the result of CO_2 emission (Fig.1.1) [8]. Estimations claim that fossil fuels are accountable for 74 % of all CO_2 emissions [9].

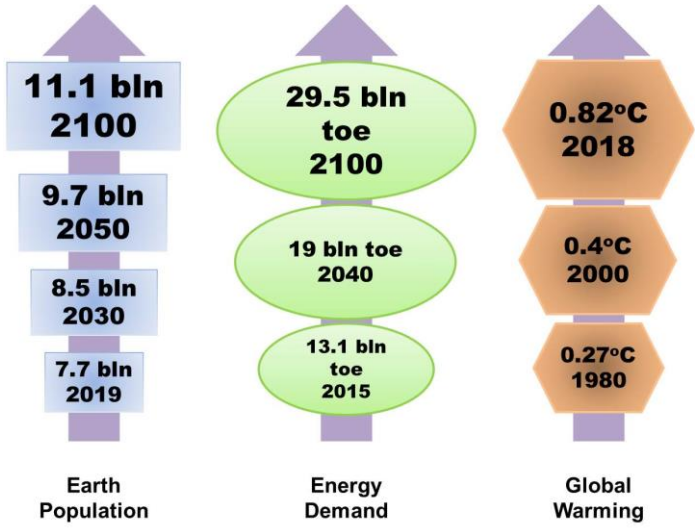

Figure 1. 1 Projected growth of human population with expected energy demand and annual average temperature change anomaly [6-8]

Since fossil fuels cannot be the major source of energy, renewable energy sources must dominate in the future. Current world energy consumption is about 580 EJ (1 EJ = 10^{18} J) [10]. If to compare the total amount of renewables on Earth and the maximum accessible amount (Table 1.1) with the current need, one can confidently claim that renewable sources can fully satisfy the energy demand in future. The potential of solar energy is promising since its total and utilizable amounts are greater than the sum of the other renewables. If used properly it alone can fully cover the demand of the planet.

Table 1. 1 Estimated potential of renewable energy sources

Potential	Solar	Wind	Biomass	Hydro	Ocean
Maximum accessible*, EJ	1600	700	200	59	11
Total**, EJ	3 900 000	28 400	3 000	130 - 160	700

* [11], ** [12]

According to Professor Richard Smalley, 1996 Nobel Laureate in Chemistry, six locations on Earth with 100×100 km area each having installed solar panels with 10 % efficiency can produce 20 TW (≈ 630 EJ / year) energy which would be enough for the current need, and if the efficiency is increased to 30 % this would be equivalent to 60 TW, enough for the future [13]. Besides abundance, solar energy is clean and environmentally friendly. CO_2 emission associated with solar energy generation is minimal. To compare, 1 kW×h generated from coal and natural gas release 18 and 9.5 times more carbon dioxide, respectively, compared to solar energy [14]. Therefore, the key benefit in utilizing solar power is not only energy supply but also reduction of greenhouse gas emissions. For these reasons, it is expected that the share of renewable sources in energy production will rapidly increase in near future and photovoltaics may produce about ¼ of the total energy by 2050 (Fig.1.2) [15]. Another forecast claims photovoltaics may generate about 40 % of all produced electricity by mid-century [16].

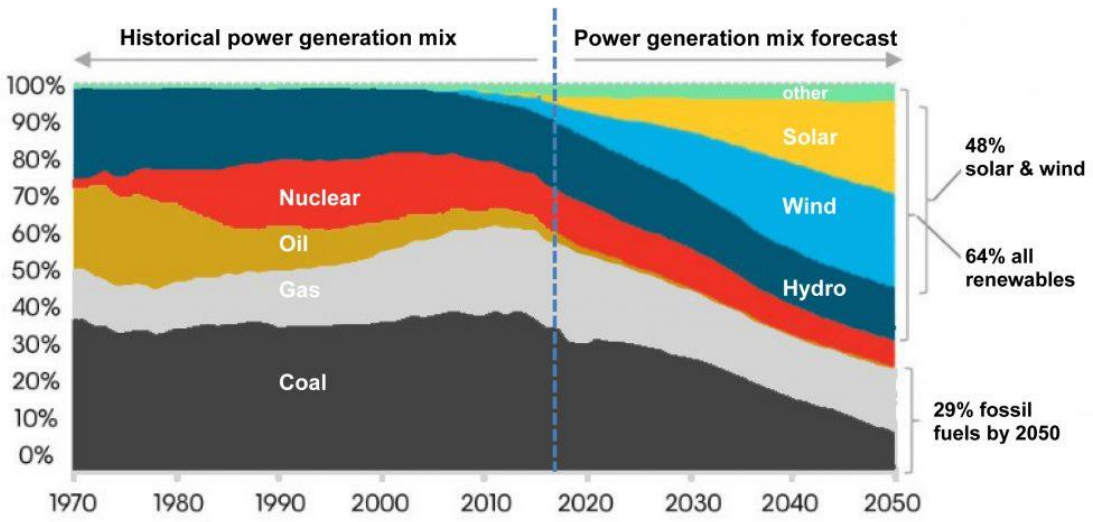

Figure 1. 2 Power generation by source: past, present and future [15]

Currently the solar energy market is heavily dominated by 1st generation crystalline silicon solar cells. This technology relies on costly production processes and thus, it is difficult to claim that silicon based PV technology can replace fossil fuel sector. Therefore, the key of the development of solar industry is low cost energy production. Third generation emerging solar technologies have a great potential to offer energy at lower price and higher efficiency. One of the types of 3G solar cells is dye-sensitized solar cell (DSSC). DSSCs have been the topic of intense research over the last three decades. It is easily manufactured using abundant materials that do not require high degree of purity and also it shows relatively high efficiency. The advent of dye-sensitized solar cells gave birth to building- and textile-integrated photovoltaics, flexible or printable solar panels and solar technology for indoor applications. However, at current, DSSCs cannot compete with the existing solar technologies because of relatively low efficiency and comparatively high cost of the device. Therefore, future development of DSSC technology heavily depends on decreasing the cost and increasing the efficiency. The components of DSSC like dye, electrolyte and platinum catalyst contribute up to 25 % of the total cost. Moreover, platinum and transparent conducting oxide substrates make up ~ 50 % of the cost [17]. The efficiency of DSSCs, on the other hand, strongly depends on perfect energy matching of the components, suppression of charge recombination and improvement of electron transfer. Therefore, we propose to develop cost-effective methods and components to improve DSSCs' efficiency and bring down its cost. The aim is to optimize the design of individual components of the solar cell via simple and cost-effective methods. This, we believe, will contribute to the development of cheap dye-sensitized solar cells.

1.2 Research Hypothesis

The hypothesis of the research thesis:

- Surface doping of the TiO_2 photoanode can be as effective as bulk doping. The use of simple solution treatment technic can optimize the performance of the TiO_2 photoanode.
- The aggregation of porphyrin dyes can be controlled via axial complexation and this will allow the use of easily prepared long alkyl chain free porphyrin sensitizers.

- The compounds of transition metals, especially abundant transition metal chalcogenides and their composites can be alternative to platinum counter electrode.

1.3 Novelty of the research

The following are the novelty of this research to the best of our knowledge:

- Modification of TiO_2 photoanode through simple surface doping method which leads to improved photovoltage due to retarded charge recombination;
- Implementation of axial complexation in porphyrin sensitizers to prevent dye aggregation and allowing the use of easily synthesized long alkyl chain free porphyrin analogs;
- Development of novel Pt-free counter electrodes based on orange fiber derived carbon embedded cobalt sulfide and ternary sulfide of copper and cobalt both of which outperform conventional Pt based solar cells.

1.4 Research contributions

Journal papers:

1) Bakhytzhan Baptayev, Sang Hee Lee, Dong Hee Kim, Mannix P.Balanay. “Controlling aggregation using self-assembled axially coordinated pyridine-based ligands on porphyrin analogues for dye-sensitized solar cells”, Chemical Physics Letters 730 (2019) 407–410 (IF: 1.901, Q2).

2) Bakhytzhan Baptayev, Ainura Aukenova, Dias Mustazheb, MirasKazaliyev, Mannix P.Balanay. “Pt-free counter electrode based on orange fiber-derived carbon embedded cobalt sulfide nanoflakes for dye-sensitized solar cells”. Journal of Photochemistry & Photobiology A: Chemistry 383 (2019) 111977. (IF: 3.261; Q1).

3) Bakhytzhan Baptayev, Salimgerey Adilov, Mannix P. Balanay. “Surface modification of TiO2 photoanodes with In3+ using a simple soaking technique for enhancing the efficiency of dye-sensitized solar cells”, Journal of Photochemistry & Photobiology A: Chemistry 394 (2020) 112468. DOI: 10.1016/j.jphotochem.2020.112468. (IF: 3.261; Q1).

Conference Papers:

1) B. Baptayev, A. Rysbekova, D. Kalpakov, A. Aukenova, D. Mustazheb,

Z. Salkenova, M. Kazaliyev,, M. Balanay. “Control of porphyrin dye aggregation using bis(4-pyridyl)alkanes in dye sensitized solar cells”. Eurasian Chem. Tech. J., vol. 21, no. 1, pp. 63-67, Feb. 2019. (CiteScore: 0.52; Q3)

2) B. Baptayev, D. Mustazheb, M.P. Balanay. “Binary Transition Metal Sulfides as an Economical Pt-free Counter Electrodes for Dye-sensitized Solar Cells”, Materials Today: Proceedings, DOI: 10.1016/j.matpr.2019.10.170. (CiteScore: 1.09).

Conference presentations:

1) Bakhytzhan Baptayev, Ainura Aukenova, Mannix Balanay. “Transition metal doped food waste derived carbon based counter electrode as a cost-effective alternative to Pt-counter electrodes in dye sensitized solar cells”. INESS-2018 Abstract Book. 8-10 Aug., 2018, Astana.

2) Bakhytzhan Baptayev, Mannix Balanay. “Binary Transition Metal Sulfide as Pt-free Counter Electrode for Dye-sensitized Solar Cells”, INESS-2019 Abstract Book. 7-9 Aug., 2019, Almaty.

Chapter 2

2 LITERATURE REVIEW

2.1 History of Photovoltaics

Humankind has been using the energy of Sun from the time it was created on Earth, though rational use of solar energy started more later with the development of science. It was Alexandre Edmond Becquerel, a French physicist, who is credited for the discovery of photovoltaic effect also known as 'Becquerel effect'. In 1839 at the age of 19 Becquerel, while experimenting with electrochemical cells, encountered an electricity generation when the electrodes placed into a conductive solution were exposed to light [18-19]. Later, in 1873 an English electrical engineer Willoughby Smith observed that the irradiation of light changes the electrical resistance of selenium making it more conductive [20]. In 1876 an English scientist William Grylls Adams and his student Richard Evans Day discovered the photovoltaic effect of selenium stating: "it was clear that a current could be started in the selenium by the action of the light alone" [21]. This led to the development of first photovoltaic cell made of selenium wafers by an American inventor Charles Edgar Fritts in 1883 [22]. However, the efficiency of the cell was around 1 % and at that time it could not compete with Thomas Edison's coal generated electricity. Nevertheless, the theoretical explanation of the photovoltaic effect was not clear until Albert Einstein published his Nobel Prize winning work on photoelectric effect in 1905. Einstein claimed that when light hits a matter "a light quantum transfers all of its energy to a single electron" [23]. Although his theory on photoelectric phenomenon was not widely accepted initially, it was experimentally proven later in 1914 by an American physicist Robert Andrews Millikan [24]. Two years later a Polish chemist Jan Czochralski accidentally develops a method of growing metal single crystals which was later used to grow silicon single crystals [20]. Together with the advent of band theory on semiconductor single crystals this laid foundation to the development of solar cells [25].

2.2 Theory of Photovoltaics

Solar cells or photovoltaic (PV) cells convert light energy into electricity. The main component of solar cells which converts light into electricity is semiconductor. This becomes possible due to their electronic structure. Generally, the electron energetic levels can be grouped into two bands – valence

band and conduction band. Valence band contains highest occupied molecular orbitals (HOMO). At ambient conditions most of the electrons reside in valence band. Conduction band is energetically higher than valence band and contains lowest unoccupied molecular orbitals (LUMO). Conduction band may overlap with the valence band such as in metals or be separated like in semiconductors and insulators (Fig.2.1). The energy difference between the top of valence band and the bottom of conduction band is called **band gap** (E_g). The band gap of insulators is very high. Unlikely, the band gap of semiconductors is narrow and the electrons can be promoted from valence band to conduction band using small amount of energy. This process is known as **excitation**.

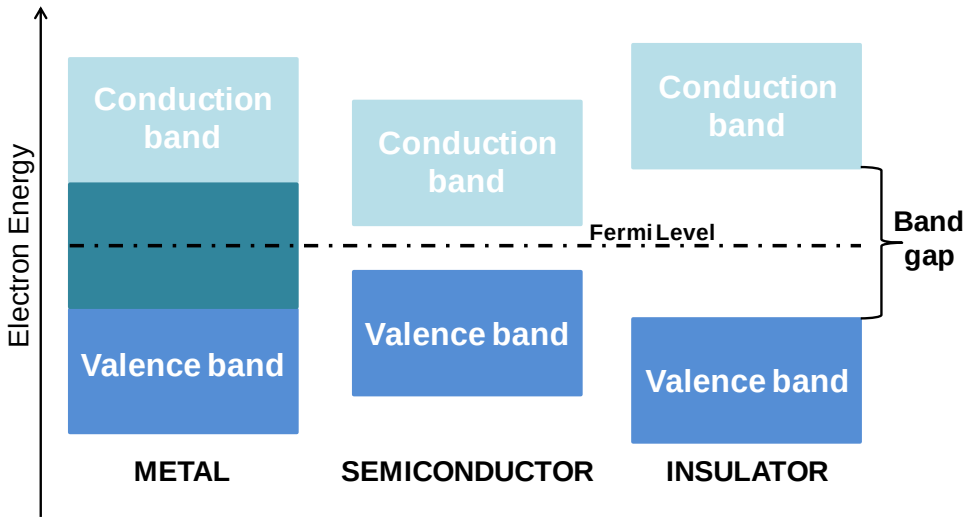

Figure 2. 1 Band distribution in metals semiconductors and insulator

In PV cells the electrons of semiconductors are photoexcited using the energy of light (Fig.2.2). When a photon with energy higher than the band gap hits the semiconductor it will be absorbed promoting electron to conduction band and leaving a hole – an unoccupied state in the valence band. These two are oppositely charged and attracted to each other via electrostatic force. This state is called **exciton**. The electron in the conduction band can be recombined with the hole in a process called **exciton annihilation** or separated also known as splitting or **exciton dissociation.** The separated charges are collected at opposite electrodes. Thus, the whole process of the generation of current and voltage using photon energy is known as **photovoltaic effect.**

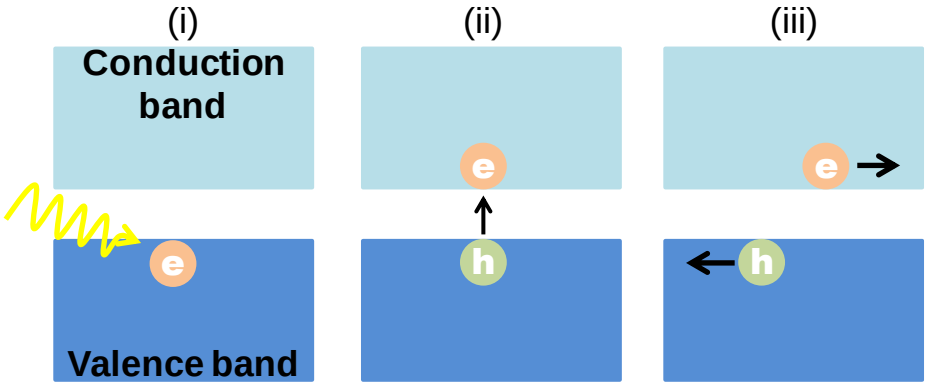

Figure 2. 2 Photovoltaic effect or the working principle of solar cells: (i) light absorption; (ii) photoexcitation - formation of exciton; (iii) charge separation – transportation of charge carriers to electrodes;

The prerequisite of electricity generation in PV cells is efficient collection of charge carriers by electrodes which in turn requires efficient exciton dissociation. Upon photoexcitation an electron may quickly recombine with hole and commonly used method to prevent this is to bring the exciton to the interface of two different materials (semiconductors) with offset energetic levels (Fig.2.3).

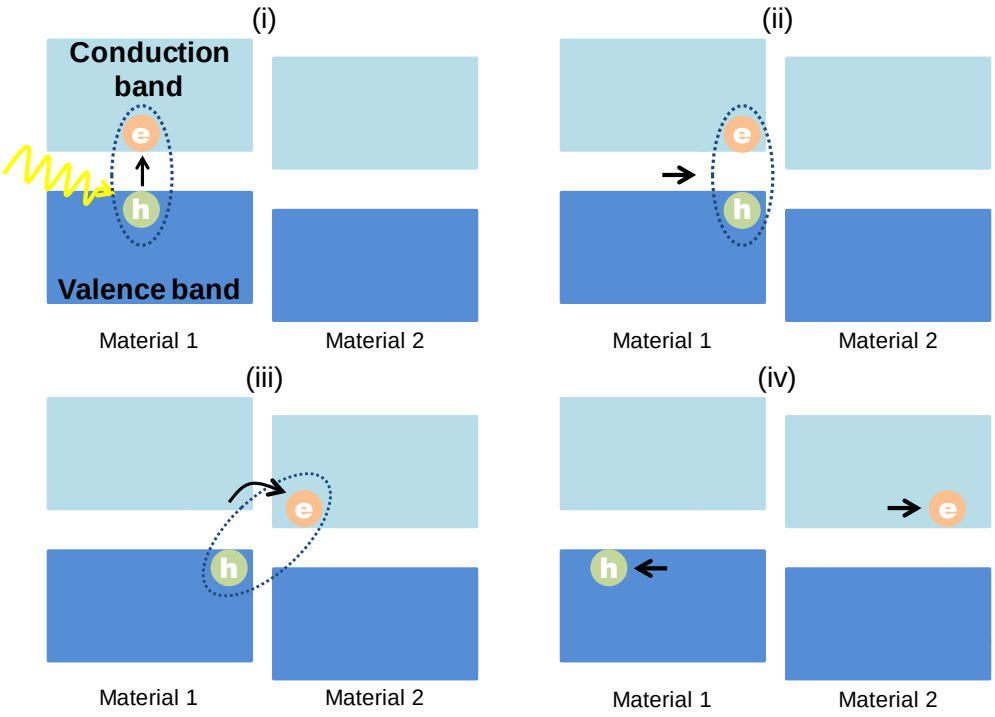

Figure 2. 3 Exciton dissociation at the interface of different materials (i) formation of exciton by photoexcitation; (ii) diffusion of exciton to the interface; (iii) electron is transferred to the material with offset energy level; (iv) charges are transported to electrodes.

The common example of two materials' interface is the ***p-n* junction**. In p-n junction two different semiconductors, a *p*-type semiconductor with excess holes and a *n*-type semiconductor with excess electrons, are brought together. The excess of electrons / holes is achieved through **doping**, addition of impurities to a pristine material which depending on the dopant either adds electrons to the conduction band (*n*-type) or adds holes to the valence band (*p*-type) of the semiconductor. When *n*- and *p*-type semiconductors form junction the free moving electrons and holes start to diffuse in opposite directions leaving fixed charge regions behind – positive charge on the side of n-type semiconductor and negative charge on the side of p-type semiconductor (Fig.2.4). The area near the interface with fixed charge and without free moving charge carriers is called **depletion region**. An electric field is formed due to fixed charges at depletion region. The field drifts charge carriers in the opposite direction: the electrons are accelerated towards *n*-type side and the holes are accelerated towards *p*-type side. In solar cell, when light is absorbed by the semiconductor this leads to the photoexcitation of electrons to conduction band creating holes in the valence band. The photogenerated electrons are drifted to the electrical contact at n-type side, whereas the photogenerated holes are drifted to the electrical contact at p-type side (Fig.2.4).

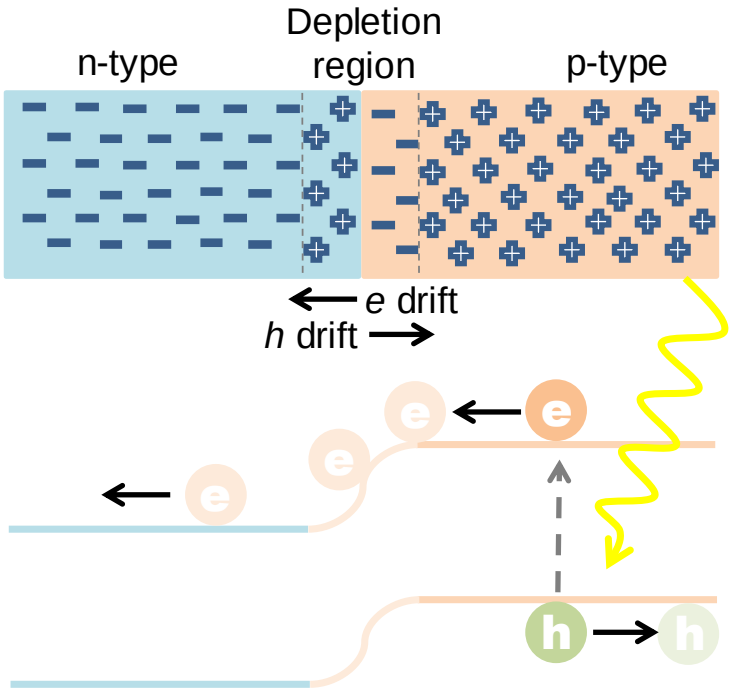

Figure 2. 4 *p-n* junction and PV cell in operation

The band gap of semiconductor determines the photons to be absorbed. Only those photons with energy equal or higher than the band gap energy (≥ E_g) can be absorbed. Upon absorption the energy in excess of band gap is lost through **thermalization** – interaction with lattice and the photoexcited electron relaxes to conduction band minimum. If the band gap is too high then only small fraction of light will be absorbed. Similarly too small band gap results in the loss of excess energy. Yet the Sun radiates in a broad spectral region starting from 280 nm until 4000 nm corresponding to photons with energies 0.3 – 4.4 eV. Considering the above mentioned, Shockley and Queisser calculated maximum power converting efficiency for a PV cell with a single light absorbing material with an optimal band gap [26]. Applying new ASTM International G173-based reference spectra the efficiency limit for single junction PVs is 33.8 % under AM1.5 and the optimal 1.34 eV band gap [27]. **AM** stands for the air mass coefficient and describes the optical path length of solar photons through the atmosphere. It is the ratio of the optical path length *L* at the angle *z* relative to the zenith and to the optical path length L_o at zenith ($z = 0^o$), see equation 2.1:

$$AM = \frac{L}{L_0} \approx \frac{1}{\cos(z)} \tag{2.1}$$

The Sun radiation is similar to the radiation of a blackbody at 5780K. AM0 is the sun radiation above the atmosphere relative to the blackbody radiation. AM1 is the radiation at sea level with $z = 0^o$, whereas AM1.5 is the solar radiation at z = 48.2^o (Fig.2.5).

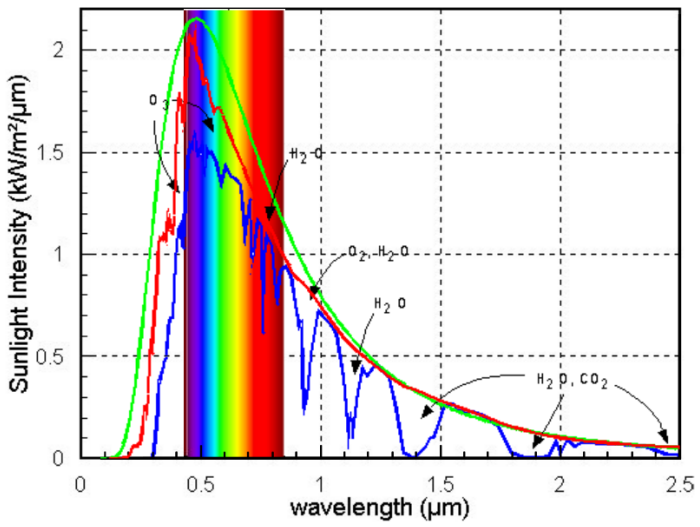

Figure 2. 5 Solar irradiance at different air mass: blackbody radiation (green); AM0 (red) and AM1.5 (blue) [28]

2.3 Solar Cell Generations

2.3.1 First generation solar cells

1G solar cells are generally made of silicon and make up around 95 % of the solar panel market today [29]. This generation of PVs has the longest history and currently the highest efficiency among all. In addition, the lifespan of the silicon-based solar cells is very long: 25 – 30 years. Mono-crystalline Si based solar cells have the highest record efficiency of 26.7 % [30-31]. However, the cost of production of silicon monocrystals is very high. Multi-crystalline Si is cheaper to obtain but the efficiency is also lower 22.3 % [30]. Nevertheless, the production of high purity silicon remains very expensive. It is reported that for a kilogram of pure silicon 15 – 90 kWh electricity is used and it can take up to 2 years to generate this energy for the PV [32].

2.3.2 Second generation solar cells

2G solar cells have lower cost compared to the 1G PVs due to less expensive manufacturing and thin layer of the semiconductor material. Because of this they are also known as thin film solar cells. They account for about 5 % of the market [29]. Amorphous-Si, cadmium telluride (CdTe) and copper indium gallium selenide (CIGS) belong to this group of PV technology. Among them CIGS is the leader with 23.4 % power converting efficiency [33]. The advantage of CIGS is the tunable bandgap 1.0 – 1.7 eV [34]. The efficiency of CdTe solar cells is bit lower 22.1 % and the amorphous-Si generates energy with 14.0 % cell efficiency [33]. The disadvantages of CdTe technology is the toxicity and scarcity of its components. Amorphous-Si suffers from low efficiency and stability problems.

2.3.3 Third generation solar cells

3G solar cells are new technologies in PVs. They are also known as emerging photovoltaics. Although they use thin-films, the efficiency is expected to be higher than in 2G. 3G solar cells apply non-silicon materials like organic semiconductors, nanomaterials and polymers. PVs which belong to this group are organic solar cells (OPV), dye-sensitized solar cells (DSSCs), quantum dot solar cells (QSC) and perovskite solar cells (PSC). The efficiencies of 3G PVs together with 1G and 2G are shown in the table below (Fig.2.6). PSC is leading by efficiency in 3G solar cells reaching 25.2 %, a comparable with monocrystalline-Si. However, they severely suffer from cell stability. Besides, the toxicity of lead component is another major issue. OPV and QSC have similar

efficiencies 16.5 and 16.6 %, respectively. However, the use of toxic heavy metal quantum dots is a challenge for the QSC. The disadvantage of OPV is related to stability of the material under temperature and air. Other problems associated with OPV is charge carrier lifetime, exciton diffusion length and charge separation. The PCE of DSSCs is 11.9 % according to NREL [33] although reports exist claiming higher efficiency. In 2018 Professor Gratzel reported a new architecture for DSSCs with a record efficiency of 13.1 % at AM1.5, 100 mW / cm^2 and 32 % under 1000 lux indoor light conditions [35]. Unique properties of DSSCs are the possibility to use low intensity light, light harvesting at extreme angles and stability of the photovoltage under different light conditions. Nevertheless, DSSC's major obstacle is poor stability due to the use of liquid electrolyte. The application of expensive components which affects the final price of the device is another critical issue of DSSC technology. Hence, this thesis investigates the cost-effective methods and components for dye-sensitized solar cells.

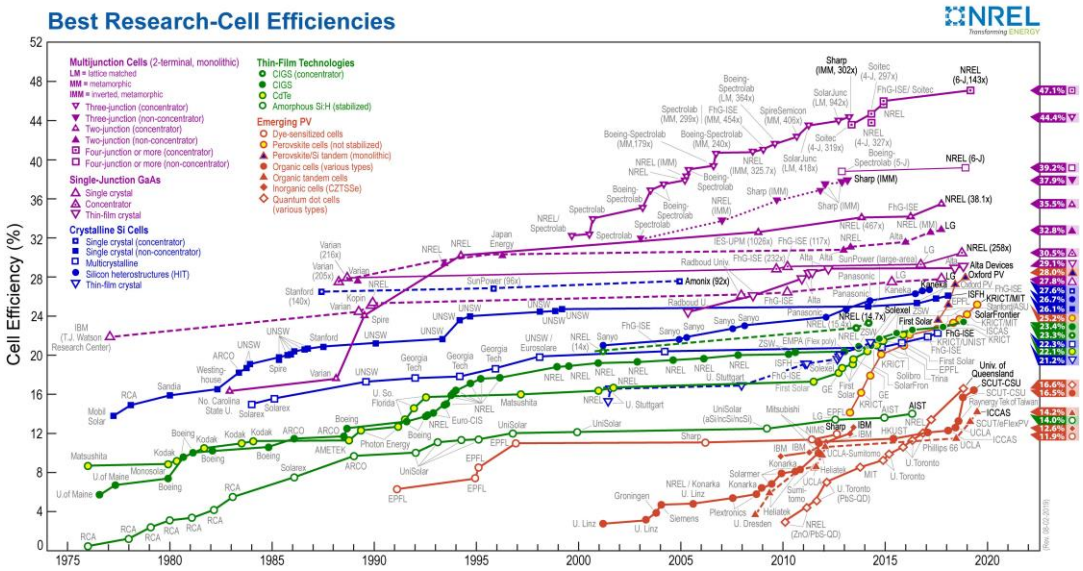

Figure 2. 6 Best research cell efficiencies provided by National Renewable Energy Laboratory for 02/08/2019 [33]

2.4 Dye-Sensitized Solar Cells

Originated in 1991 as a thin film technology, dye-sensitized solar cells have changed scientists' view of photovoltaics. The use of cheap materials and accessible methods in manufacturing made the DSSCs a potential alternative to high cost Si-based solar cells [36]. What makes it attractive is the possibility of light harvesting at weak light intensities and extreme angles which many solar

cells cannot offer. This enables their application outside under diffused daylight and indoor under low-light conditions.

Dye-sensitized solar cell is considered a photoelectrochemical cell and consists of two electrodes: anode and cathode, see Fig.2.7a. The anode is a transparent conducting oxide (TCO) electrode with a film of semiconducting oxide nanoparticles. The oxide nanoparticle is sensitized with dye molecules. The cathode is composed of a layer of catalytic material on TCO. The two electrodes are brought face-to-face and the space between the two is filled with a redox electrolyte. The dye is responsible for light absorption and electron injection into the semiconductor. The injected electrons travel to back electrode, while the oxidized dye is reduced by the redox mediator. The oxidized species of the latter are catalytically regenerated at the counter electrode. All these processes happen due to energetics of the components of DSSC, see Fig.2.7b. When dyes are hit by photons their electrons are photoexcited from HOMO to LUMO. The excited electrons can be injected into the conduction band of the semiconductor or decay back to HOMO. The latter does not contribute to current generation. Luckily, charge transport kinetics work in favor of injection (occurs on a femto- to picosecond time scale) and the electrons are injected into the semiconductor conduction band [37]. The injected electrons have to migrate through semiconductor to back contact, another required step for current generation, before they are recombined with oxidized dye or redox electrolyte. Since the dye regeneration process is very fast, taking place in nano- to microsecond time frame, the possibility of injected electron recapture by the oxidized dye is very small. The remaining two processes, electron diffusion via semiconductor and recombination with redox media, are in conflict since both occur in a millisecond to second scale [38]. Therefore, various methods and technics of controlling recombination are used in DSSC.

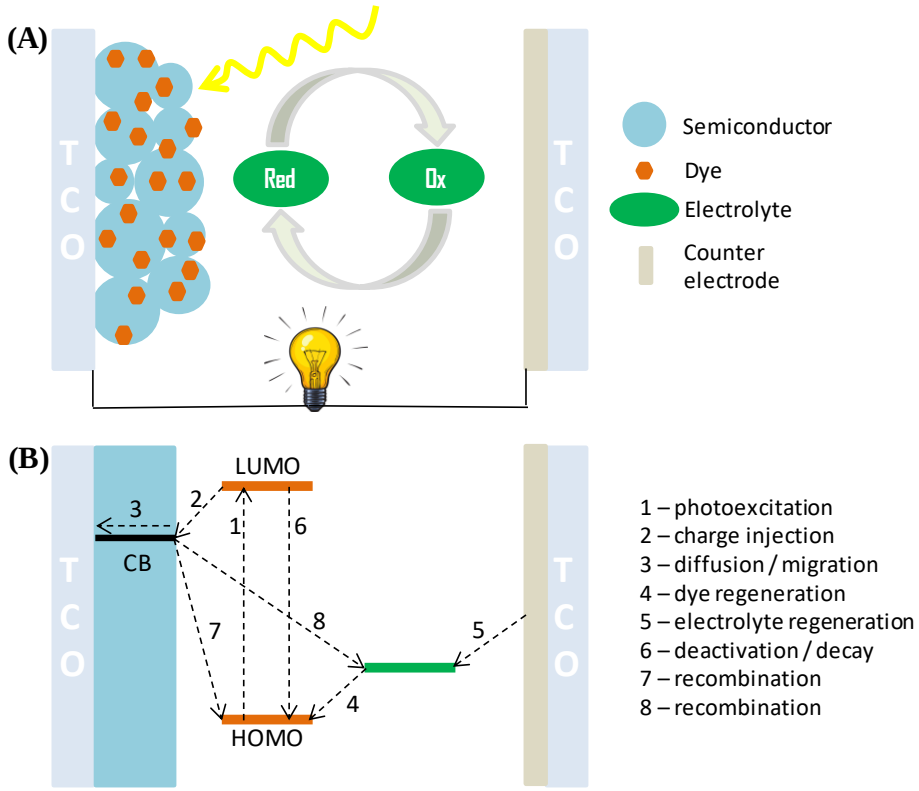

Figure 2. 7 a) schematics and b) energy level and operation of dye-sensitized solar cells

Thus, to generate power from sunlight the LUMO of dye must be higher that the conduction band of the semiconductor to have enough energy (ΔG_{inj}) for electron injection. To regenerate the dye its HOMO level must be lower than redox potential of the redox mediator and the difference between the two makes free energy for regeneration (ΔG_{reg}). The minimum free energy for the fast charge injection should be around 0.2 eV [39]. The difference between the semiconductor conduction band and redox potential of the electrolyte corresponds to the open-circuit voltage of the cell (V_{OC}). Mathematically the voltage *V* is given as:

$$qV = E_F - E_{F0} \tag{2.2}$$

where q is electronic charge, E_F and E_{F0} are Fermi levels of the semiconductor in the light and in the dark, respectively [40]. At open circuit V = V_{OC}.

The short-circuit current density J_{SC} is derived from incident-photon-to-current conversion efficiency (IPCE):

$$J_{SC} = e \int IPCE(\lambda) \times \Phi_{SUN}(\lambda) d\lambda \tag{2.3}$$

where Φ_{SUN} is incident photon flux [41]. The IPCE is the product of light harvesting efficiency (LHE), injection efficiency (φ_{inj}), regeneration efficiency (φ_{reg}) and charge collection efficiency (φ_{cc}):

$$IPCE(\lambda) = LHE(\lambda) \times \varphi_{inj}(\lambda) \times \varphi_{reg}(\lambda) \times \varphi_{cc}(\lambda) \quad (2.4)$$

LHE depends on the light absorbing property of the sensitizer. Dyes with large molar extinction coefficients demonstrate high LHE. φ_{inj} is related to the coupling of dye anchoring group with the semiconductor. The product of injection (φ_{inj}) and charge collection (φ_{cc}) efficiencies correspond to absorbed-photon-to-current conversion efficiency (APCE) [42].

Both open-circuit photovoltage V_{OC} and short-circuit photocurrent density J_{SC} are important parameters of DSSC and the power converting efficiency PCE of cell is directly proportional to the product of the two. These are obtained from I-V characteristic curve of a solar cell. Fig.2.8 illustrates the I-V curve of solar cell (black curve) and the power generated from the cell (red curve). The efficiency of a cell is the ratio of maximum produced power P_{MP} to the input power P_0:

$$PCE = \frac{P_{MP}}{P_0} \quad (2.5)$$

The power is the product of I and V and therefore the maximum power point P_{MP} would be:

$$P_{MP} = I_{MP} \times V_{MP} \quad (2.6)$$

The maximum power can be represented by J_{SC} and V_{OC}:

$$P_{MP} = FF \times J_{SC} \times V_{OC} \quad (2.7)$$

where FF is fill factor and it demonstrates the “squareness” of the I-V curve. If the shape of I-V curve is similar to rectangle then fill factor is close to unit and vice versa. Combining the equations (2.5) and (2.7) gives:

$$PCE = \frac{FF \times V_{OC} \times J_{SC}}{P_0} \quad (2.8)$$

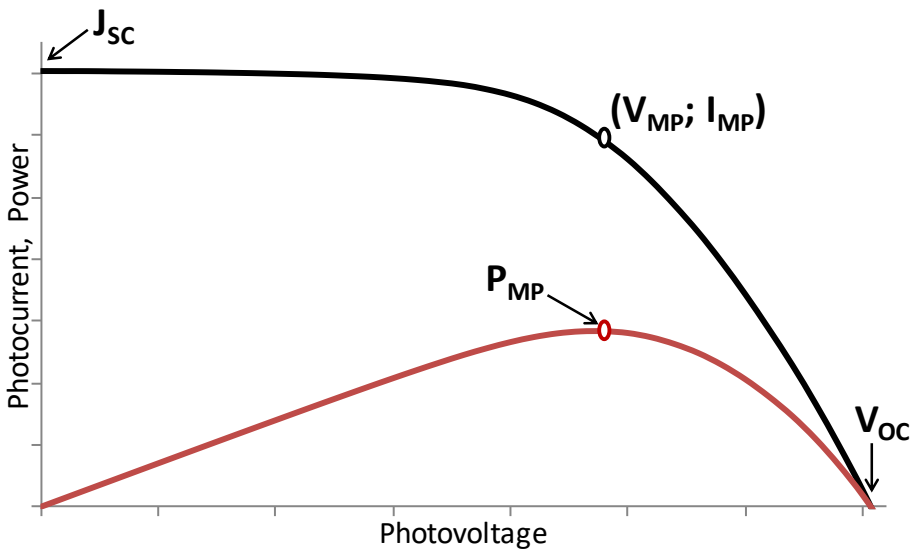

Figure 2. 8 I-V characterization of dye-sensitized solar cell

The efficiency of first reported ruthenium – dye sensitized mesoporous TiO_2 solar cell was about 7.1 – 7.9 % [36]. Modification of the ruthenium dye to improve light harvesting property resulted in 11.5 % PCE in 2009 [43]. This cell used liquid electrolyte based on iodine / iodide. Two years later the application of cobalt – based redox electrolyte instead of I_2 / I_3^- and the substitution of ruthenium sensitizers with donor-π-acceptor porphyrin dye (labelled YD2-o-C8) generated power at record 12.3 % efficiency at AM1.5 [44]. The utilization of new Co – based electrolyte increased voltage reaching almost 1 V. Later improvement of the porphyrin dye via incorporation of novel donor and acceptor groups pushed the PCE to 13 % under AM1.5G illumination [45]. In 2015, 14.3 % efficiency under AM1.5G was reached by co-sensitization – application of more than one dye and using Co-based mediator [46]. Recently, the group of Professor Gratzel at EPFL reported a new architecture for DSSCs with direct contact demonstrating 13.1 % PCE at full sunlight and record 32 % power conversion under 1000 lux ambient light conditions [35]. The photovoltaic performance of DSSC depends on the characteristics of its components and their energy alignment.

2.5 Components of Dye-sensitized Solar Cells

2.5.1 Photoanode

In a typical solar cell the processes of light absorption, charge separation and transport are carried out by semiconductor. However, in DSSCs these are separated. The light harvesting is accomplished by sensitizing dye, whereas the charge transport is performed by semiconducting photoanode. The photoanode also known as working electrode is a thin film of a nano-sized wide band gap semiconductor placed on a transparent conducting electrode. The function of photoanode is collection of injected electrons, providing path for charge diffusion and collection at the TCO back contact. Since photons are absorbed by dye, ideally, neither semiconductor nor TCO substrate should absorb in the visible spectrum. Moreover, the electrical resistivity of TCO should be low to prevent energy loss during charge collection. FTO (fluorine – doped tin oxide) is extensively used in DSSCs. The use of ITO (indium tin oxide) is restricted by its thermal instability. Usually, sintering is required to obtain high crystallinity of semiconductor and heating above 300^{o}C is detrimental for ITO. Although ITO is more conductive than FTO, heating at 300^{o}C or higher increases its resistance by three times [47]. It is reported that DSSCs assembled from FTO and ITO demonstrated PCEs 9.6 % and 2.24 %, respectively, and the poor efficiency of the latter was ascribed to small J_{SC} resulted from increased resistance [48].

Similarly, photoanode should also be optically transparent to prevent loss of photons and possess high electron mobility to provide better charge transport. Additionally, it should have high surface area to accommodate as many dye molecules as possible. It is the use of high surface area semiconductors that brought DSSC to PV arena. Historically, the efficiency of DSSCs was very low due to the use of single crystal semiconductors. For comparison, the IPCE of a flat single crystal electrode at 530 nm was reported to be 0.13 %, whereas, the use of mesoporous nanocrystalline electrode demonstrated 88 % incident photon-to-current conversion efficiency, corresponding to more than 600 times increase [49]. This results in 10^3 - 10^4 times boost of J_{SC} in nanocrystalline cell compared to single-crystalline electrode [50]. Moreover, the photoanode must be chemically stable and should not react with the redox mediator. It should be able to chemically bond with the dye molecules providing good electronic coupling with the acceptor group of sensitizer.

There are many wide band gap semiconducting materials which satisfy the above mentioned requirements and some of them are TiO_2 [51], ZnO [52], SnO_2 [53], Nb_2O_5 [54]. TiO_2 is the most studied and widely used photoanode due to its abundance, low cost, ease of preparation and non-toxicity. Three structural forms of TiO_2 are available: anatase, rutile and brookite. Anatase is the best performing form so far. It has wider band gap (3.2 eV) compared to rutile (3.02 eV) and brookite (2.96 eV) which makes anatase more stable under sunlight [55]. Moreover, it is claimed that the lifetime of electrons in anatase is longer due to its indirect band gap, whereas direct band gap of rutile and brookite makes the injected electrons susceptible for recombination [56]. Park et al. reported that cells made of anatase and rutile produced equal photovoltages but the latter generated 30 % less photocurrent [57]. This resulted from smaller dye loading in rutile caused by its less surface area. Moreover, they found that electron transport was slower in rutile. In a similar study, brookite-based cell demonstrated less J_{SC} due to lower dye loading and smaller diffusion length and low charge collection efficiency due to faster recombination kinetics compared to anatase [58]. The best performing DSSCs were fabricated from anatase TiO_2 [45-46]. Usually TiO_2 mesoporous nanoparticles with average size around 20 – 30 nm is used and the thickness of film is around 10 µm (Fig.2.9). This provides high surface area and hence increased dye load which is a requirement for generating high J_{SC} and PCE. On the other hand, this increases the recombination site at TiO_2 / electrolyte and allows the contact of electrolyte with the FTO. The interface FTO / electrolyte is also prone for charge recombination that lowers J_{SC}. This can be overcome by the introduction of a thin blocking layer at the interface of FTO / TiO_2. The compact layer is prepared from various materials including TiO_2 [59-60], ZnO [61], SnO_2 [62], Nb_2O_5 [63], etc. The most commonly utilized compact layer is TiO_2. It is reported that the presence of compact – TiO_2 layer at FTO / meso – TiO_2 interface increases the cell efficiency over 160 % under standard one sun and over 200 % under low light conditions for DSSCs operating with organic dyes [64]. A simple extensively used procedure of TiO_2 compact layer preparation is chemical bath deposition method where FTO electrode is kept in $TiCl_4$ solution under elevated temperature for known time before applying mesoporous TiO_2 [65]. The presence of compact layer also improves the adhesion of meso-TiO_2 providing greater contact area [66].

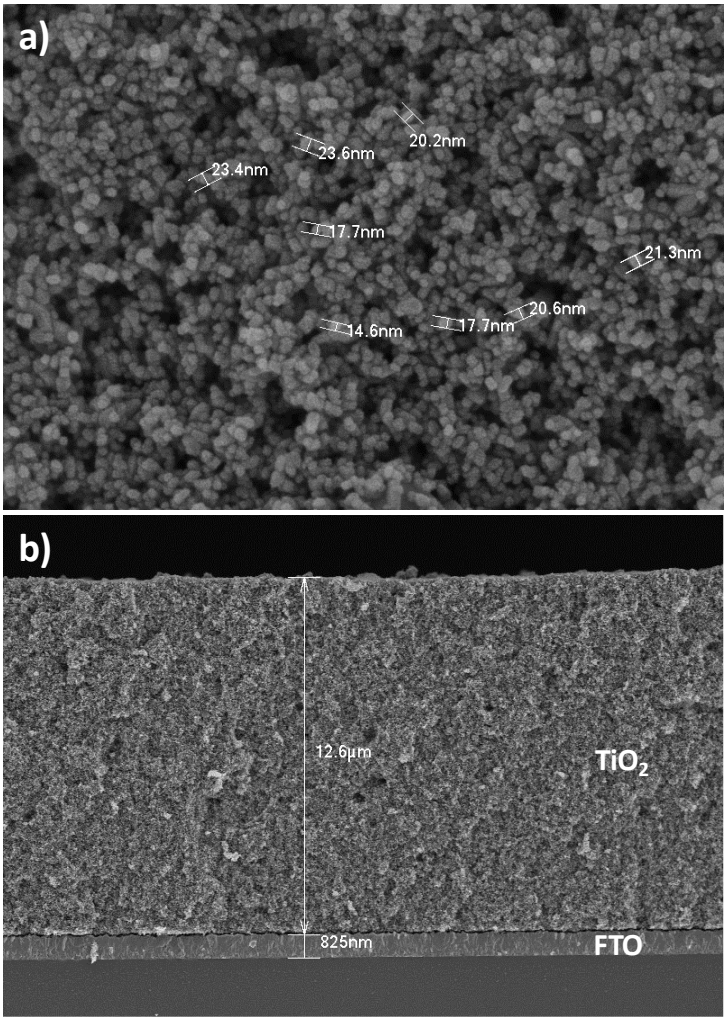

Figure 2. 9 SEM image of TiO_2 nanoparticles (a) and cross section of TiO_2 film on FTO glass electrode (b)

After meso-TiO_2 is applied and the electrode is sintered the film is again treated with $TiCl_4$. This post-treatment also has beneficial effect to solar cell performance. Although the result of post-treatment is the increase in J_{SC}, the exact mechanism of the influence is not clear. Sommeling et al. claimed that the increase in J_{SC} upon $TiCl_4$ post-treatment is due to the shift in TiO_2 conduction band caused by the treatment [67]. The downward movement of conduction band increases free energy for charge injection and, thus, increases injection efficiency. Others state that $TiCl_4$ post-treatment improves charge transport via improving neck between TiO_2 particles [66, 68]. However, the agreed effect of post-treatment is the increase in dye loading.

It is known that raising dye load increases cell photocurrent. Therefore, film thickness also plays role in determining J_{SC}; however, it cannot be increased without affecting V_{OC}. Thicker film means larger surface for photoanode /

electrolyte interaction and hence increased recombination which lowers both cell voltage and current. Another common method of increasing light harvesting is through increasing the optical path length of photons by applying light scattering layer over transparent nanoparticle film (Fig.2.10). This layer is usually composed of sub-micro sized particles.

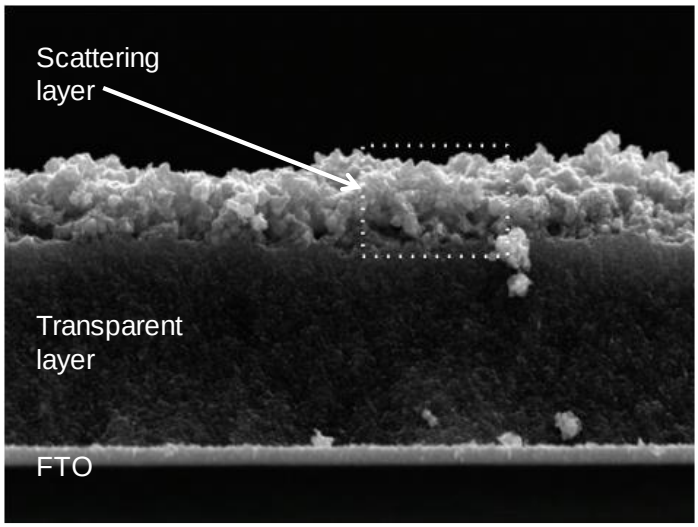

Figure 2. 10 Cross sectional view of photoanode composing of transparent and scattering layers [69]

The group of Michael Gratzel investigated the role of scattering layer on the performance of dye-sensitized solar cell [70]. Four configurations of photoanode film was prepared: **a** – 3.4 μm layer of 20 nm sized TiO_2 and 4.5 μm layer of 400 nm sized TiO_2 with 10 nm sized TiO_2 layer between the two; **b** – the same as in recipe **a** but the normal 400 nm TiO_2 microparticles were coated with 20 nm thick SiO_2 layer; **c** – 1.5 μm thick layer of 10 nm sized SiO_2 was placed between nano-TiO_2 and micro-TiO_2; **d** – 4.5 μm layer of TiO_2 microparticles. The control cell was made of nano-TiO_2 with 3.4 μm thickness and designated as **e**. The PV performance of the cells is shown in Table 2.1.

Table 2. 1 Photovoltaic parameters of dye-sensitized solar cells with different photoanode configuration [69]

Cell	J_{sc}/mA cm^{-2}	V_{oc}/mV	*FF*	η/%
a	14.5 ± 0.2	840 ± 6	0.72 ± 0.01	8.8 ± 0.1
b	12.6 ± 0.3	845 ± 5	0.71 ± 0.01	7.6 ± 0.2
c	10.1 ± 0.1	836 ± 5	0.73 ± 0.01	6.2 ± 0.1
d	7.8 ± 0.1	864 ± 4	0.75 ± 0.01	5.0 ± 0.1
e	9.7 ± 0.1	834 ± 3	0.74 ± 0.04	6.0 ± 0.0

It is clear that the presence of light scattering layer had a significant effect on photocurrent which implies that light harvesting was increased. The DSSC with photoanode composing of nano- and micro-TiO_2 demonstrated 8.8 % efficiency corresponding to 46 % increase compared to reference cell. The increase of PCE was mainly ascribed to improved J_{SC}.

The thickness of the scattering layer also affects the cell performance. Min-Kyu Son et al studied the effect of light scattering layer thickness and found that increasing the thickness of scattering layer has positive effect on cell performance but too thick layer adversely affects cell efficiency [71]. As the result, the optimal thickness of scattering layer improved photocurrent by over 80 % compared to control cell without scattering layer and the PCE was increased by 55 %.

Nevertheless, TiO_2 suffers from low electron mobility and high charge recombination [40, 51, 72]. Further improvement of the efficiency should rely on improving charge transport in TiO_2 semiconductor and controlling the recombination of injected electrons.

ZnO, in this regard, may offer several suitable characteristics. ZnO is considered the best alternative to TiO_2 semiconductor in DSSCs. This is due to similar band gap energy and band edge alignment of ZnO (3.2-3.3 eV) (Fig.2.11). It has much higher electron diffusivity than TiO_2 and high electron mobility [52]. Additionally, the exciton binding energy of ZnO is high which implies that excitons in ZnO are stable against thermal dissociation [55]. These are beneficial for faster electron transport and decreased recombination. Nonetheless, the highest reported efficiency of ZnO sensitized solar cells is lower than their TiO_2 analogs. The record 7.5 % PCE was achieved by using hierarchically structured ZnO nanoparticles prepared by spray pyrolysis method [73]. The photoanode was composed of polydispersed ZnO particles: mesoporous nanocrystallites and light scattering submicrometer range particles. Zinc acetate in methanol / water solution was used to prepare a compact buffer layer over FTO via spray pyrolysis. Hence, thanks to high light absorption in polydispersed ZnO film and retarded recombination at FTO / electrolyte interface, 7.5 % light-to-current conversion was obtained.

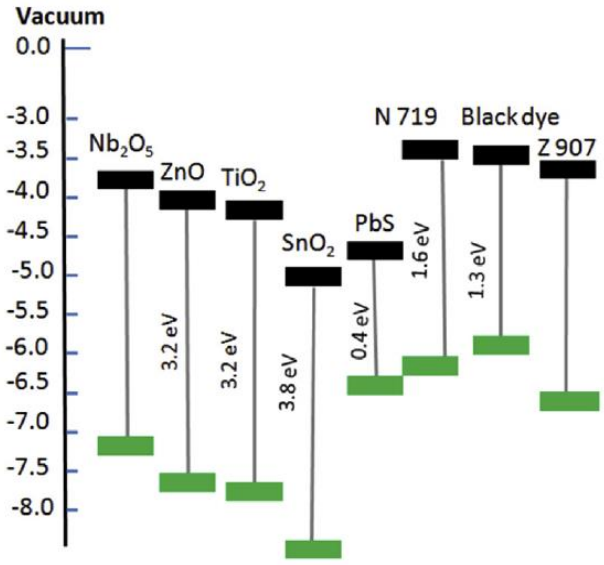

Figure 2. 11 Band diagram of common photoanodes and dyes used in DSSC [53]

To understand why ZnO performance is lower than that of TiO_2 Quintana et al investigated the DSSCs prepared from ZnO and TiO_2 photoanodes of equal particle size (15 nm) [74]. Intensity modulated photocurrent spectroscopy analysis showed identical electron transport for both electrodes; however, ZnO was superior in lifetime than titania. Despite the rate of recombination was low, the performance of ZnO cell was less. The authors attributed it to poor charge injection efficiency from excited sensitizer to ZnO conduction band and slow dye regeneration. Another reason of low PCE in ZnO DSSCs is the instability of the photoanode. ZnO has basic nature and in the presence of acidic sensitizers it can dissolve into Zn^{2+} which can later on form agglomerates with the dye molecules [75]. These agglomerates accumulate in the pores of ZnO and inhibit efficient electron injection. To prevent the formation of Zn^{2+} / dye agglomerates core – shell structure were developed where ZnO is coated with buffer layer. SiO_2 is one of successfully applied shell material over ZnO core [76]. The result is over 11 times increase in the photocurrent and 10 times boost of the cell efficiency. Similarly, it is reported that ZnO / TiO_2 core – shell photoanode based DSSC demonstrated much better performance than bare ZnO photoanode based cell [77]. The result was attributed to increased stability of TiO_2 covered ZnO photoanode against dye molecules. Yet the performance of ZnO sensitized solar cells is inferior to TiO_2 DSSCs.

Next alternative to TiO_2 photoanode is SnO_2. The use of SnO_2 is explained by its two main advantages: i) its band gap is wider (3.6 – 3.8 eV) compared to

anatase (3.2 eV) and ii) electron mobility in SnO_2 is faster for two orders than in TiO_2 [78]. Wide band gap implies its prolonged stability under sunlight. High charge mobility allows efficient charge transport and hence minimized recombination. Despite of this, the highest efficiency achieved by SnO_2 based DSSCs so is 9.53 % and it is lower than the PCE of TiO_2 sensitized solar cells [79]. The reason is small dye loading on SnO_2 photoanode due to its lower isoelectric point (pH = 4 - 5) compared to TiO_2 (pH = 6 - 7) [80]. This leads to reduced J_{SC}. Moreover, the conduction band edge of SnO_2 is below than that of TiO_2 (see Fig.2.11). This minimizes the V_{OC} since cell photovoltage is the difference between Fermi level of the photoanode and the redox potential of electrolyte. Also, low conduction band edge results in loss of photon energy.

In addition to TiO_2, ZnO and SnO_2, several other semiconductors have been used in DSSCs as photoanodes for their amusing properties. For its wide band gap (2.6 – 3.1 eV), high stability in acidic media and similar to TiO_2 electron mobility WO_3 attracted the attention of researchers as an alternative photoanode for DSSCs [81]. Another wide band gap (3.2 – 4 eV) metal oxide that is used as photoanode in DSSCs is Nb_2O_5 [54]. It draws attention because of its conduction band edge which is higher than TiO_2 and may assist in achieving elevated cell voltage. Due to the presence of several metals and their potential synergistic effect, ternary oxide based photoanodes are also interesting as DSSC photoanodes. Among noticeable candidates are Zn_2SnO_4 [82], $BaSnO_3$ [83], $SrTiO_3$ [84], etc. The efficiencies of DSSCs for extensively investigated photoanodes are shown in Fig.2.12.

Further improvement of the photoanode should consider enhancing charge transport capability in order to increase electron lifetime and therefore, suppress recombination. The problem of nanoparticle photoanodes is short diffusion length (10 – 35 μm) caused by multiple trapping and detrapping events taking place within nanoparticle grain boundaries, defects and surface states [85]. The disorder of nanoparticles and the mismatch of crystallographic lattices at grain boundaries shorten the lifetime of injected electrons making them vulnerable to recombination with electrolyte [86]. Trapping severely affects diffusion length of electrons by decreasing it. For effective charge transport the diffusion length L_e must be much higher than the film thickness d [87]. For nanoparticles the diffusion length is $L_e \approx d$. However, one-dimentional (1D) vertically oriented

photoanode nanostructures such as nanotubes (NTs), nanorods (NRs), nanowires (NWs) can provide efficient charge transport increasing diffusion length up to 100 μm making $L_e >> d$ [85]. Martinson et al estimated that electron transport is 10 – 100 times faster in nanorod electrodes compared to nanoparticle photoanode [88].

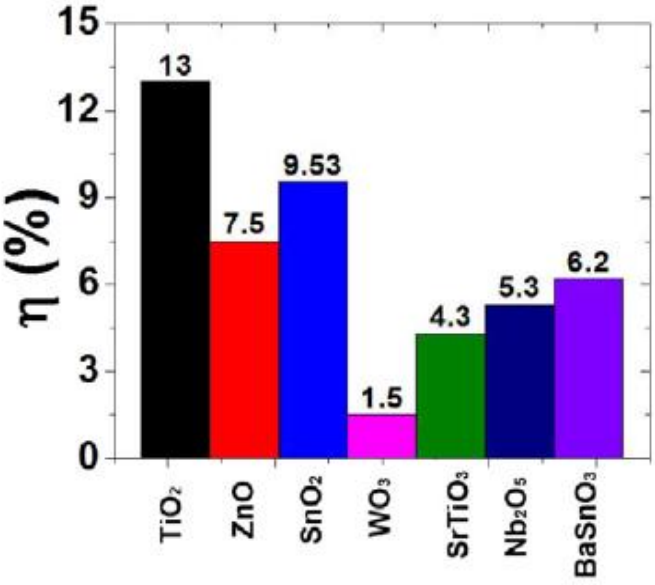

Figure 2. 12 Highest reported DSSC efficiencies for different photoanodes [53]

As a pioneering work Law et al made a comparative investigation of ZnO nanoparticle and nanowire based DSSCs to demonstrate high electron transport in 1D structured photoanodes [89]. The surface area of nanowire was one fifth of nanoparticle which resulted in lower dye uptake. The overall achieved efficiency of ZnO nanowire based cell was 1.5 %, limited by the surface area of the photoanode. Recent comparative study of ZnO nanoparticle and nanowire based DSSCs resulted in 6.2 % PCE for the former and 10 times less PCE for the latter [90]. The main reason of such low performance was poor light harvesting of ZnO nanowire due to an order of magnitude lower dye loading compared to nanoparticulate ZnO. Small dye loading in ZnO NWs resulted from electrostatic repelling forces between the photoanode surface and dye. Optimization of the dye pH to minimize the repelling helped to increase dye uptake and resulted in 1.84 % PCE. Other 1D nanostructures of ZnO photoanode such as nanotubes [91-92], nanorods [93] are also reported. However, their efficiencies are quite low. Branched 1D photoanodes are performing much better, on the other hand. Chen and Yang reported the use of ZnO nanotetrapod photoanodes (Fig.2.13)

which demonstrated outstanding charge collection [94]. The film with thickness up to 30 µm did not require calcination and produced 10.31 mA/cm^2 photocurrent leading to 3.27 % efficiency. The composite photoanode obtained by mixing ZnO nanotetrapod with SnO_2 nanoparticles showed higher efficiency, 6.31 %. It was concluded that the nanotetrapod was responsible for elevated electron transport due to minimal to moderate grain boundaries.

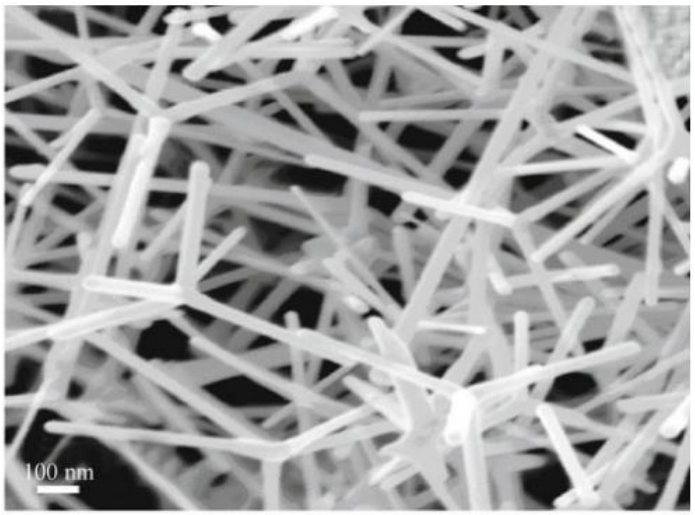

Figure 2. 13 SEM image of ZnO nanotetrapods [adopted from 94]

The use of 1D SnO_2 based photoanodes was also reported widely. It is said that SnO_2 NW based cells generated higher photovoltage than their nanoparticle based counterparts [95]. This was explained with faster electron transport, slower recombination kinetics and lower work function of SnO_2 NWs. Huo et al presented SnO_2 nanorod and TiO_2 based composite photoanode that showed 6.98 % efficiency, higher than when the nanorod (3.95 %) and P25 (5.27 %) were used separately [96]. The authors claim that this was thanks to superior light scattering effect, suppressed charge recombination and elevated dye loading.

The use of composite morphologies is reasonable since 1D nanostructures suffer from minimal dye loading and the composites may offer both increased dye uptake and faster electron transport. In 2013 Wu et al demonstrated hierarchical anatase TiO_2 nanowire arrays as a new photoanode for dye-sensitized solar cells [86]. The photoanode is composed of long TiO_2 NW trunk and numerous short TiO_2 NR branches. This showed outstanding performance compared to its 1D TiO_2 counterparts which exhibited low specific surface area due to huge diameter and broad gaps between NWs. Interestingly, electron

transport and recombination were found to be inferior to TiO_2 NWs due to additional trap states and recombination centers; however, because of better light scattering property and increased surface area which can accommodate more dye molecules were responsible for high photocurrent and efficiency 7.34 %. A year later, this research group developed multi-layered ultra-long anatase TiO_2 nanowire arrays (MTNWs) on FTO surface using hydrothermal method (Fig.2.14) [85]. A film with 47 μm thickness accommodated excellent properties such as high surface area, quick electron transport and noticeable light scattering ability and generated electricity with 9.40 % efficiency and established a new record. To compare, P25 based control cell demonstrated 7.23 % PCE due to its inferior light scattering and recombination.

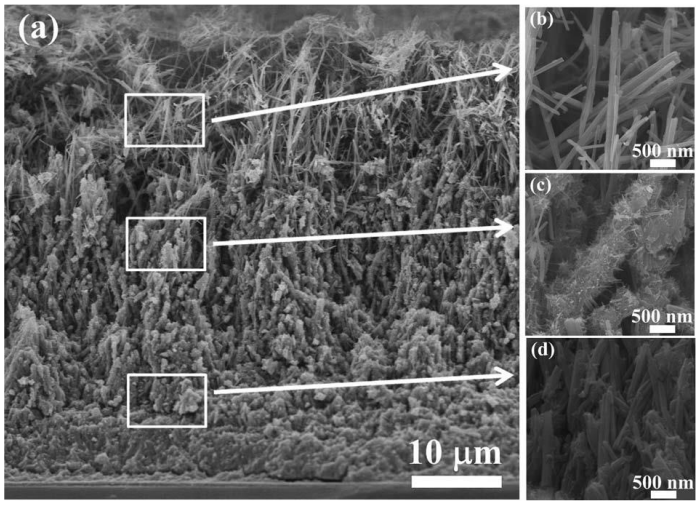

Figure 2. 14 Cross-sectional image of MTNWs composing of three layers (a, b and c) [85]

2.5.2 Dye

Photons are absorbed by dye molecules chemically bonded to the surface of the photoanode. Light absorption leads to the photoexcitation of electrons and their pumping into the conduction band of photoanode. The more light is absorbed by the dye molecules the higher is the photocurrent and hence the efficiency of solar cell. Therefore, the main requirements for the dye are

i) strong absorption in visible and near infra-red region;
ii) good bonding and coupling with the photoanode;
iii) efficient electron injection upon photoexcitation;
iv) efficient regeneration by the electrolyte;
v) high photo- and thermostability;
vi) good solubility in corresponding solvent;

vii) no toxicity;

viii) low cost.

The properties of dye depend on its structure. Many sensitizers have been investigated since the advent of dye-sensitized solar cells. All of them can be categorized into three groups:

a) Ru – complex dyes;
b) Metal-free organic dyes;
c) Natural dyes.

2.5.2.1 Ru-complex dyes

Ruthenium complex dyes are known from the start of DSSCs. They are considered among the best sensitizers. The first reported TiO_2 sensitized solar with 7.1 % efficiency cell used Ru-based dye ($RuL_2(\mu\text{-}(CN)Ru(CN)L'_2)_2$, where L is 2,2' bipyridine-4,4' –dicarboxylic acid and L' is 2,2'-bipyridine) [36]. In 1993, Nazeeruddin et al developed a new Ru complex labelled N3 (Fig.2.15) [49]. This dye with absorption threshold around 800 nm demonstrated quantitative IPCE over a wide spectral range and generated 17 mA / cm^2 photocurrent at AM1.5 with 10 % PCE. Four years later black dye was developed by Nazeeruddin et al, with three thiocyanato and three carboxyl groups [97]. The IPCE of the black dye extended to near – IR region and the efficiency reached 10.4 %. In 2005, Nazeeruddin et al modified N3 dye structure into novel N719 dye by doubly protonating it (Fig.2.15), which performed much better than the former demonstrating remarkable 11.18 % efficiency at 1 sun [98].

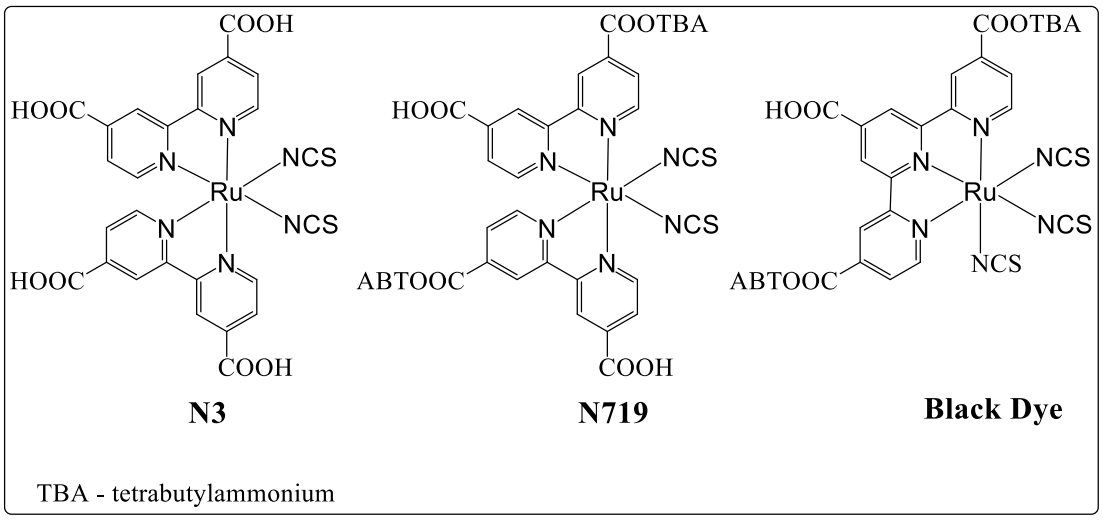

Figure 2. 15 Chemical structures of highly efficient Ru – based sensitizers

2.5.2.2 Porphyrin dyes

Although Ru – complex dyes show outstanding performance in DSSCs, their widespread application may be obstructed by the limited supply and elevated cost of ruthenium metal. Therefore, it is rationale to use cheap alternatives. Multitude of metal – free and / or cost – effective metal containing sensitizers have been studied. Porphyrin dyes, in this regard, are unique due to their excellent properties such as strong light absorption around 400 – 450 nm (Soret band) and moderate light absorption at 600 – 650 nm (Q band); suitable energetics for charge injection and regeneration; its properties can be tuned via chemical methods; porphyrin has several places to form chemical bonds; good solubility in common organic solvents.

The sensitization of TiO_2 with porphyrin based dyes was known earlier. For example, in 1987 Kalyanasundaram et al reported TiO_2 sensitization with [tetrakis(4-carboxyphenyl)porphyrinato]zinc(II) and efficient charge injection from excited state of the dye to the conduction band of TiO_2 [99]. However, the pioneering work on porphyrin sensitized solar cells was reported in 1993 by Kay and Gratzel with cell efficiency value 2.6 % [100]. Within a decade (1993 – 2003) the efficiency of porphyrin sensitized solar cells (PSSCs) did not increase significantly [101]. In 2005 Wang et al reported the use of **Zn-3** porphyrin sensitizer (Fig.2.16) with overall efficiency 5.2 % when the dye was used alone and 5.6 % when it was used with chenodeoxycholic acid (CDCA) as aggregation inhibitor [102]. Two years later the PCE of porphyrin based DSSCs increased to 7.1 % with the use of another β-functionalized porphyrin dye **2** (Fig.2.16) [103].

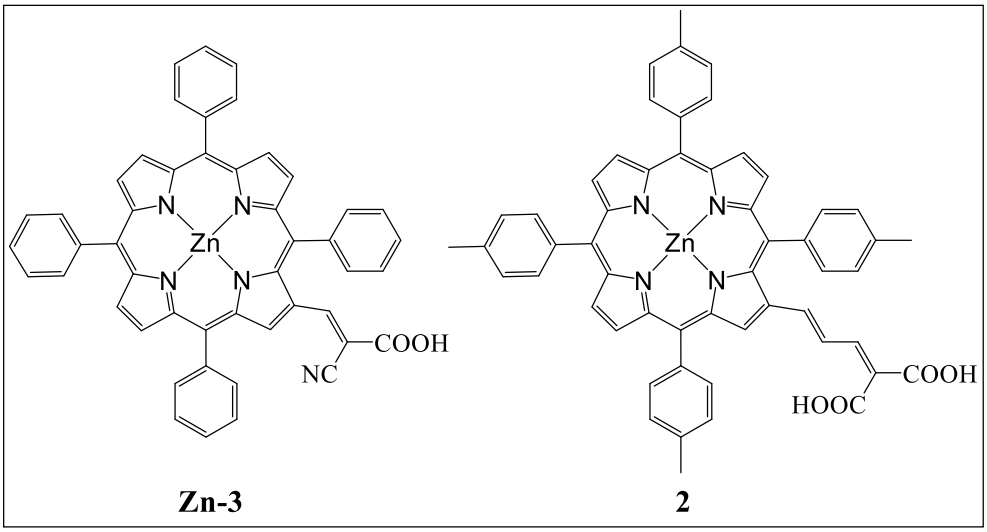

Zn-3 **2**

Figure 2. 16 Chemical structures of early porphyrin sensitizers

One of the reasons of porphyrin sensitizers showing lower efficiency compared to Ru-based dyes was their poor light harvest at around 500 nm and at near IR region. To improve the light absorption of porphyrin sensitizers it was necessary to increase the π – conjugation of the molecule. This led to the development of push – pull porphyrins or so called D-π-A type sensitizers where D is electron donating group, π is highly conjugated spacer and A is electron acceptor moiety. In 2009 the group of Professor Diau reported the use of D-π-A type porphyrin sensitizers in DSSCs (Fig.2.17) [104]. Due to aggregation the cell efficiencies were low when the dyes were used alone. To suppress dye agglomeration the sensitizers were used together with CDCA (1:2 ratio) and demonstrated 4.53 % and 6.54 % PCE for **YD0** and **YD1**, respectively. However, the presence of CDCA had negative effect on **YD2** dye due to decreased injection efficiency. When used alone **YD2** demonstrated improved efficiency compared to **YD1** and reached 6.76 %.

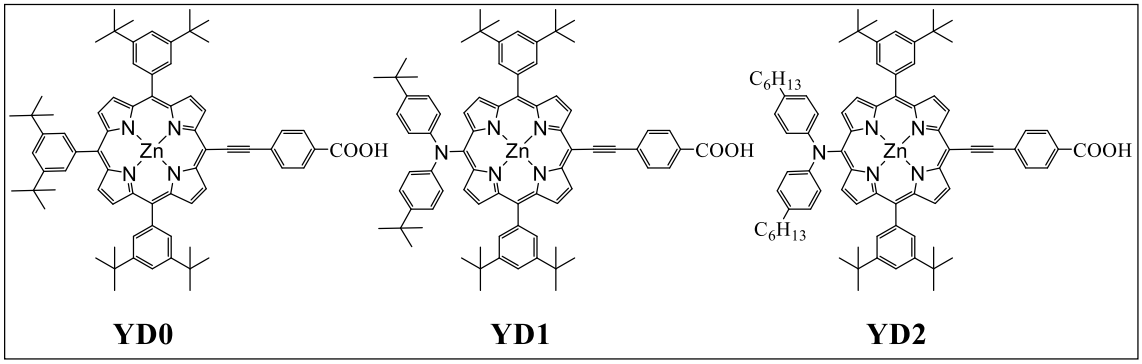

Figure 2. 17 YD push-pull porphyrin sensitizers

A year later the photovoltaic performance of **YD2** sensitized solar cell was improved to 11 % in collaboration with the group of Professor Gratzel [105]. This was a first incident when a PSSC demonstrated PCE above 10 %. Such an outstanding performance was achieved through co-sensitization of **YD2** with the mixture of D205 dye and CDCA. D205 has absorption peak at 532 nm where porphyrin sensitizer **YD2** shows minimal absorption. Co-sensitization allowed improved light harvest around 500 nm and boosted IPCE improving cell performance (Fig.2.18) [105].

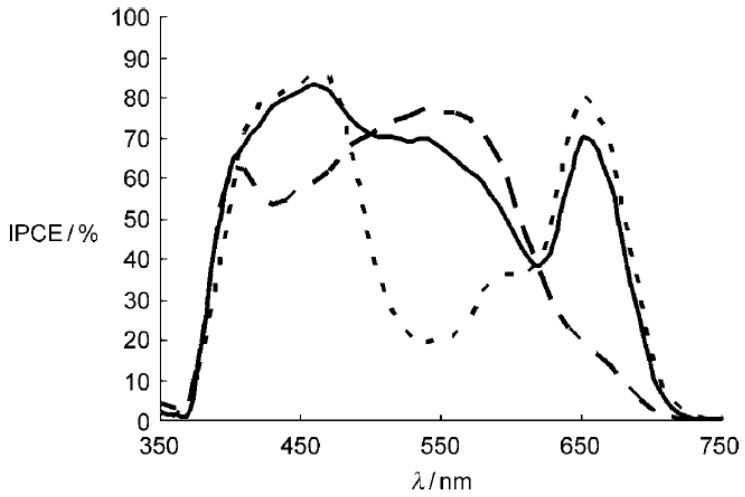

Figure 2. 18 IPCE spectra of YD2 (dotted line), C205 (dashed line) and YD2/C205 (solid line) [105]

The concept of alkoxy – wrapped dyes also affected the further development of porphyrin based sensitizers. It was reported that the presence of alkoxy groups notably reduced charge recombination [106]. Although the butyl group in **YD2** suppressed the dye aggregation, it could not prevent recombination. It is assumed that the presence of metal cation, Zn^{2+}, attracts I_3^- species and increase charge recombination with the electrolyte [107]. Therefore, protecting the porphyrin core was expected to reduce recombination. In this regard, Yella et al introduced octyloxy-wrapped analog of **YD2** dye labelled as **YD2-o-C8** (Fig.2.19) in 2011 [44]. This dye performed much better compared to **YD2** and demonstrated PCE value of 11.9 % against 8.4 % for the latter at AM1.5 using new $Co^{(II/III)}$tris(bipyridyl) electrolyte. The use of this redox mediator allowed V_{OC} to approach 1 V. When co-sensitized with triphenylamine based dye **Y123**, the cell efficiency was increased up to 12.3 % [44]. Mathew et al further modified the structure of **YD2-o-C8** dye introducing new donor and acceptor moieties to obtain **SM315** sensitizer (Fig.2.19) [45]. The presence of benzothiadiazole acceptor group allowed broadening and red-shifting of light absorption. With the use of cobalt (II / III) bipyridine complex as redox electrolyte and **SM315** dye alone the cell demonstrated 13 % outstanding efficiency. At the same time, the same group developed another porphyrin dye **GD50** (Fig.2.19) which showed comparable efficiency to **SM315** sensitizer [108]. The authors claimed that the introduction of benzothiadiazole group improved the light absorption between Soret band and Q band eliminating the use of co-sensitizer.

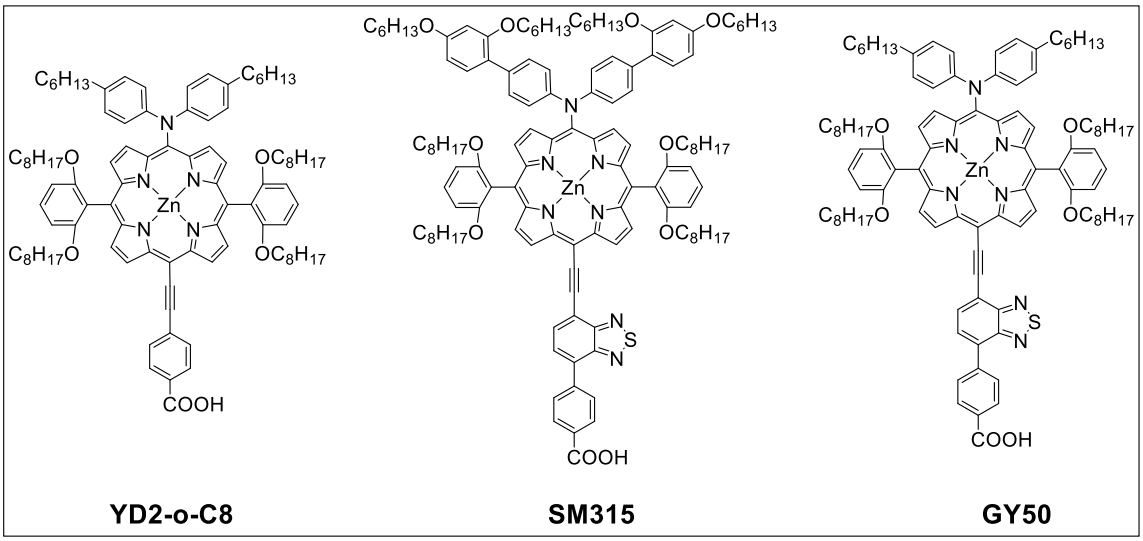

Figure 2. 19 Best – performing alkoxy – wrapped porphyrin dyes

Thus, porphyrin based sensitizers proved to be as much efficient as Ru – complex dyes. Porphyrin dyes like **SM315** and **GD50** even outperformed Ru sensitized DSSCs. These achievements were possible due to careful tuning of HOMO – LUMO energetics and light harvesting properties of porphyrin sensitizers [109].

2.5.2.3 Phthalocyanine dyes

Another class of sensitizers similar to porphyrins is phthalocyanines. Phthalocyanines are highly conjugated planar molecules with 18 delocalized π-electrons which has strong absorption in red / near IR region (Q band) and in UV / blue region (Soret band) of solar spectrum. Light harvesting at near IR region makes them attractive for solar cell applications as red / NIR sensitizers. Moreover, they possess good thermal and chemical stability which is one of the main requirements of DSSC dyes [110]. However, as light harvesters they show moderate efficiency in DSSCs. Fig.2.20 depicts the best performing phthalocyanine dyes so far with their corresponding efficiencies.

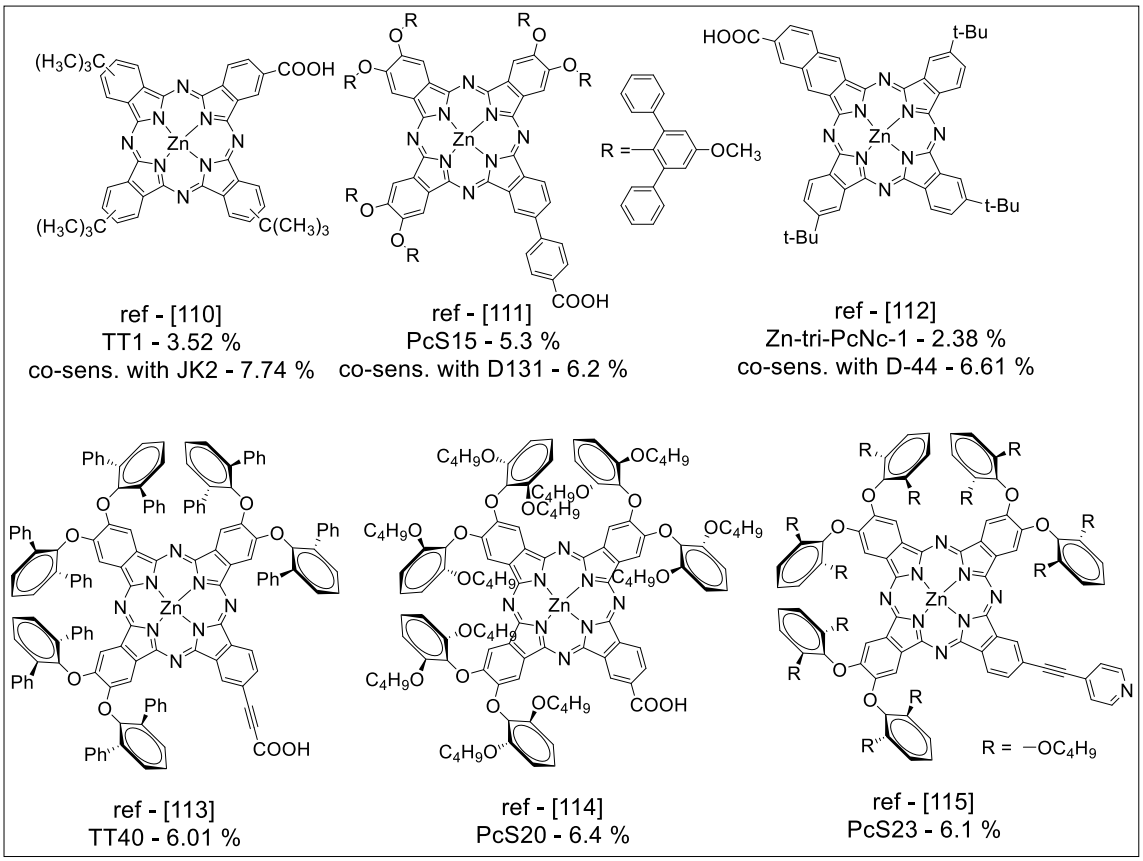

Figure 2. 20 Best – performing phthalocyanine dyes

The major reason for modest performance of phthalocyanine sensitized solar cells is the reduced electron injection and exciton deactivation caused by strong aggregation of phthalocyanine dyes [110]. In many cases chenodeoxycholic acid is used together with phthalocyanine dyes to reduce dye agglomeration. The ratio of dye / CDCA may reach 1 / 3000 [117]. This shortens the amount of adsorbed dye cutting down the photocurrent. Another drawback of phthalocyanines as sensitizers is their low – lying LUMO which minimizes free energy needed for electron injection and hence affects J_{SC} [110].

2.5.2.4 Triphenylamine dyes

The non-planar structure of triphenylamine makes it aggregation resistant. Moreover it has finest electron donating ability which makes it favored material in organic photovoltaics [118]. Kitamura et al were among first to introduce triphenylamine (TPA) based dyes to DSSCs [119]. They developed D-π-A sensitizers **1b** and **2b** with TPA as electron donating group and cyano carboxylic group as the acceptor. Methine units served as π – bridge (Fig.2.21). They showed 3.3 and 5.3 % PCE, respectively.

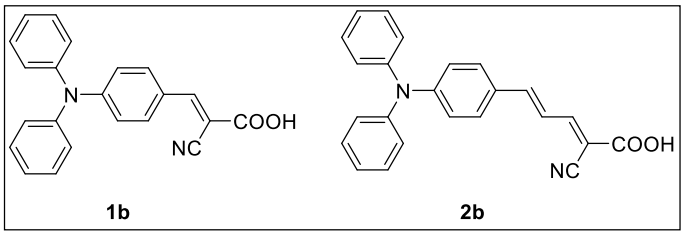

Figure 2. 21 Pioneering triphenylamine dyes

Later in 2005 Velusamy et al introduced benzothiadiazole group as the π – bridge to develop **S1** dye which demonstrated 3.77 % efficiency [120]. The structures of dyes with benzothiadiazole bridging unit are shown in Fig.2.22. Tang et al attempted to increase molecular conjugation by adding two thiophene moieties with BTD unit in between and the obtained dye BzTCA showed 6.04 % PCE [121]. Similarly, Lee et al reported several TPA dyes with π-extended benzothiadiazole group [122]. The BTD bridge was connected with TPA unit through single (**HKK-BTZ1**), double (**HKK-BTZ2**) and triple (**HKK-BTZ3**) bonds and in addition alkoxy donating group was introduced to the TPA (**HKK-BTZ4**). The dyes were used in mixture with deoxycholic acid to retard aggregation and the cell efficiencies were 5.72 %, 3.37 %, 4.55 % and 7.30 %, respectively. Better performance of **HKK-BTZ4** was explained with the presence of strong alkoxy donating groups which red-shifted the absroption and suppressed dye agglomeration [122]. In 2014 Yigit et al attempted to further elaborate on the sensitizer **HKK-BTZ4** structure introducing phenyl (**MZ-255**) and thiophene (**MZ-259**) units to the acceptor part and also attaching hexyl chains to thiophene units of **HKK-BTZ4** [123]. Due to better conjugation of thiophene **MZ-259** showed red shift in light absorption, better electron donating and charge separation; hence, **MZ-259** demonstrated 3.81 %, whereas **MZ-255** showed 3.16 % PCE.

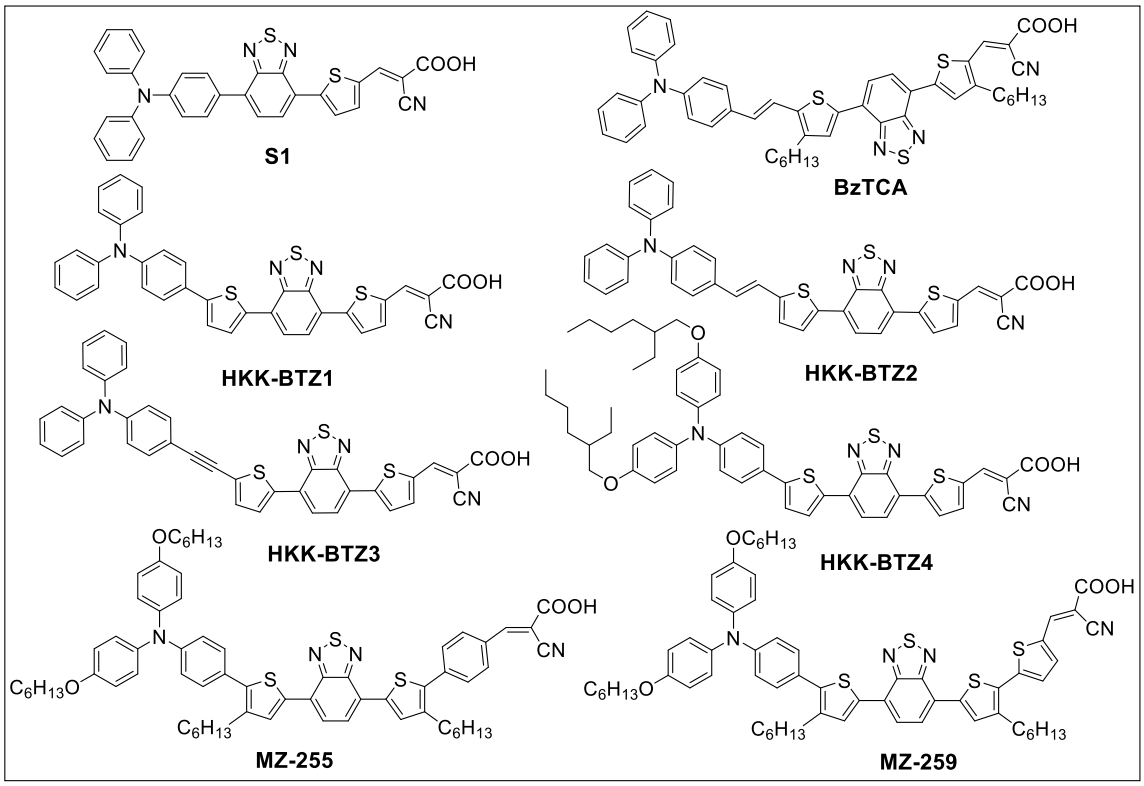

Figure 2. 22 Benzothiadiazole bridged triphenylamine dyes

The performance of TPA dyes with fused ring building blocks were further improved due to wide spectral response. Some of the highly efficient dyes with fused thiophene units are shown below with reported PCEs (Fig.2.23).

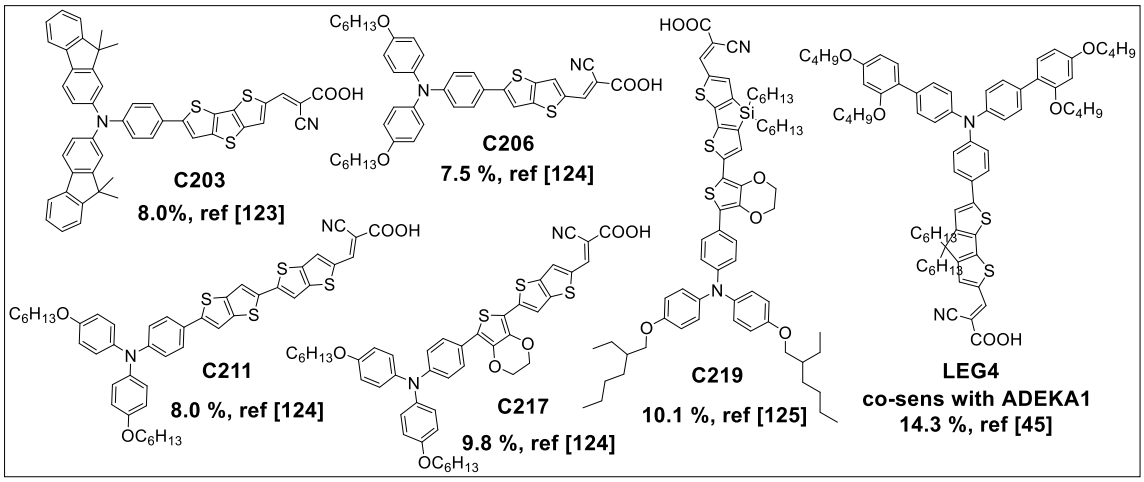

Figure 2. 23 TPA dyes with fused ring building blocks

2.5.2.5 Triazatruxene dyes

Triazatruxenes are π-extended delocalized systems which consist of three indole moieties fused with one benzene ring. Presence in the ring of nitrogen atoms makes them excellent electron donors. Qian et al, for the first time,

reported triazatruxene based dyes applied in DSSCs [127]. The sensitizer **TD1** (Fig.2.24) with thiophene acceptor unit demonstrated 6.1 % efficiency due to high photocurrent. Later in 2018, the same group reported triazatruxene dyes with benzothiadiazole bridge **JY43 – 46** (Fig.2.24) [128]. The authors stated that the presence of ethynyl unit and cyaniacrylic acid in dye structures boosted light absorption and elevated J_{SC}. Overall, dyes **JY43 – 46** showed efficiency values 7.51 %, 7.15 %, 6.50 % and 7.26 %, respectively. Recently, the group of Hagfeldt and Sun reported a new record power converting efficiency for single dye DSSCs with value 13.6 % [129]. The dye is made of triazatruxene as donating group, thiophene linked benzothiadiazole π – extended through ethynyl moiety as conjugated bridge and carboxylic acid as acceptor, and labelled ZL003 (Fig.2.24). 20.73 mA / cm^2, 0.956 V and 68.5 FF were obtained with cobalt electrolyte and Pt – based counter electrode. The dye was noted with remarkably fast electron injection into TiO_2 conduction band.

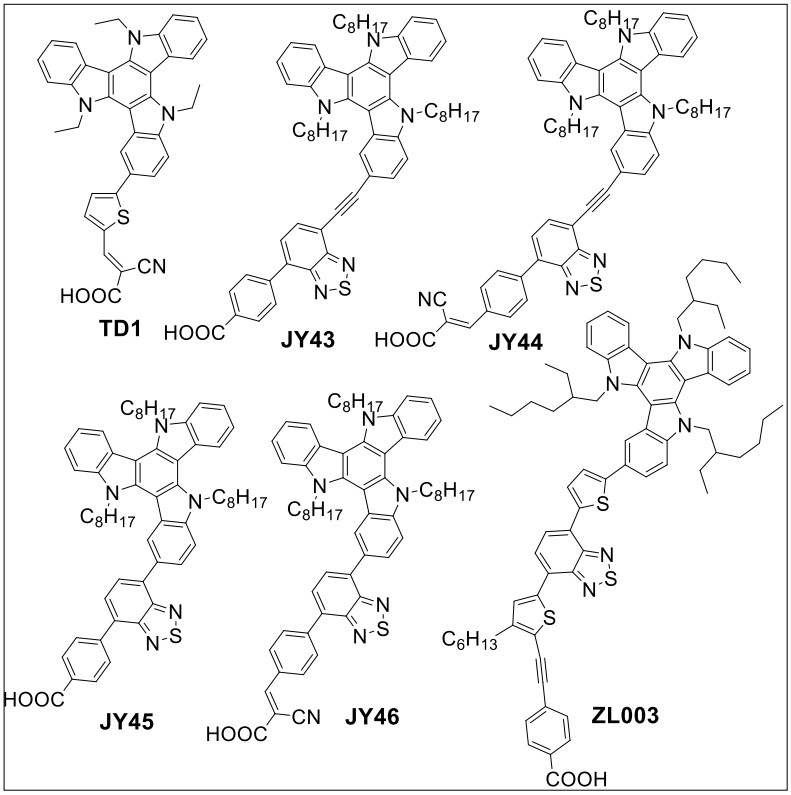

Figure 2. 24 Triazatruxene based sensitizers

2.5.3 Electrolyte – Hole Transporting Media

Electrolyte is a component of DSSCs responsible for charge carrier transport between two electrodes. It regenerates oxidized dye and carries the holes to the counter electrode. To do so it must have good interfacial contact with the photoanode and the counter electrode, and must be highly conductive to provide fast charge carrier diffusion between the electrodes. Moreover, it should not interfere with the light absorption of the sensitizer. In addition, the electrolyte should be thermo-, photo- and chemically stable to guarantee long term stability of the cell. Three types of electrolytes are known that are used in DSSCs: 1) liquid state; 2) quasi-solid state and 3) solid-state electrolyte.

2.5.3.1 Liquid electrolytes

This type of electrolyte is widely used in DSSCs and so far produced the highest cell efficiency [46, 129]. The main components of liquid electrolyte are solvent, ionic conductor and electrical additives.

Solvent acts as a media to dissolve and diffuse ionic conductor. An ideal solvent should meet following requirements: i) complete dissolution of electrolyte salts; ii) it should not boil or freeze under operating conditions; iii) low viscosity to allow diffusion of electrolyte species; iv) it should not remove / dissolve dye from semiconductor surface and the sealant; v) no toxicity and vi) low cost. Since it is difficult to find a solvent which can satisfy all the mentioned requirements, usually mixture of solvents is used. One of the extensively used solvent mixture is acetonitrile / valeronitrile with different ratios [130-131]. Ionic liquids are also used as solvent in DSSC liquid electrolyte and show remarkable results [132].

Iodide / triiodide couple is a commonly used ionic conductor in liquid electrolyte because it provides high conductivity, fast dye regeneration, good penetration into mesoporous film and its redox potential has favorable matching with many dyes. In DSSCs iodide species regenerate photo – oxidized dyes (eq.2.9-2.10), whereas triiodide species are catalytically reduced / regenerated to iodide at counter electrode (eq.2.11). Usually for the sake of fast dye regeneration the concentration of iodide species is higher compared to that of iodine.

$$S^+ + I^- \rightarrow [S\cdots I] \xrightarrow{I^-} S + I_2^{-*} \xrightarrow{I_2^{-*}} S + I_3^- + I^- \quad (2.9)$$

$$S^+ + I_2^{-*} \rightarrow [S\cdots I_2] \xrightarrow{I^-} S + I_3^- \quad (2.10)$$

$$I_3^- + \bar{e} \rightarrow I^- + I_2^{-*} \xrightarrow{\bar{e}} 3I^- \quad (2.11)$$

Although iodide / triiodide redox couple demonstrates remarkable performance in DSSCs it has several disadvantages which limit its use. First, I^-/I_3^- based cells have problems related to long term stability due to the corrosive nature of the couple [133]. Another major issue is the loss of potential due to huge difference between the redox potential of iodide / triiodide and the HOMO of dye [134]. For dye regeneration purpose 0.2 – 0.3 eV of driving force is enough [135], therefore, this led researchers to search for alternative ionic conductors with lower redox potentials. Some of the studied alternatives with more positive redox potentials are bromide / tribromide (Br^-/Br_3^-) [136], SCN- / $(SCN)_3$- and SeCN- / $(SeCN)_3$- [137] redox couples. The best alternative to iodide / triiodide couple so far is Co (II/III) redox couple which was introduced in 2001 [138]. The application of Co (II/III) bipyridine complex (Fig.2.25) as ionic conductor allowed photovoltage values close to 1 V [45-46, 129].

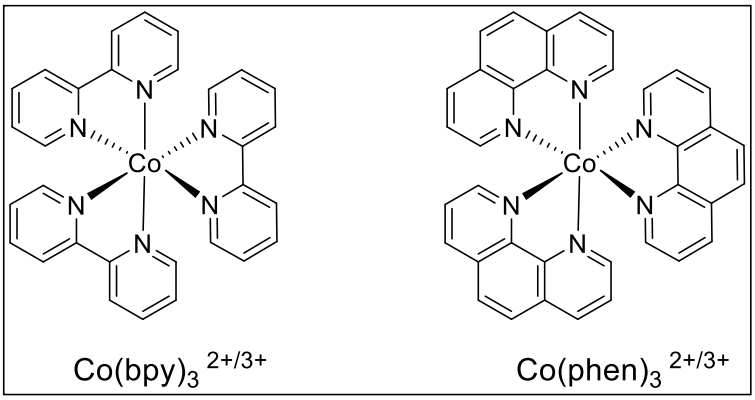

Figure 2. 25 Structures of Co (II/III) complexes

The third component of liquid electrolytes is electrical additives. These are responsible for tuning the semiconductor surface states, conduction band edge movement, rate of back electron transfer and photovoltaic parameters of DSSCs. 4-tert-butyl pyridine (TBP) is added to electrolyte because its presence is known to improve photovoltage V_{OC} [49]. It is reported that TBP can reduce the rate of recombination by 1 – 2 orders of magnitude [40] and shift the conduction band edge of TiO_2 in negative direction [139]. Some suggested that TBP has combined effects of upward shift of TiO_2 conduction band and prolonging lifetime of injected electrons [140].

Another group of additives are used in electrolytes to obtain higher photocurrent. Such components are cations like Li^+ and guanidinium ($C(NH_2)_3^+$ = G^+). The presence of lithium cations leads to downward movement of TiO_2 conduction band edge, thus improving electron injection and J_{SC} [141-142]. Guanidinium cation (G^+) also demonstrates similar improvement in J_{SC} by boosting electron injection [143]. It is reported that G^+ can reduce dark current [144]. Some results suggest that the presence of G^+ may reduce recombination by factor of 20 [145].

Nevertheless, the main limiting factor of liquid – state electrolytes is the poor stability of solar cell caused by the leakage of the electrolyte and difficulty of sealing. To overcome this, quasi – solid state electrolytes were developed.

2.5.3.2 Quasi – solid electrolytes

Quasi – solid is a state between liquid and solid. Quasi-solids are also known as semi – solids. This type of electrolyte possesses characteristics of both liquid electrolytes like high diffusivity and of solid electrolytes like better long term stability. The general method preparation of quasi-solid state (QSS) electrolytes is based on gelation of liquid electrolyte in organic / inorganic gelators. Therefore, the composition of QSS electrolyte is gelator (polymer, oligomer, TiO_2, SiO_2, ZnO, etc.), organic solvent and inorganic salt. The polymer acts as a framework or a matrix to hold the ionic conductor solution. Wu et al reported QSS thermoplastic gel electrolyte (TPGE) consisting of polyethylene glycol (40 wt %) as a gelator, propylene carbonate (60 wt%) as solvent and 0.65 M KI and 0.065 M I_2 as ionic conductor [146]. The DSSCs prepared from TPGE generated electricity with 7.22 % efficiency at 100 mW / cm^2. Generally, high polymer gel content negatively affects the ionic conductivity of the electrolyte. In this regard, Komiya et al presented three dimensional polymer network as gelator with only 7 wt% and 0.2 M DMPII, 0.5 M LiI, 0.05 M I_2 as ionic conductors in ethylene carbonate and γ-butyrolactone (30:70 v/v) solvent system which demonstrated high ionic conductivity 9 mS/cm [147]. The cell with novel QSS electrolyte showed higher photovoltage than liquid electrolyte based cell and impressive 8.1% PCE under AM1.5. Addition of inorganic gelator to QSS electrolytes may enhance diffusion of ionic conductors. Thus, a composite QSS electrolyte was obtained via mixing TiO_2 nanoparticles and poly(vinylidenefluoride-co-hexafluoropropylene) based gel electrolyte [148]. The addition of inorganic

nanoparticle led to improvement of PCE from 5.72 % to 7.18 % which was ascribed to the increase of diffusion coefficient of I_3^- species.

2.5.3.3 Solid – state electrolytes

The presence of solvent in QSS electrolytes still causes problems related to stability. Solvent evaporation is unavoidable at long term storage. Therefore, solid – state electrolytes (SSE) are more advantageous.

In SSE, the ionic conductor is replaced by hole transporting material (HTM) or p – type semiconductor. A perfect HTM should i) have appropriate energetics to transfer holes from oxidized dye to counter electrode, ii) be able to form good interface with mesoporous semiconductor, iii) have high hole mobility, iv) not absorb in the visible region. The examples of p – type semiconductors are CuI, CuBr, CuSCN, Cs_2SnI_6, organic polymers, etc [149-152]. However, the performance of solid – state DSSCs was inferior to liquid DSSCs. Major reasons are slow charge carrier mobility and poor interface due to improper pore filling. In 2017, the group of M. Gratzel reported a record 11 % PCE for ss-DSSCs [153]. They presented a novel solid electrolyte based on Cu (II/I) complex: [Cu (4,40,6,60-tetramethyl-2,20-bipyridine)$_2$](bis(trifluoromethylsulfonyl)imide)$_2$ and [Cu (4,40,6,60-tetramethyl-2,20-bipyridine)$_2$](bis(trifluoromethylsulfonyl)imide) (Fig.2.26).

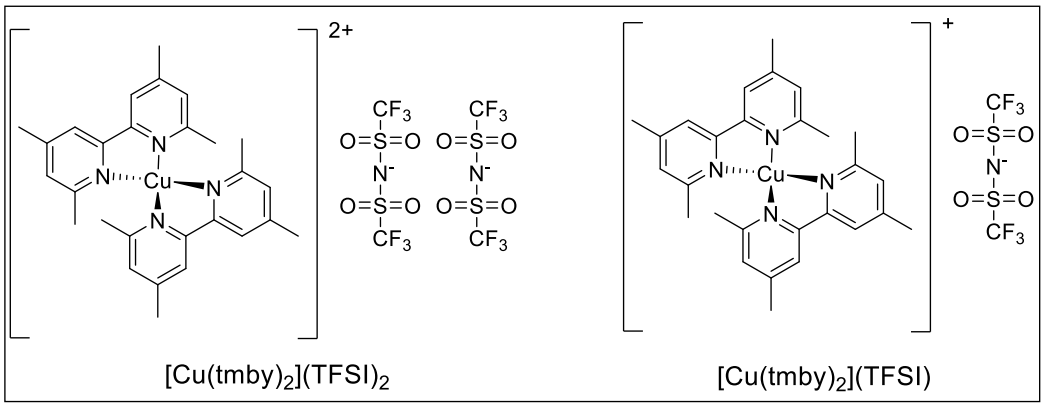

Figure 2. 26 Structures of solid state electrolyte based on Cu (II/I) complexes

The redox potential of Cu (I) is 1.07 V vs SHE, whereas the redox potential of the dye Y123 is 0.87 V vs SHE giving 0.2 V potential difference for dye regeneration. The electrolyte was composed of 0.06 M [Cu(tmby)$_2$](TFSI)$_2$, 0.2 M [Cu(tmby)$_2$](TFSI), 0.1 M LiTFSI and 0.6 M 4-tert-butylpyridine (TBP) in acetonitrile. To obtain solid electrolyte the solvent was slowly evaporated

through the predrilled hole which resulted in better interface between the electrolyte / semiconductor and higher conductivity.

2.5.4 Counter Electrode

The function of counter electrode is to regenerate oxidized electrolyte and this is done by receiving electron from outer circuit and passing it to the redox media (HTM). For efficient electron flow the counter electrode (CE) must have low internal resistance. Additionally, it should have high catalytic activity, vast surface area, physical and chemical stability, resistance to corrosion, perfectly matching energetics with the redox potential of the redox mediator and low cost. In general counter electrode is a thin film of catalytic material on a conductive substrate (e.g. FTO glass). Traditionally, the catalytic material used is Pt. Since Pt is very expensive and scarce, this will restrict its use when it comes to large scale production. Moreover, the performance of DSSCs with Pt CEs deteriorates with time. One of the reasons is that Pt is washed away into the electrolyte and / or oxidized. The dissolved species, even in tiny amount, may land on the photoanode and lead to short-circuiting of the cell [154]. Furthermore, the liquid electrolyte may cause the oxidation of Pt to form PtI_4 causing the change of redox electrolyte concentration [155-158]. The formation of ionic species like Pt(II) and Pt(IV) may result in significant increase of the charge transfer resistance of counter electrode R_{CT} [159]. Hence, one of the important tasks of DSSC technology is the substitution of Pt with more abundant, cost – effective and easy to prepare material.

2.5.4.1 Metals and metal alloys

Since Pt demonstrates excellent catalytic property in regenerating oxidized redox mediator (I_3^-) the metals of Pt – group were investigated as a potential alternative to Pt CEs. Irridium in comparison with Pt is cheaper for 25 % and possesses exceptional stability [160]. For these reasons Ir – based CE was prepared with layer thickness of 46 nm and demonstrated 5.19 % efficiency; however, this was lower than the performance of Pt – based solar cell which showed 7.38 % PCE [160]. Mokurala et al reported radio-frequency sputtered Ir CE which exhibited 7.2 % PCE against 8.5 % of Pt CE due to lower J_{SC} and FF [161]. Cyclic voltammetry analysis indicated that the reduction of I_3^- to I^- in Ir – based DSSCs is slower compared to that of Pt – based cells. Higher R_{CT} value for Ir CE obtained from electrical impedance spectroscopy measurements confirmed slow

electron transport from Ir CE to the electrolyte. Another metal of Pt – group is ruthenium. Thus, Seok et al introduced a nanostructured Ru – based CE which was prepared by H_2 reduction of RuO_2 [162]. However, the photovoltaic performance of Ru CEs was inferior to that of Pt (6.77 % vs 7.87 %). Compared to a single metal an alloy of two or more metals can be superior due to multi effect. Metal alloys possess high conductivity, remarkable catalytic activity and they are cheap. Therefore, their use as CEs in DSSCs was studied extensively. In this regard, He et al prepared CoPt alloy CEs with different ratios of the metals via electrochemical codeposition method [163]. The CEs demonstrated excellent catalytic activity which was deduced from EIS measurements and all samples demonstrated better photovoltaic efficiency than Pt CE. An alloy with composition $CoPt_{0.02}$ showed the highest efficiency of 10.23 % which outperformed Pt – based cell with 6.52 % PCE. The same group later presented another alloy CE consisting of Ni and Se prepared by mild solvothermal method [164]. The NiSe CEs were found to be transparent which allowed bifacial irradiation of the DSSC. $Ni_{0.85}Se$ composition was found to be the best performing CE and demonstrated 7.85 % PCE when irradiated from front, 4.37 % from rear and 10.63 % from both sides. For comparison Pt reference cell showed 6.97 %, 3.56 % and 8.78 %, respectively. EIS analysis revealed strong catalytic activity of the alloy CE with R_{CT} = 2.96 Ωcm^2, whereas Pt CE exhibited 7.23 Ωcm^2 [164]. The components of alloy when used alone have poor photovoltaic performance. For example Co alone demonstrated 1.84 % [163], similarly Ni and Se showed 1.03 % and 4.86 %, respectively [164]. These observations reveal the synergistic effect of metals in alloy form. Thus, Zhao et al presented a Pt – free ternary RuCoSe alloy based counter electrode for DSSCs [165]. The alloy was prepared by electrodeposition method. The ternary alloy RuCoSe counter electrode demonstrated excellent electrocatalytic activity which resulted in 9.07 % PCE outperforming Pt reference cell 7.03 %.

2.5.4.2 Polymers

Conductive polymers are another group of materials that are studied as an alternative to Pt – based counter electrodes for DSSCs. Their properties like electrical conductivity, porosity, ease of preparation, abundance, reasonable price and good catalytic performance make them suitable as Pt-free counter electrodes. One of the polymers extensively studied as CE in DSSCs is poly(3,4-

ethylenedioxythiophene) or PEDOT (Fig.2.27). It is highly flexible and has wonderful conductivity and impressive stability. In addition it is cheap. In 1998 Yohannes and Inganäs discovered that PEDOT can catalyze the redox reaction of iodide / triiodide [165]. And later it was shown that PEDOT has high catalytic activity for its practical application as counter electrode in DSSCs [166]. Pringle et al prepared a cheap counter electrode based on PEDOT using electrodeposition method on flexible ITO-PEN electrode [167]. The polymer CE based cell demonstrated 8.0 % efficiency, whereas Pt – based DSSC showed 7.9 % PCE. The authors also noted very promising stability of PEDOT based cells. Trevisan et al reported nanostructured PEDOT CEs for DSSCs [168]. They used ZnO template based method of electropolymerization followed by removal of the template via acid washing. The obtained PEDOT nanotube arrays demonstrated better catalytic activity in reducing triiodide and outperformed flat PEDOT counterpart due to increased surface area. Its photovoltaic performance was identical to that of Pt – based cells showing 8.3 % PCE. Recently Kang et al presented bifacial DSSC with PEDOT counter electrode with unprecedented cell efficiency among bifacial DSSCs [169]. This was achieved by decreasing the film thickness of PEDOT while keeping high catalytic activity of the counter electrode. With Co (II/III) electrolyte PEDOT CE based cell outperformed Pt CE based DSSC demonstrating 8.65 % PCE vs 5.94 % of Pt for front irradiation and 7.48 % vs 4.86 % for back illumination.

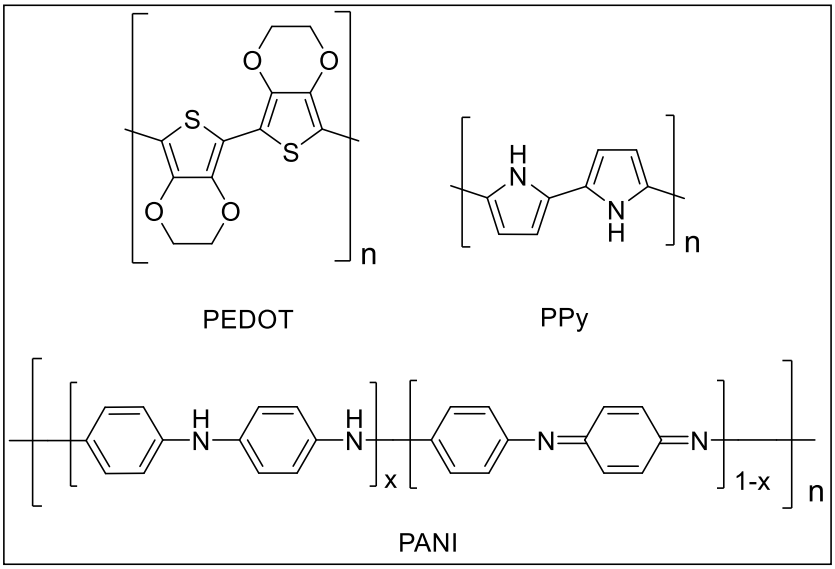

Figure 2. 27 Structures of conductive polymers

Polyaniline or PANI (Fig.2.27) is also promising material as counter electrode for DSSC application. It has high conductivity and both thermal and chemical stability. Also it is easily synthesized and cost – effective. For its notable properties PANI was first used as CE for DSSC in 2008 [170]. The PANI CE possessed microporous nature and in comparison with Pt CE it exhibited better electrocatalytic activity in reducing triiodide and lower charge transfer resistance. This led to 7.15 % PCE for PANI – based DSSC and this was higher than Pt – based cell which showed efficiency value of 6.9 %. PANI counter electrodes manifest excellent capability of regenerating Co (II/III) – based electrolytes as well. Wang et al applied PANI nanowires as counter electrodes for a DSSC with Co (II/III) electrolyte [171]. The NW CE was prepared in situ without template and demonstrated high electrocatalytic activity than its flat analog, and outperforms Pt – based cell in electrocatalytic capability and electrochemical stability. The efficiency of PANI NW CE – based cell was 8.24 %, whereas Pt CE – based DSSC showed 6.78 % efficiency. PANI counter electrodes are also suitable for bifacial applications due to good transparency. Wu et al demonstrated the application of PANI counter electrodes for DSSC in bifacial applications via improving photoelectric performance of the polymer film by modifying with 4-aminothiophenol [172]. The transparency of the modified PANI film was found better than conventional Pt film. With similar to Pt charge transfer resistance and electrocatalytic activity the modified PANI – based DSSC outperformed Pt control cell in bifacial performance showing 8.35 % PCE against 7.46 % of Pt.

Another conducting polymer as a candidate to substitute Pt CE is polypyrrole (PPy) (Fig.2.27). Polypyrrole have excellent thermostability up to 150^{o}C and its conductivity may range between 2 – 100 S / cm [173]. It is easily synthesized with high yields and has good catalytic activity. Due to such properties PPy has been studied extensively as Pt – free CE for DSSCs. Wu et al prepared porous PPy nanoparticles with particle size 40 – 60 nm and coated on FTO glass [174]. With the help of cyclic voltammetry they showed that PPy is better than Pt in charge transfer and electrocatalytic activity. This led to 7.66 % efficiency in PPy – based cell which was 11 % higher than Pt DSSCs. Similarly, Jeon et al reported nanoparticulate PPy with average size of 85 nm and electrical conductivity 10 S / cm [175]. To prepare CE the 5 % dispersion of PPy in methanol was drop casted on FTO glass substrate and to fine-tune the CE the

film was doped with HCl. The obtained CE demonstrated 7.73 % PCE which was inferior to Pt with 8.2 % efficiency. In general, although polypyrroles show good performance they suffer from high R_{CT} and imperfect conductivity. Moreover, their performance depends on treating and doping [173].

2.5.4.3 Carbonaceous materials

Carbon is one of the most abundant elements on Earth and its low cost, ease of preparation, high surface area, stability and electrical conductivity make the carbonaceous materials a promising candidate for Pt – free counter electrodes of DSSCs. They can regenerate both I_3^- to I^- [176-177] and Co (III) to Co (II) [178-179]. Moreover, they have various allotropic forms like carbon black [154, 180], mesoporous carbon [181], carbon nanotubes [182-183], graphene [184-185], graphite [186-187]. Graphene was successfully used as Pt – free counter electrode in record efficiency DSSCs. The counter electrode of the DSSC with record 13 % efficiency composed of SM315 porphyrin dye on TiO_2 and Co (II/III) electrolyte was made by drop casting a suspension of graphene nanoplatelets on FTO substrate and drying at room temperature [45]. Another record holding DSSC with PCE value 14.3 % was fabricated using TiO_2 working electrode covered with ADEKA-1 and LEG-4 dyes, $[Co(phen)_3]^{3+/2+}$ - based redox mediator and counter electrode made by graphene nanoplatelets covered gold treated FTO glass substrate [46]. Nevertheless, most of carbon based CEs have problems related to resistance like TCO contact resistance due to weak adhesion of carbonaceous materials to the substrate, bulk resistance of carbon material and diffusion resistance in the pores. In addition, carbonaceous materials may need substantial amount to deliver required catalytic activity [173].

2.5.4.4 Transition metal compounds

Transition metal compounds like oxides, nitrides, carbides and chalcogenides have excellent catalytic performance and similar electronic structures like noble metals. They are corrosion resistant and can work under harsh conditions [188-190]. These marvelous properties make them suitable for application in DSSCs as counter electrodes. Researchers have investigated many diversity of transition metal oxides, carbides and nitrides some of which prove to be a good candidate as Pt-free counter electrode [191-194]. The chalcogenides of transition metals (sulfides and selenides) also display promising results due to fitting properties. CoS based counter electrodes have been extensively studied

and considered one of the best Pt-free counter electrodes for DSSCs. It exhibits performance similar to Pt and sometimes it can be superior to the latter. This depends on its morphology and the method of preparation [195-200]. The morphology of some CoS materials can be seen in Fig.2.28. Nickel sulfides were also proven to possess notable catalytic activity in regenerating redox mediator. Depending on the synthetic procedure different structures and sizes of NiS particles were obtained with comparable to Pt CE performances [201-202].

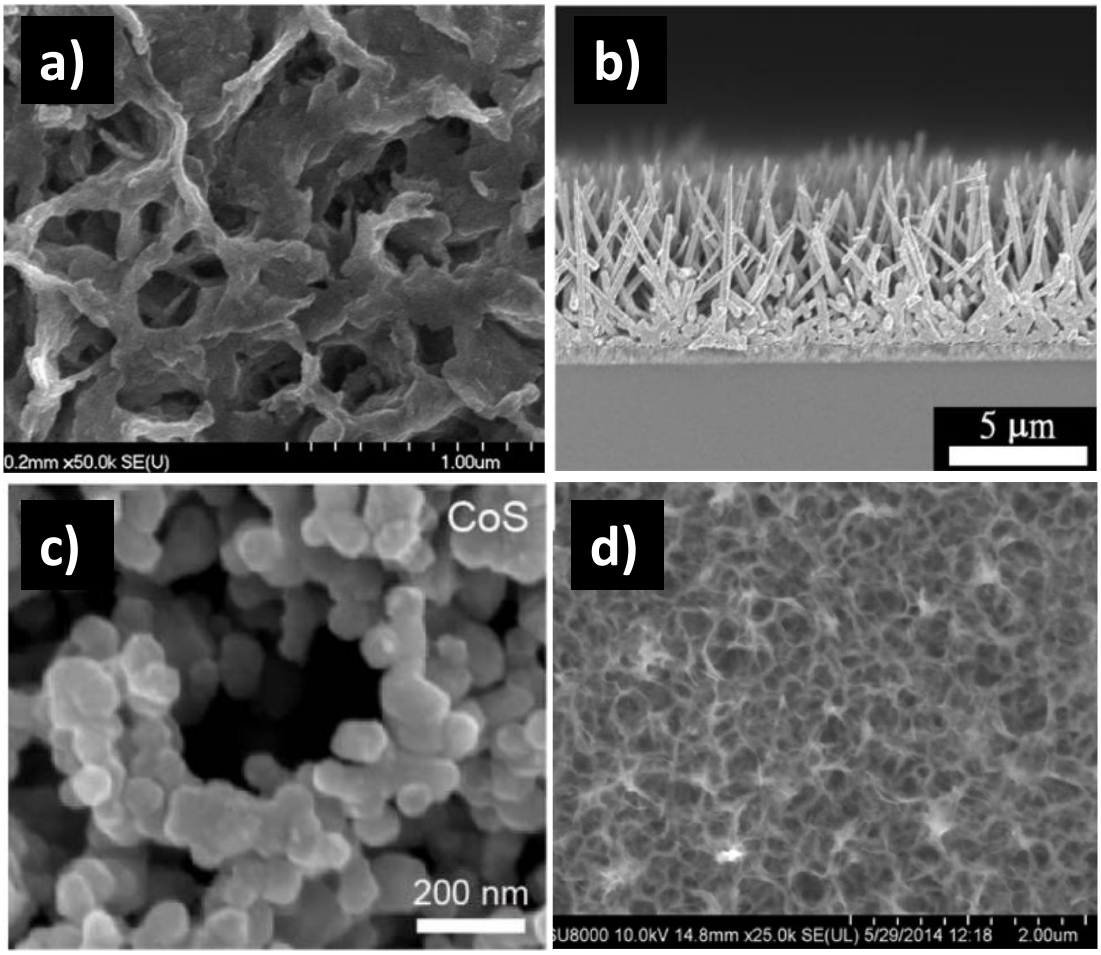

Figure 2. 28 SEM images of a) highly porous [196], b) nanorod arrays [197], c) nanoparticles [198] and d) honeycomb like [200] CoS counter electrodes

The substitution of sulfur to selen may increase the transparency of the material. Thus, Duan et al developed seleindes of transition metals (Co, Ni, Cu, Fe and Ru) as Pt – free CEs for bifacial irradiation using mild solution based synthesis [203]. All of the candidates outperformed control Pt cell in both front and back radiation tests. The highest efficiency was demonstrated by $Ru_{0.33}Se$ (9.22 % / 5.90 %) and Pt cell showed 6.18 % and 3.56 % for front and rear irradiation, respectively.

Recently, the interest of researchers shifted to ternary and quaternary sulfides. The presence of several metal centers greatly affects the quality of the product. It was shown that charge transfer is much higher in $NiCo_2S_4$ than in CoS and NiS [204]. Thus, Khoo et al prepared $NiCo_2S_4$ CE via one step hydrothermal method and the material exhibited 7.22 % PCE against 6.87 % of Pt cell due to remarkable charge transport and electrocatalytic activity [205]. Earlier, $CoNi_2S_4$ nanoribbon based CEs were also shown to be more effective than conventional Pt CE [206]. Some of the recently discovered ternary sulfides which demonstrated excellent performance in comparison with Pt are $Ni_{0.5}Fe_{0.5}S_2$ [207], $FeIn_2S_4$ [208], $NiIn_2S_4$ [209], $CoIn_2S_4$ [208-209].

Chapter 3

3 MATERIALS AND METHODS

3.1 Modification of the photoanode through surface doping with indium

3.1.1 Materials and synthesis

All the materials (chemicals, solvents and gases) used in this work were purchased from commercial sources and used without further purification unless otherwise stated. C264 triphenylamine dye (Fig.3.1) was synthesized according to the procedure presented by Wang and colleagues [210]. Determination of its molar mass was done using liquid chromatography-electrospray ionization-tandem mass spectroscopy (LC-ESI-MS/MS, Agilent 6420), while 1H and 13C nuclear magnetic resonance (NMR) spectra were analyzed in Varian VNMRS 500 in $CDCl_3$ solvent. The LC-ESI-MS/MS data for C264 dye is 699.8 m/z. ^{1}H NMR (500 MHz, CDCl3): δ = 8.30 (d, J = 8.6 Hz, 2H), 8.12 (d, J = 8.6 Hz, 2H), 7.85 (d, J = 6.8 Hz, 3H), 7.77 (d, J = 7.6 Hz, 1H), 7.15 (d, J = 9.0 Hz, 4H), 7.07 (d, J = 8.8 Hz, 4H), 6.87 (d, J = 8.8 Hz, 4H), 3.96 (t, J = 6.6 Hz, 4H), 1.81 (m, 4H), 1.49 (m, 4H), 1.37 (m, 8H), 0.93 (m, 6H); ^{13}C NMR (126 MHz, CDCl3): δ = 171.16, 155.85, 15.09, 153.93, 1949.29, 12.90, 140.17, 134.23, 130.65, 130.49, 129.84, 129.21, 129.00, 128.52, 128.26, 127.16, 126.59, 119.40, 115.34, 68.27, 31.62, 29.33, 25.78, 22.78, 14.07.

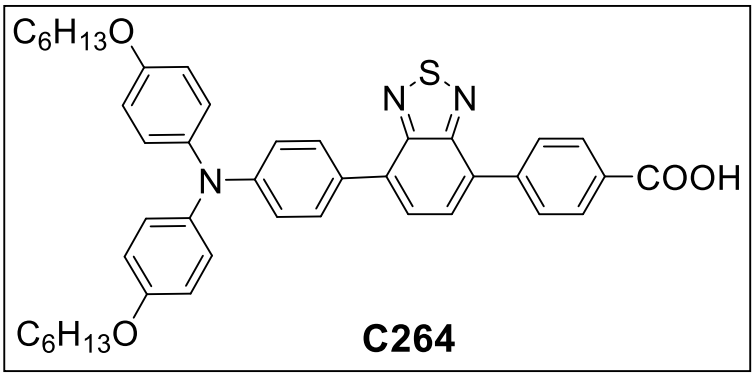

Figure 3. 1 Structure of C264 triphenylamine dye

3.1.2 Cleaning of FTO glass electrodes

The FTO glass substrates were purchased from Dyenamo (DN-HB06, surface resistance 15 Ω/sq, thickness 2.2 mm). Prior to use the substrates were cleaned to remove any dirt from the surface via sequential sonication for 30 min in soap, DI water, acetone and ethanol. The FTO substrates to be used as counter electrodes were cleaned the same way as mentioned except sonication in 0.1 M

HCl solution for 30 min after cleaning with acetone. Cleaned substrates were always kept in ethanol. Prior to film application the substrates were dried using N_2 gas flush under ambient conditions.

3.1.3 Preparation of indium surface doped TiO_2 photoanode

The clean and dry FTO substrates were put in a 50 mM solution of $TiCl_4$ at 70^{o}C for 30 min and the substrates were removed and sintered at 500^{o}C for 30 min with 5^{o}C/min heating rate to form the compact layer. After the substrates cooled to around 70 – 80^{o}C TiO_2 paste (opaque, Dyenamo DN-GP-18OB) was applied on them using doctor blading method. The film was allowed to air dry for 2 h before sintering in the furnace at 125^{o}C for 5 min, 325^{o}C for 10 min, 425^{o}C for 15 min and 500^{o}C for 30 min. The heating rate was set to 5^{o}C/min. After natural cooling to 70 – 80^{o}C the photoanodes were placed in a vessel with 50mM solution of $InCl_3$ in 0.1M HCl and hold at 70^{o}C for certain time duration (30, 45 and 60 min). Then the films were rinsed with DI water and sintered at 450^{o}C for 30 min with heating rate 5^{o}C/min. The photoanodes cooled to 70-80^{o}C were placed in a 0.5 mM C264 triphenylamine dye solution in ethanol for 8 h to form dye monolayer over the film and then rinsed with pure ethanol, dried with N_2 and assembled into solar cell for further characterization.

3.1.4 Characterization of the photoanodes

The photoanodes were analyzed by High-Resolution X-ray Diffractometer (HR-XRD, PANalytical Empyrean) and Raman Spectroscopy (The Horiba LabRam Evolution) using 633 nm laser beam. The electron microscopic images of the photoanodes were obtained using Ultra-High-Resolution Field Emission Scanning Electron Microscopy (UHR FE-SEM, Hitachi SU8220) operated at 3.0 kV and Transmission Electron Microscope (Jeol JEM-1400 Plus) with 120 kV accelerating voltage. The dopant content in the films were analyzed with Energy-Dispersive X-ray spectroscopy (EDX) analysis performed on Hitachi TM 3030 with microanalysis system Bruker XFlash MIN SVE at 15 kV.

3.1.5 Fabrication of dye-sensitized solar cell

On the dye loaded photoanode few drops of the MPN-based DSSC electrolyte S104 (Dyenamo DN-OD05) were dropped using Pasteur pipette and the Pt counter electrode was placed on top. The electrodes were put together using a thin spacer tape. The cell area is 0.28 cm^2. The counter electrode was prepared

by doctor blading the paste of Pt (Dyenamo DN-EP01) on clean and dry FTO substrate followed by sintering in the oven at 500^{o}C for 30 min with heating rate 5^{o}C/min under air atmosphere.

3.1.6 Photovoltaic and electrochemical characterization of solar cells

The assembled cells were analyzed on Dyenamo Toolbox (DN-AE01, see Fig.3.2A) to obtain I-V characteristic curves and photovoltaic parameters (PCE, J_{SC}, V_{OC} and FF) at standard 100 mW/cm^2. At least three devices (replicates) were measured for each sample and the reported value is the average of all devices (replicates). The deviation from the mean value is calculated using the formula of standard deviation. The IPCE data of the cells were obtained from Dyenamo IPCE equipment (DN-AE03, see Fig.3.2B). The V_{OC} decay analysis and the charge extraction at open-circuit conditions were performed on the Toolbox. The electrochemical characteristics of the DSSCs were obtained using Electrical Impedance Spectroscopy technic on Autolab PGSTAT302N potentiostat/galvanostat (Metrohm) in the dark at –0.65 V forward bias, 10 mV amplitude and in a 10^{-1} – 10^{5} Hz frequency range. The working electrode of the EIS was connected to the photoanode of the solar cell and the counter / reference electrodes were connected to the Pt CE of the DSSC.

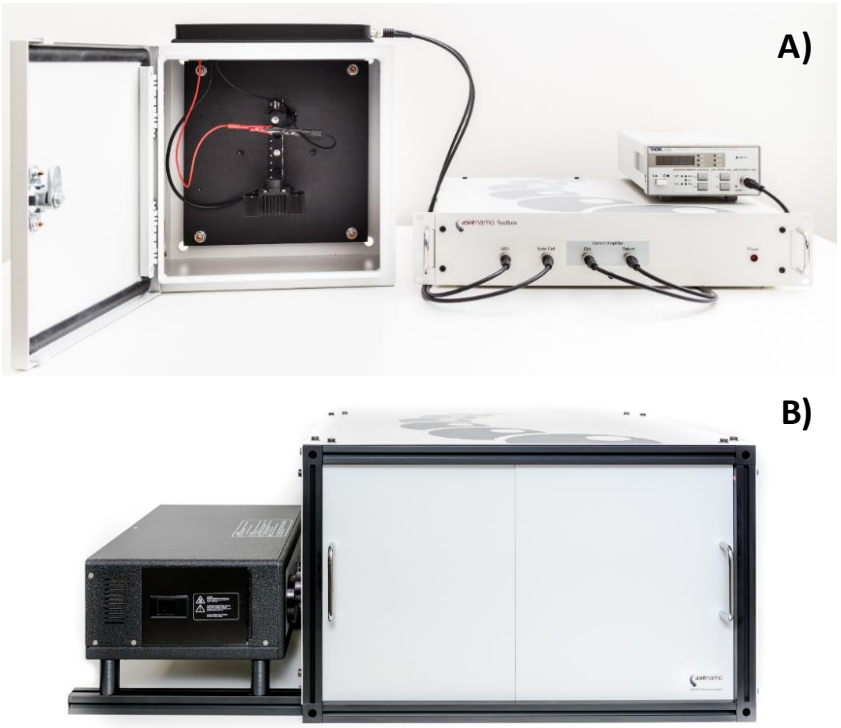

Figure 3. 2 A) DN-AE01 Dyenamo Toolbox and B) DN-AE03 IPCE test equipment

3.2 Control of porphyrin dye aggregation

3.2.1 Materials

All the materials (chemicals, solvents and gases) used in this work were purchased from commercial sources and used without further purification unless otherwise stated. The porphyrin dye ZnP was synthesized according to literature [211].

3.2.2 Fabrication of solar cells

A paste of 20 nm TiO_2 (CICC, PST-18NR) was doctor-bladed on a clean FTO glass electrode (Pilkington TEC-8 glass, with 6–9 Ohms/sq surface resistance and 2.3 mm thickness) and air-dried for 2 h before stepwise sintering at 325 ^oC for 5 min, at 375^oC for 5 min, at 450^oC for 15 min, and at 500^oC for 15 min. The scattering layer paste consisting of 400 nm anatase TiO_2 (CICC, PST-400 C) was doctor bladed onto the first transparent layer. The electrode was air-dried and then sintered in the same way as the first layer. The photoanode was post-treated with 40 mM aqueous $TiCl_4$ solution at 70^oC for 30 min and subsequently washed with water and ethanol. The electrode was then heated at 500^oC for 30 min. When cooling to 80^oC the photoanode was put into a ZnP dye solution in toluene with concentration 0.2 mM for 2 h. For dye – pyridine complex loading, the complexes were prepared before the soaking via mixing appropriate amounts of the sensitizer and ligand spacer solutions making sure that the final dye concentration is 0.2 mM. The mixtures were carefully mixed for 1h prior to soaking. The dye-loaded photoanodes were rinsed with ethanol. For the preparation of counter electrode, a small hole was drilled on FTO substrate and on cleaned FTO glass H_2PtCl_6 solution (2 mg Pt in 1 mL of ethanol) was spin-coated and followed by sintering at 400^oC for 15 min. The working and counter electrodes were put together with a thin Surlyn film in between the electrodes (SX 1170-25, 25 µm). To seal them the assembled cells were compressed at 110^oC. The electrolyte consisting of 0.6 M butylmethylimidazoliumiodide, 0.05 M I_2, 0.10 M LiI in 1:1 acetonitrile / valeronitrile solution was introduced via predrilled hole from the counter electrode side using vacuum. The holes were sealed with Surlyn and microscope cover slides to prevent electrolyte escape.

3.2.3 Dye loading

The amount of the dye loaded on TiO_2 was calculated using UV / Vis spectroscopy method. To calculate dye loading freshly sintered TiO_2 on FTO

were soaked in 0.2 mM toluene solutions of ZnP, ZnP/pyridine and ZnP/bipyridine for 2 hours and excess dye was removed by rinsing. The dye loaded TiO_2/FTO was placed in 5 mL of 0.1 M KOH in methanol overnight to desorb the dye. Dye concentrations in desorption solution were determined by UV / Vis absorption technic prior calibrated with ZnP, ZnP/pyridine and ZnP/bipyridine solutions in desorption solvent. From obtained values the amount of dye per unit area of the semiconductor was calculated.

3.2.4 Characterization

The photovoltaic parameters of the DSSCs were obtained under AM 1.5G irradiation with Oriel Sol 3A AAA Solar Simulator. A black mask was applied to the area surrounding the TiO_2 with an illuminated active area of 0.159 cm^2 for all measurements. Dye – pyridine complex optimized structures were calculated on Gaussian 16 [212] at B3LYP/6-31G (d) in vacuo without symmetry constraints and viewed using GaussView 6.0.16 software [213]. The UV / Vis absorption spectra of dye – pyridine complex solutions and dye-coated TiO_2 films were measured on Thermo Scientific Evolution 60S UV–Vis Spectrophotometer. Cyclic voltammetry analysis was performed on Elektric Zahner station, with FTO as working electrode, Pt wire as counter electrode and Ag/AgCl as reference electrode in 0.1 M solution of tetrabutylammonium hexafluorophosphate in DMF. The scanning rate was 0.25 V/s.

3.3 Cost-effective Pt-free counter electrodes

3.3.1 Pt-free counter electrode based on the composite of CoS and orange fiber derived carbon

3.3.1.1 Materials and synthesis

The materials (chemical reagents, solvents and gases) used in this section were bought from commercial suppliers and used without purification unless otherwise noted. Glass substrates with fluorine-doped SnO_2 (FTO) layer (DN-HB06, 15Ω/sq, 2.2 mm), anatase TiO_2 paste (DN-GP-18OB), Platinum paste (DN-EP01) and MPN-based DSSC iodide / triiodide electrolyte S104 (DN-OD05) were procured from Dyenamo AB, Sweden. The photoanode was coated with triphenylamine based sensitizer C264 with benzothiadiazole acceptor unit. The dye was prepared according to a procedure published elsewhere [210].

The Pt-free catalyst material was prepared from orange fiber and cobalt sulfide composite using solvothermal synthesis method (Fig.3.3). To synthesize the material a powder of orange fiber was prepared. To do so the juice was separated from orange flesh and the remnants were dried in an oven and pulverized to obtain powder. 1 g of the orange fiber powder, 0.25 g of elemental sulfur and 3.7 g of $Co(NO_3)_2 \times 6H_2O$ (calculated for 0.75 g of Co) were stirred in 50 mL ethanol for 2 h at room temperature. Then another 10 mL of ethanol was added and the mixture was placed in a Teflon liner, sealed with stainless-steel reactor and reacted at 200 °C for 12 h. After cooling, the mixture was filtered and the filter cake was washed with ethanol and dried at 80 °C overnight. Then the product was ground using mortar and pestle to obtain orange fiber derived carbon embedded cobalt sulfide OFC@Co_xS_y as a black powder. The as-prepared powder sample, labelled OFC@Co_xS_y-AP, was sintered in air at 200 °C and 300 °C for 30 min to fully oxidize the organic part to give OFC@Co_xS_y-200 and OFC@Co_xS_y-300 powders, respectively.

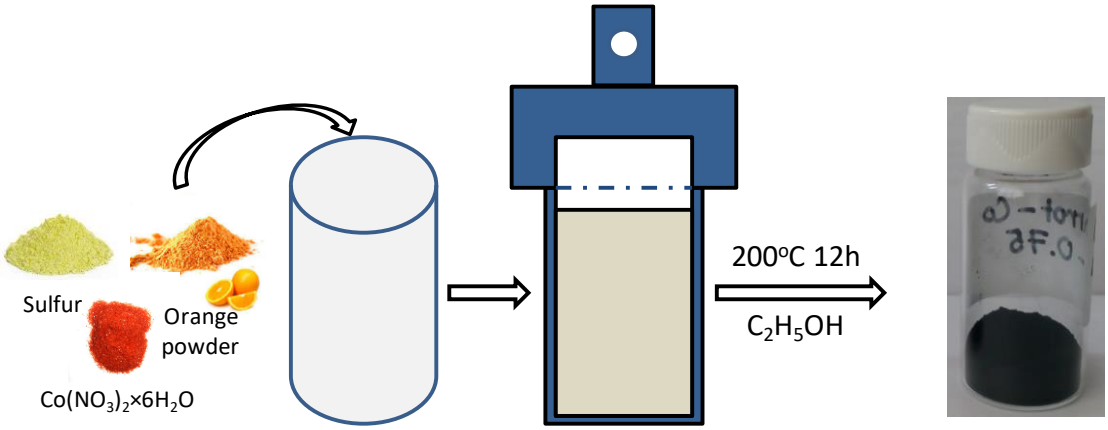

Figure 3. 3 Solvothermal synthesis of OFC@Co_xS_y

3.3.1.2 Characterization

The synthesized OFC@Co_xS_y-AP and sintered OFC@Co_xS_y-200, OFC@Co_xS_y-300 powders were characterized by Rigaku SmartLab® X-ray diffractometer (XRD) and Thermo Scientific, Nicolet™ iS5 FTIR Spectrometer. For FTIR analysis the powders were mixed with KBr in a mortar and tablets were obtained using press. TGA analysis of the samples was done using Q500 Thermogravimetric analyzer (TA Instruments). The electron microscopic images of OFC@Co_xS_y samples were obtained from Auriga Crossbeam 540 Scanning Electron Microscope (Carl Zeiss) and JSM-7500 Field Emission Scanning Electron Microscope (Jeol Ltd.). The elemental composition analysis was

obtained using Energy-Dispersive X-ray spectroscopy EDSX-max 150 (Oxford Instruments) and Perkin Elmer 2400 Series II CHNS/Owas. N_2 adsorption-desorption analysis was done on Nitrogen Porosimeter (Quantachrome Instruments). X-ray photoelectron spectroscopy (XPS) was performed in an Omicron Multi Probe XPS using a monochromised Al Kα source (XM 1000, 1486.7 eV). The instruments base pressure was 5×10^{-11} mbar and the instrumental resolution was set at 0.6 eV.

3.3.1.3 Solar cell fabrication

The working electrode was prepared as following. A compact TiO_2 layer was formed on clean and dry FTO glass substrate by placing the substrate in 50 mM $TiCl_4$ at 70 °C for 30 min then washed with ethanol, drying with N_2 gas and sintering at 500^{o}C for 30 min at 5^{o}C/min. 18–20 nm sized opaque TiO_2 paste was doctor bladed and air dried for 1 h before stepwise sintering in the furnace at 125 °C for 5 min, 325 °C for 10 min, 425 °C for 15 min, and 500 °C for 30 min. The photoanodes were then placed into 0.5 mM C264 dye solution in ethanol for 8 h in the dark condition. After indicated time the films were rinsed with ethanol and dried with N_2 gas.

The counter electrode was prepared as following. The paste of OFC@Co_xS_y-AP was doctor bladed on clean and dry FTO glass and sintered at 200^{o}C and 300^{o}C to obtain OFC@Co_xS_y-200 and OFC@Co_xS_y-300 counter electrodes, respectively. The paste was prepared by mixing 5 mg of OFC@Co_xS_y-AP in 400 µL of ethylene glycol : terpineol (10:1) mixture. Pt counter electrode was prepared by doctor blading the paste of Pt on FTO glass and sintering at 500 °C for 30 min with 5^{o}C/min.

Then the working and counter electrodes were sandwiched with thin spacer after applying the iodide / triiodide based electrolyte (Fig.3.4).

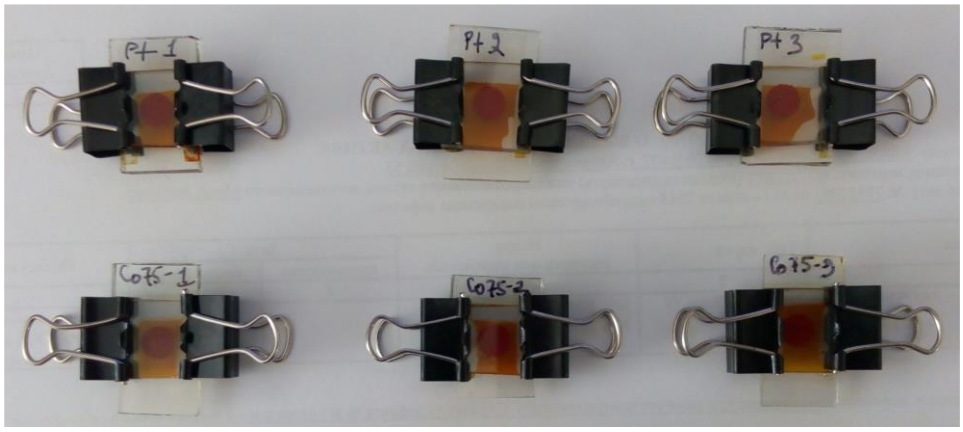

Figure 3. 4 Pictures of assembled dye-sensitized solar cells with Pt (top row) and OFC@CoxSy (bottom row) counter electrodes

3.3.1.4 Photovoltaic and electrochemical analysis

The electrochemical impedance spectroscopy (EIS) was carried out on electrochemical station IM6 of Zahner Elektrik under dark conditions at −0.72 V forward bias, 0.1–100 000 Hz frequency range and 10 mV amplitude and the obtained data were fitted using EIS Spectrum Analyzer [214]. The photovoltaic performances of the constructed cells were analyzed using the Dyenamo Toolbox (DN-AE01). At least three devices (replicates) were measured for each sample and the reported value is the average of all devices (replicates). The deviation from the mean value is calculated using the formula of standard deviation.

3.3.2 Pt-free counter electrodes based on Cu-Co-S ternary sulfides

3.3.2.1 Materials and synthesis

The consumables used in this section were bought from commercial suppliers and used as obtained unless otherwise stated. Chemical reagents used in the synthesis of counter electrodes, Ru-based N719 dye (CAS 207347-46-4) and opaque TiO_2 paste (Dyesol 18NR-AO) were procured from Sigma-Aldrich. Fluorine-doped SnO_2 (FTO) glass electrodes (with 2.2 mm thickness, 15 Ohm/sq surface resistivity), Pt paste (DN-EP01), and MPN-based DSSC electrolyte S104 (DN-OD05) were acquired from Dyenamo AB.

The synthesis of Cu-Co-S ternary sulfide counter electrodes was based on solvothermal method which implies the mixing of $CoCl_2{\times}6H_2O$, $CuCl_2{\times}2H_2O$, and thiourea in known amount in ethanol (60 mL) in a 100 mL Teflon lined stainless steel reactor (Fig.3.5). To grow the product on FTO, a clean FTO glass placed

against the wall of the liner and the mixture heated at 200°C for 4 h. Then the system naturally cooled before the FTO was rinsed with DI water, EtOH and dried in an oven at 90°C for 5 h.

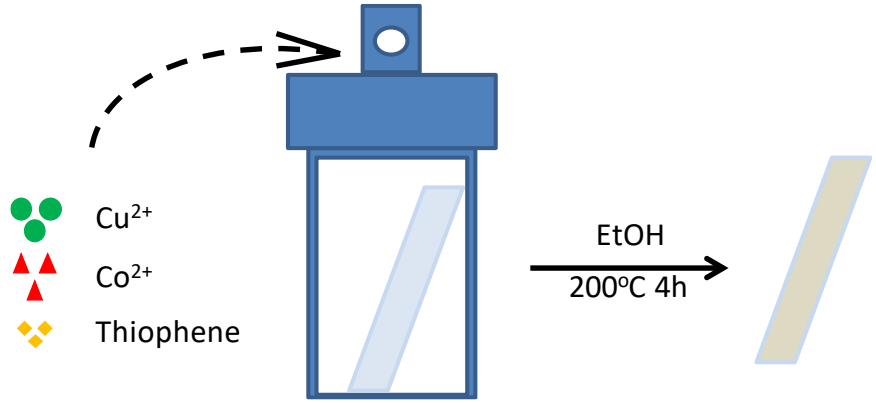

Figure 3. 5 Solvothermal growth of Cu-Co-S ternary sulfides on FTO glass electrode

3.3.2.2 Characterization

The obtained powder samples were analysed with Rigaku SmartLab® X-ray diffraction (XRD) and Horiba LabRam Evolution Raman Spectroscopy with 532 nm laser beam. Additionally, adsorption / desorption curves were obtained using N_2 porosimeter at 77.35 K with prior degassing the powders at 110°C for 8.5h. The electron microscopic top and cross sectional images of the counter electrodes were observed on scanning electron microscopy (SEM) (Auriga Crossbeam 540 Carl Zeiss) with Energy Dispersive X-Ray Spectroscopy (EDX).

3.3.2.3 Fabrication of solar cell

FTO glass was stepwise cleaned following procedure mentioned in this Methods section. For Pt CE, a Pt paste was doctor-bladed on clean and dry FTO glass substrate and sintered on a hot plate at 500°C for 30 min with slow stepwise increase of temperature from RT to 500°C. For Cu-Co-S CEs, they were used as prepared after rinsing and drying. For the working electrode (WE), N_2 dried FTO was placed in 40 mM $TiCl_4$ solution for 30 min at 70°C to form compact layer, then dried and TiO_2 paste was doctor-bladed. The film was air dried for 2 h before stepwise sintering as reported in previous subsections and N719 dye loading (0.285 mM in EtOH) for 22 h. Then, the dye loaded WE was sandwiched with CE with a thin spacer. The gap between electrodes was filled with MPN-based DSSC electrolyte S104.

3.3.2.4 Photovoltaic and electrochemical analysis

Photovoltaic measurements were carried out on the Dyenamo Toolbox (DN-AE01). At least three devices (replicates) were measured for each sample and the reported value is the average of all devices (replicates). The deviation from the mean value is calculated using the formula of standard deviation. The electrochemical analysis were done using IM6 Zahner Elektrik electrochemical station under dark condition with -0.65 V bias, 0.1 – 100000 Hz frequency range and 10 mV amplitude. The working electrode of the EIS was connected to the photoanode of the DSSCs and the counter / reference electrodes of the instrument were connected to the CE of the analyzed solar cells. The obtained data were fitted using EIS Spectrum Analyzer [214].

Chapter 4

4 Modification of TiO_2 photoanode through surface doping with indium

4.1 Introduction

The modification of DSSC photoanode through doping is valuable in terms of enhancing optical and electronic properties [215]. Indium has attracted great attention as a dopant for TiO_2 in recent years due to its high transparency, low toxicity and electronic properties that can be adjusted. In-doped TiO_2 has found application in different areas including ceramics [215-217], photocatalysis [218-219] and thin film [220]. The use of In-doped TiO_2 photoanode in DSSC was reported by Bakhshayesh and Farajisafiloo who claimed retarded electron recombination and decreased internal cell resistances as a result of doping [221]. The doping of TiO_2 was achieved by sol-gel method and the efficiency of cell with In-doped TiO_2 was improved by 17.4 %. This is despite the lower V_{OC} of In-doped TiO_2 cell compared to undoped TiO_2 caused by downward shift of conduction band [221]. Another use of In-doped TiO_2 photoanode prepared by sol-gel technic was reported by Beula and colleagues [222]. The authors observed a noticeable enhancement in cell photocurrent J_{SC} caused by high charge carrier mobility in In-doped TiO_2. Overall result was increase of PCE from 1.47 % to 2.71 % due to doping. Sun et al. utilized sol-gel synthesized In-doped TiO_2 as a compact layer between photoanode and TCO substrate [223]. They claimed 11.9 % improvement of PCE caused by slowed down charge recombination at TCO / TiO_2 interface and increased light harvest of dye.

All abovementioned reports apply sol-gel assisted method of preparation of doped TiO_2 which results in bulk doping. Bulk doping is a challenging technic as it requires strict control of the purity and concentration of reactants and conditions of synthesis which heavily affect the structure and size of product. Alternative method of improving the characteristics of photoanode is through surface-doping which is fast and cost-effective compared to bulk doping. Additionally, surface-doping is more attractive than bulk doping because the latter may generate extra deep traps that may inhibit electron diffusion [224]. This chapter describes the modification of TiO_2 photoanode of dye-sensitized solar cell with In surface-doping which is achieved by soaking TiO_2 film in In^{3+} acidic solution at 70^oC for 30-60 min.

4.2 Characterization

The films of pristine (In0) and indium doped TiO_2 at different soaking time (In30, In45 and In60) were analyzed by Scanning Electron Microscopy (SEM), Transmission Electron Microscopy (TEM) and Energy Dispersive X-Ray Spectroscopy (EDX) technics. SEM pictures revealed that untreated and post-treated films have particles of identical size, around 22 nm (Fig.4.1) indicating no 'extra' layer is formed. TEM observations of In30 sample confirm this (Fig.4.2). The calculated average d-spacing is 0.354 nm which corresponds to the dominant (101) plane of TiO_2 anatase (JCPDS 21-1272). Further analysis on EDX exhibited homogeneous distribution of indium over TiO_2 (Fig.4.3). Quantitative analysis indicates the increase of indium content with soaking time, see Fig.4.4. However, the weight percent of indium was less than 0.5 %. These findings suggest that post-treatment resulted in indium surface doped TiO_2 rather than forming layer over TiO_2 nanoparticles.

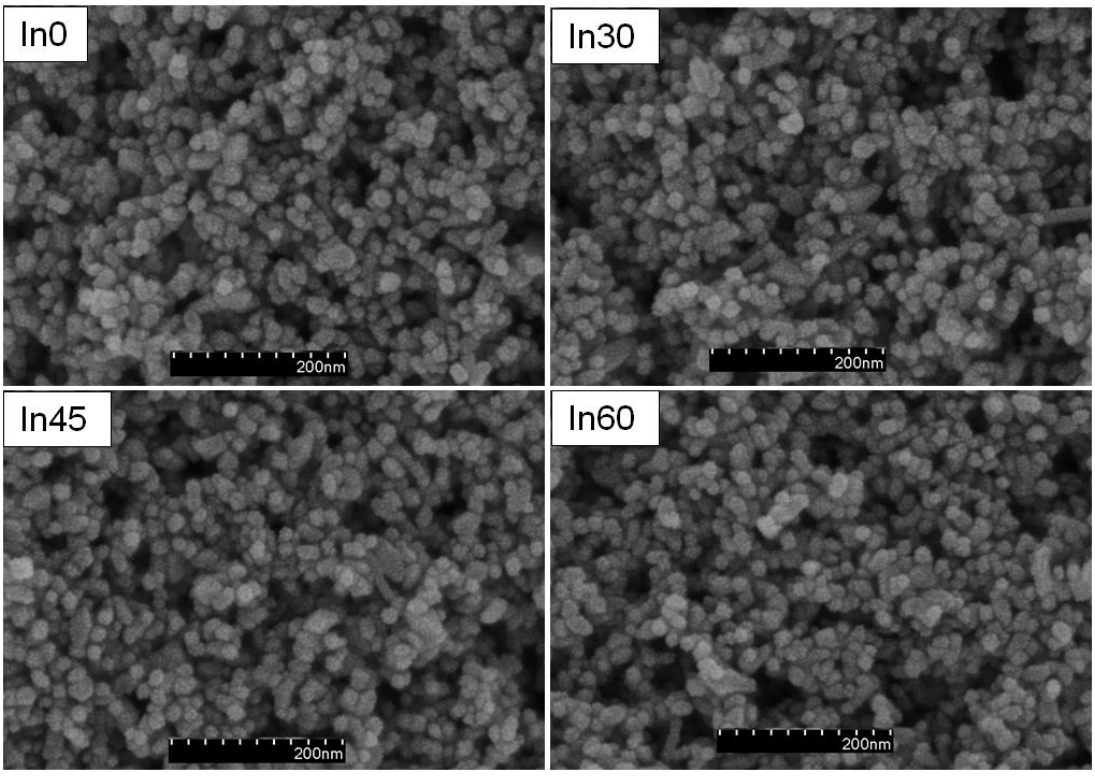

Figure 4. 1 SEM images of pristine and In surface doped TiO_2 films

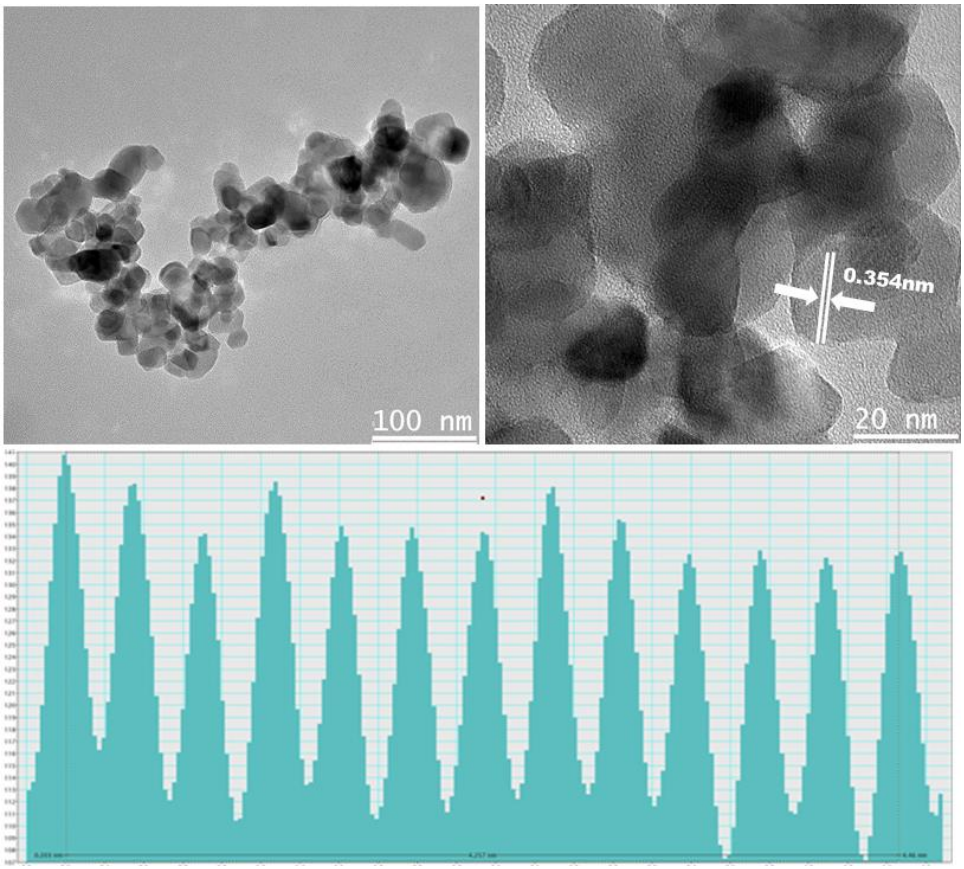

Figure 4. 2 TEM images of In30 sample with lattice spacing

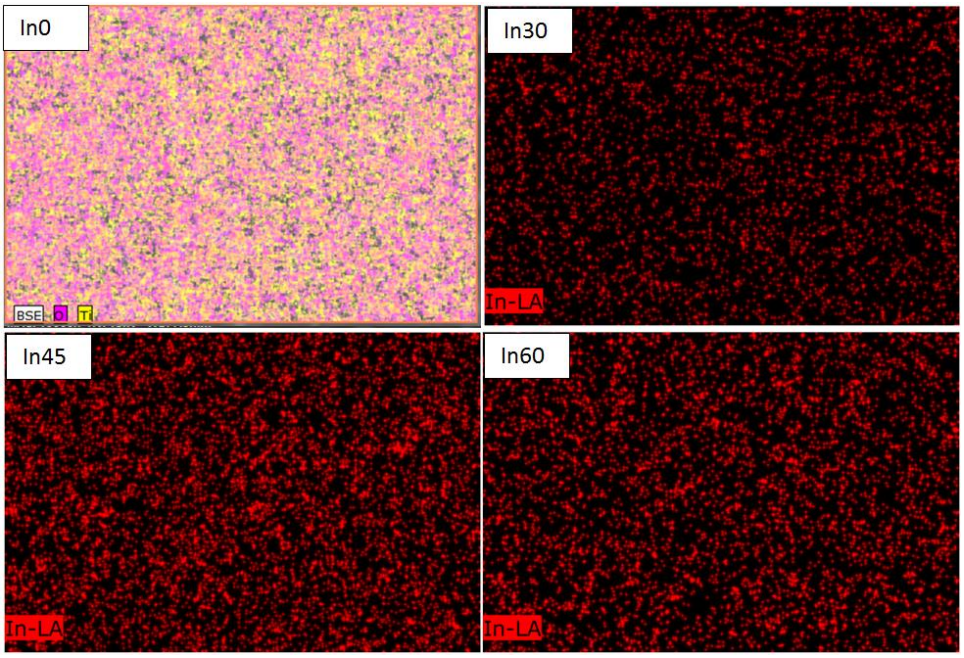

Figure 4. 3 EDX spectra of pristine and In surface doped TiO_2 films

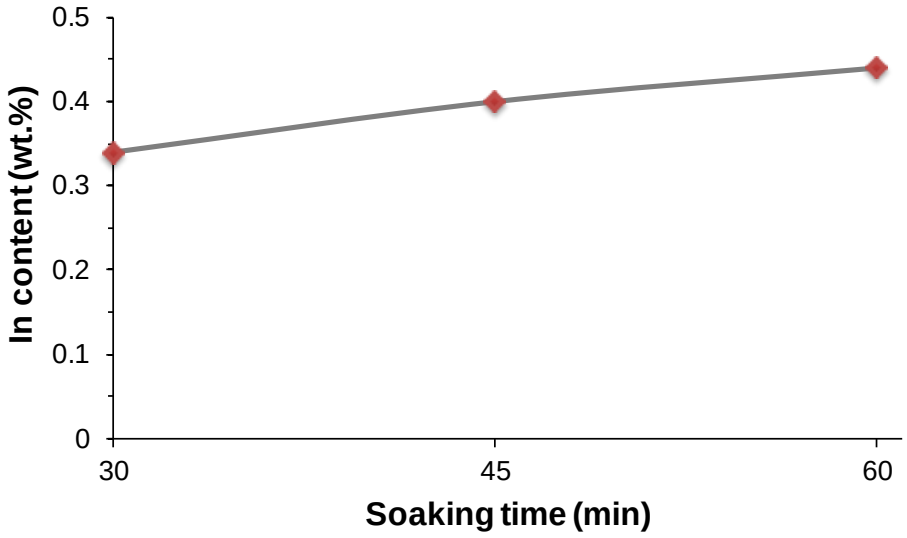

Figure 4. 4 In content of surface doped TiO_2 films

Moreover, the samples were studied with X-Ray Diffractometer (XRD) and Raman Spectroscopy. The analysis on XRD produced peaks at 25.3º, 37.8º, 48.0º, 53.9º, 55.0º, 62.5º, 62.7º, 68.8º, 70.3º, and 75.0º which are indicative of anatase titania with corresponding planes of (101), (004), (200), (105), (211), (213), (204), (116), (220) and (215), respectively (Fig.4.5).

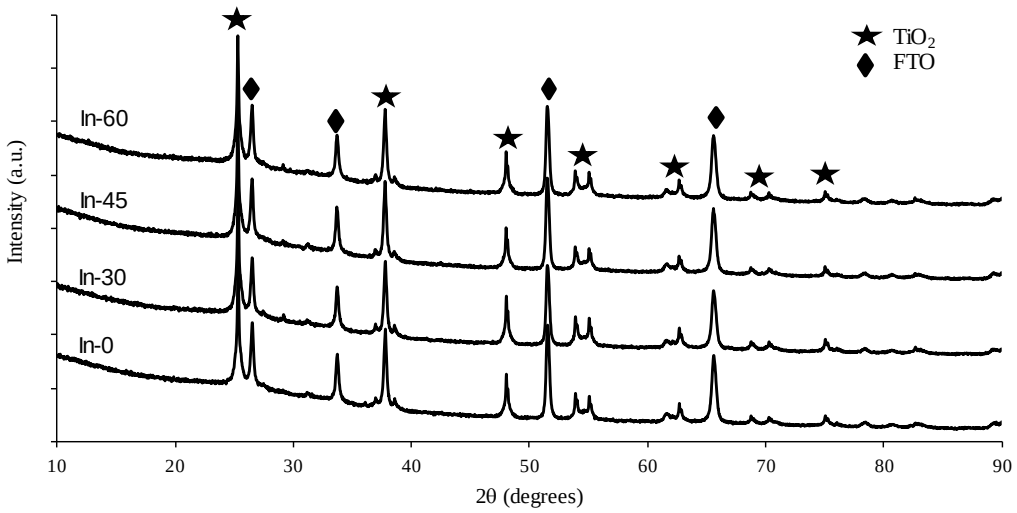

Figure 4. 5 XRD spectra of pristine and In surface doped TiO_2 films on FTO substrate [1]

Sharpened peaks are illustrative of high degree of crystallinity. The signals at 25.3º, 37.8º and 48.0º were analyzed by Scherrer equation (eq.4.1) to determine the size of the particles.

$$D = \frac{K\lambda}{\beta \cos\theta} \qquad (4.1)$$

D is the size of crystallite, the shape factor K = 0.9, β is full width of the peaks at half maximum and θ is diffraction angle. λ the wavelength of applied X-Ray, 0.1540598 nm. The results of the Scherrer analysis revealed crystallite sizes between 17.8 – 27.6 nm which correspond with the value manufacturer declared and in agreement with SEM findings. The study of the films by Raman Spectroscopy generated characteristic to TiO_2 peaks resulting from its six modes - 3Eg + 2B1g + A1g (Fig.4.6).

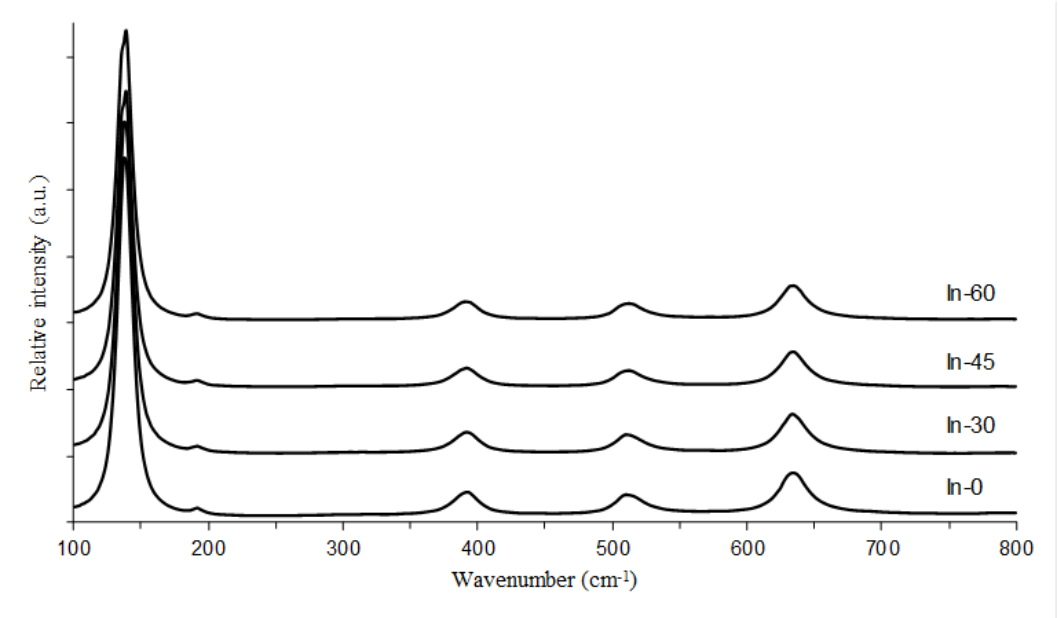

Figure 4. 6 Raman spectra of pristine and In surface doped TiO_2 films [1]

Peak observation revealed noticeable broadening and splitting of the signals from surface doped samples. This phenomenon is more obvious at E_g mode (Fig.4.7) and is caused by disorder due to the presence of indium dopant [225]. The surface atoms of bare TiO_2 are weakly bound because of the absence of neighboring atoms. Introduction of indium dopant changes this leading to higher vibrational wavenumbers as was observed with post-treated samples.

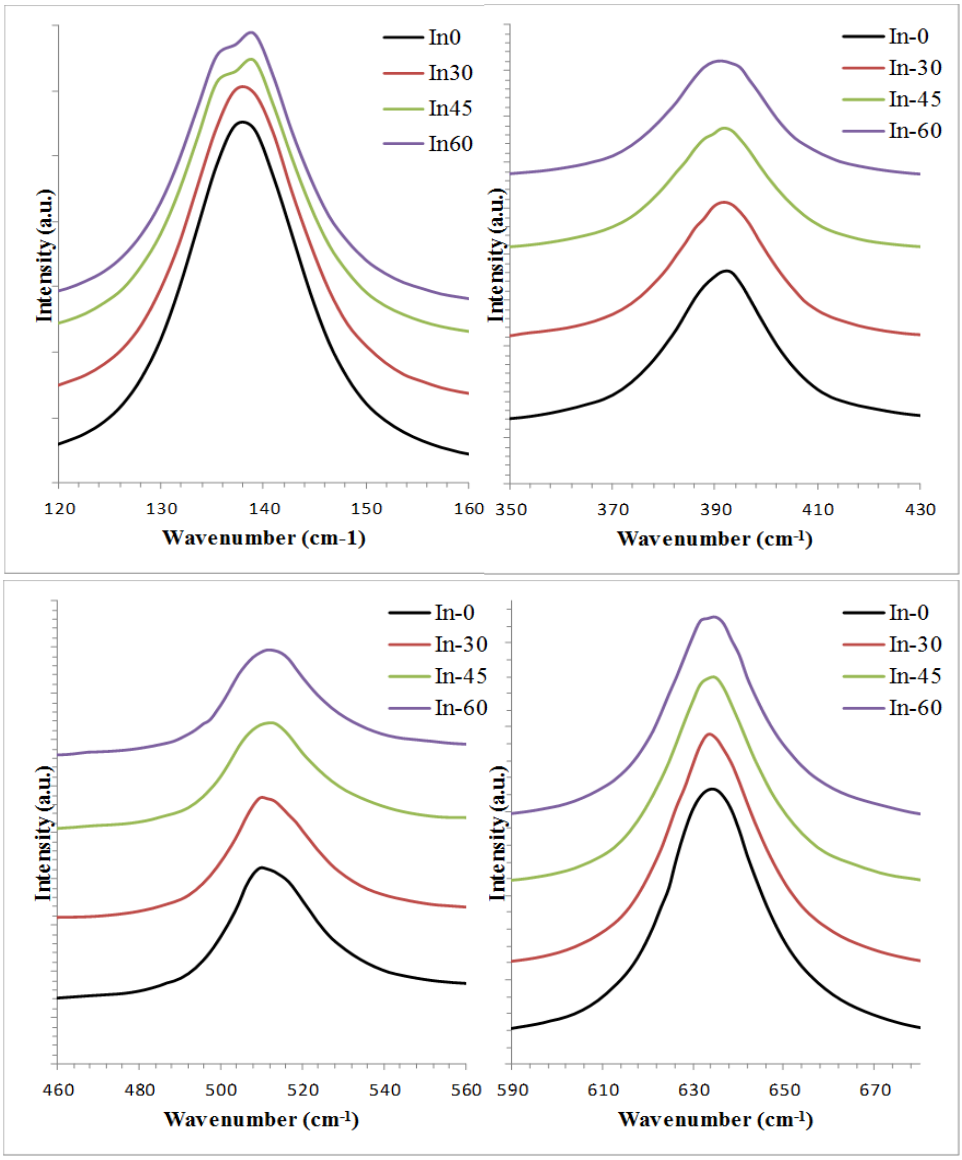

Figure 4. 7 Broadening and splitting of Raman spectra after surface doping with indium

4.3 Photovoltaic performance

The I-V curve and photovoltaic parameters of DSSCs assembled from doped and undoped TiO_2 are shown in Fig.4.8 and Table 4.1. The results demonstrate increase in the photovoltage for doped cells In30 and In45 compared to pristine In0. It was found that V_{OC} decreased with the increase of In content: V_{OC}(In30) > V_{OC}(In45) > V_{OC}(In60). Similar trend can be observed for J_{SC} of doped cells: J_{SC}(In30) > J_{SC}(In45) > J_{SC}(In60). Among doped cells only In30 generated higher short-circuit current than undoped In0 cell. Notably, surface doping of TiO_2 photoanode with indium resulted in significant increase of fill factor for all cells compared to undoped solar cell. Thus, surface doped In30 cell outperformed reference In0 cell by 18 % in terms of power converting efficiency due to

improvement of V_{OC}, J_{SC} and FF. In45 cell also demonstrated higher efficiency than In0 with 6.39 % PCE against 6.09 % of the latter.

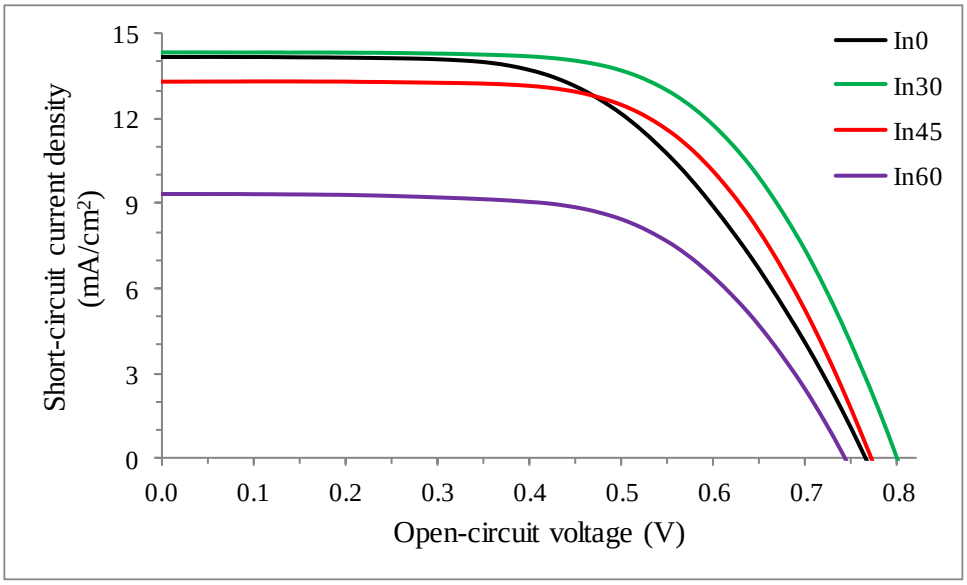

Figure 4. 8 I-V characterization of cells [1]

Table 4. 1 Photovoltaic parameters of pristine and surface doped TiO_2 sensitized solar cells [1]

Cells	Eff (%)	Voc (V)	Jsc (mA/cm²)	FF
In0	6.09±0.23	0.77±0.01	14.17±0.82	0.56±0.00
In30	7.19±0.14	0.80±0.02	14.33±0.83	0.63±0.01
In45	6.39±0.48	0.78±0.02	13.30±0.64	0.62±0.03
In60	4.30±0.08	0.75±0.03	9.33±0.91	0.62±0.02

Incident photon-to-current conversion (IPCE) analysis of the solar cells was performed to study the effect of doping on J_{SC} (Fig.4.9). The results were found consistent with J_{SC} order. In general, longer soaking time (In45 and In60) caused lower IPCE than pristine cell, whereas post-treatment for 30 min led to higher IPCE for In30 compared to In0. The analysis of photovoltage as the function of photo-induced charge density (V_{OC} ~ f(Q)) may further shed light on understanding the effect of post-treatment on J_{SC}.

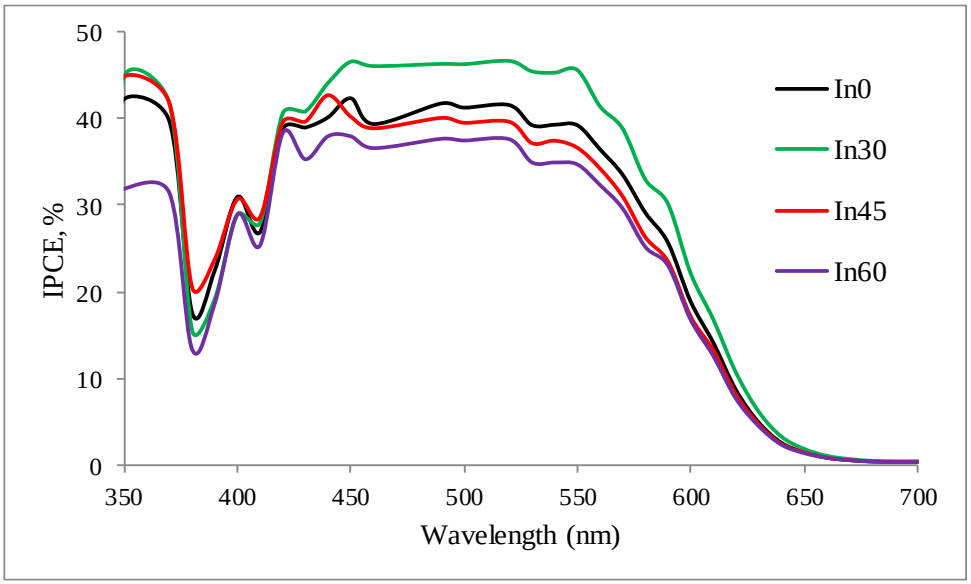

Figure 4. 9 IPCE characterization of solar cells [1]

The results can be seen in Fig.4.10 and present linear dependence of V_{OC} on charge density with $R^2 > 0.999$. The position of a line relative to a reference line may indicate the movement of conduction band and a line is positioned lower relative to a reference implies downward movement of the conduction band and vice versa [226]. As the result of the analysis show, In surface-doping caused downward movement of TiO_2 conduction band and the shift is greater with the increase of soaking time: $CB_{In-0} > CB_{In-30} > CB_{In-45} \approx CB_{In-60}$. More specifically, compared to In0, band edge moved to 50 mV for In30 and to 120 mV for In45 and In60. This indicates increased electron injection energy ΔG_{inj} for doped cells; therefore, In30 cell generated higher J_{SC} compared to In0. However, it did not lead to the increase of J_{SC} for In45 and In60. Hence, this may indicate that excess surface doping may create a 'thick' doped layer which hinders charge transport possibly by trapping electrons.

The movement of TiO_2 band edge, on the other hand, is not consistent with V_{OC} values since downward movement should lower voltage because V_{OC} is the difference between TiO_2 conduction band and redox potential of electrolyte. This suggests that the reason for higher photovoltage is decreased recombination due to surface doping. To understand this, V_{OC} decay analysis was carried out.

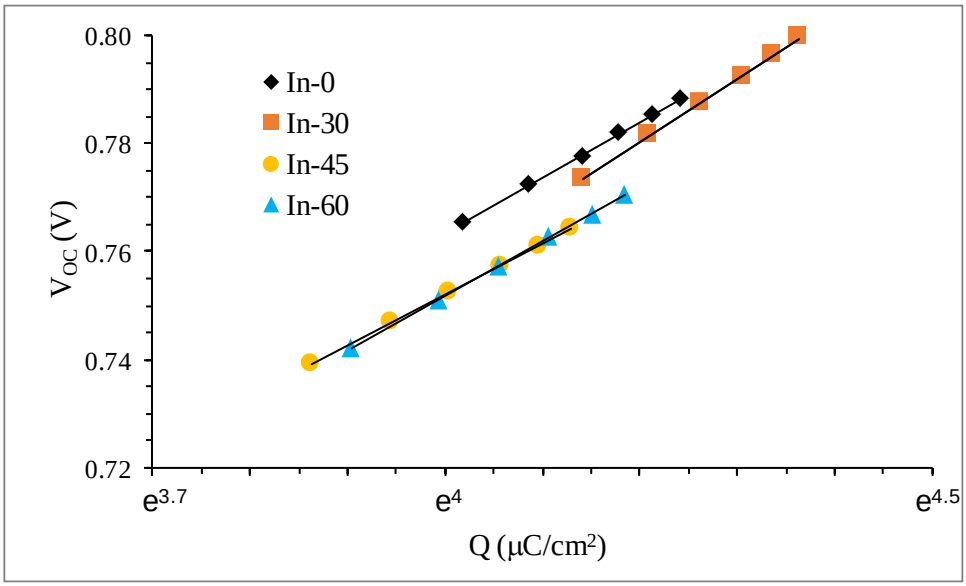

Figure 4. 10 Open-circuit photovoltage as a function of charge density [1]

The decay of open-circuit voltage is measured by exposing a cell to light source under open-circuit condition. This allows buildup of electrons in the conduction band of the photoanode and creates voltage. At certain time the voltage is stabilized and then the light is turned off and the decay of V_{OC} is measured with respect to time. The decay of V_{OC} proceeds with electrons escaping TiO_2 conduction band via recombining with electrolyte species or oxidized dye molecules. The path via oxidized dyes is less probable because the measurement was carried out in the dark; hence, no dye is oxidized. Recombination via back contact is also eliminated due to the presence of compact TiO_2 layer which is known to significantly block the escape of electrons from FTO into the redox electrolyte [64, 227]. Moreover, open-circuit condition does not allow charge collection at TCO. Nevertheless, to avoid potential loss of electrons through back contact a limit of minimal voltage was set to 0.4 V, as it is known that the role of recombination at back contact may increase at lower voltages [228]. Therefore, the main possible path for the electron back flow is through recombination with electrolyte. Prior to measurements the DSSCs were cooled in refrigerator at 0^oC to minimize the rate of recombination. The results of the analysis showed that V_{OC} decay is significantly slower in surface doped samples compared to undoped cell (Fig.4.11). The order of V_{OC} decay from the slowest to the fastest is as following: In30 < In45 < In60 < In0. This suggests that the rate of recombination is much slower in surface doped cells indicating positive effect of In impurities.

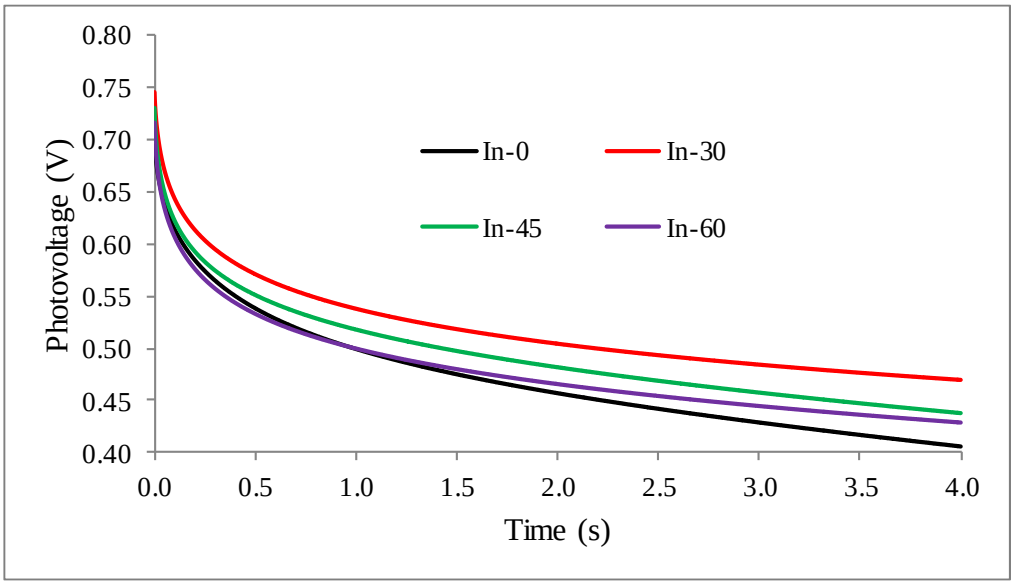

Figure 4. 11 Open-circuit photovoltage decay curves [1]

The data from V_{OC} decay can be used to derive electron lifetime (τ_e) using following equation [229]:

$$\tau_e = \frac{k_B T}{q} \left(\frac{dV}{dt}\right)^{-1} \tag{4.2}$$

where kB is Boltzmann constant, T is absolute temperature, q is elementary charge, V is voltage and t is time. The calculated lifetime is considered as the effective lifetime of conduction band electrons [230] and presented in Fig.4.12. The comparison of derived data clearly demonstrate that the lifetime of electrons injected into surface doped TiO_2 is higher than in pristine TiO_2 and less susceptible to recombination. Bisquert et al. report three possible mechanisms of electron recombination with electrolyte: 1) direct transfer from conduction band states, 2) indirect transfer of deep monoenergetic surface state trapped electrons and 3) indirect transfer of electrons trapped at an exponential distribution of band gap surface states near conduction band [231]. Considering that electron diffusion in nanoporous TiO_2 photoanode proceeds through trapping – detrapping model [232] and that the surface trap states constitute greater portion of all trap states in large surface area materials like mesoporous TiO_2 [233-234]; we assume that recombination of electrons mostly happens through surface trap states. Therefore, the introduction of indium impurities into the surface of TiO_2 passivates and diminishes the surface trap states minimizing charge recombination centers. However, with the increased content of In the V_{OC} decreases due to recombination through induced by the dopant trap states [235].

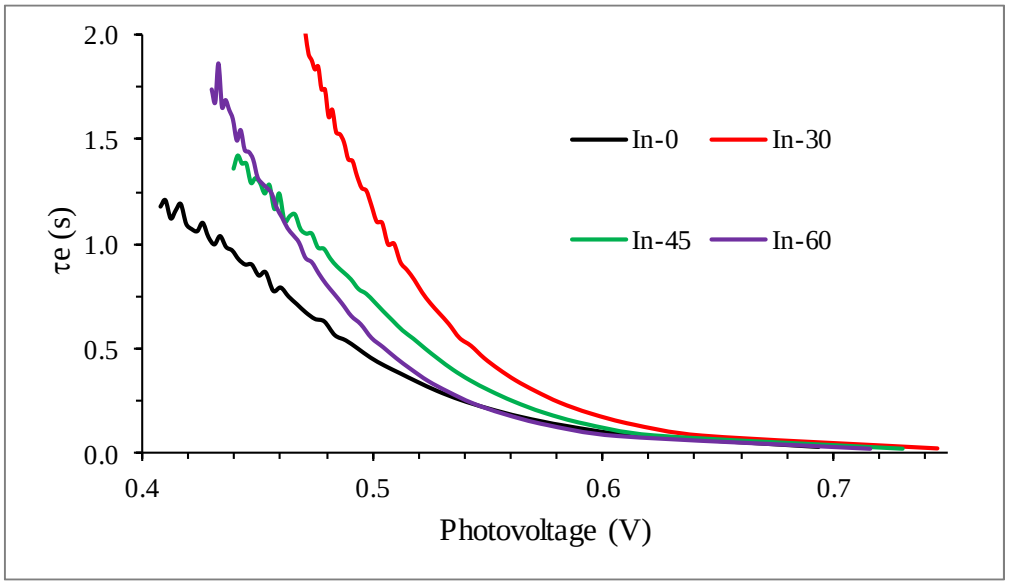

Figure 4. 12 Electron lifetime curves of solar cells [1]

4.4 Electrochemical performance

The effect of In surface-doping on recombination was further verified by the analysis of the DSSCs on Electrical Impedance Spectroscopy (EIS). EIS is a three electrode system and its working electrode was connected to the photoanode of the solar cell, whereas the counter and reference electrodes were connected to the Pt counter electrode of DSSC. The cells were scanned with -0.65 V forward bias, 10 mA amplitude at 0.1 – 100 000 Hz frequency range in the dark to obtain their Nyquist plots (Fig.4.13). The data were fitted using equivalent circuit, presented in Fig.4.13 as inset and consisting of series resistance R_S, charge transfer resistances at Pt counter electrode / electrolyte interface (R_1) and TiO_2 / dye / electrolyte interface (R_{CT}) and constant phase element CPE. The results clearly demonstrate the passivating effect of the indium dopant by reducing surface trap states which act as recombination centers. The R_{CT} can be considered as recombination resistances and for the surface doped cells it is noticeably greater than in reference undoped cell (Table 4.2). The recombination resistance R_{CT} was improved 2.5 times for In30 (732.9 Ω) with respect to In0 (297.9 Ω) and it decreases with increased dopant content almost reaching its original value in In60 cell (326.4 Ω). The order of R_{CT} is consistent with the V_{OC} of doped cells. Therefore, we can conclude that In surface doping of TiO_2 shifts the conduction band edge downward and passivates surface trap states reducing charge recombination. The increase in V_{OC} (for In30 and In45) is combined result of the two effects. For In60 cell, its

V_{OC} is lower compared to In0 cell because the passivation effect is minimized due to newly added trap states by the dopant.

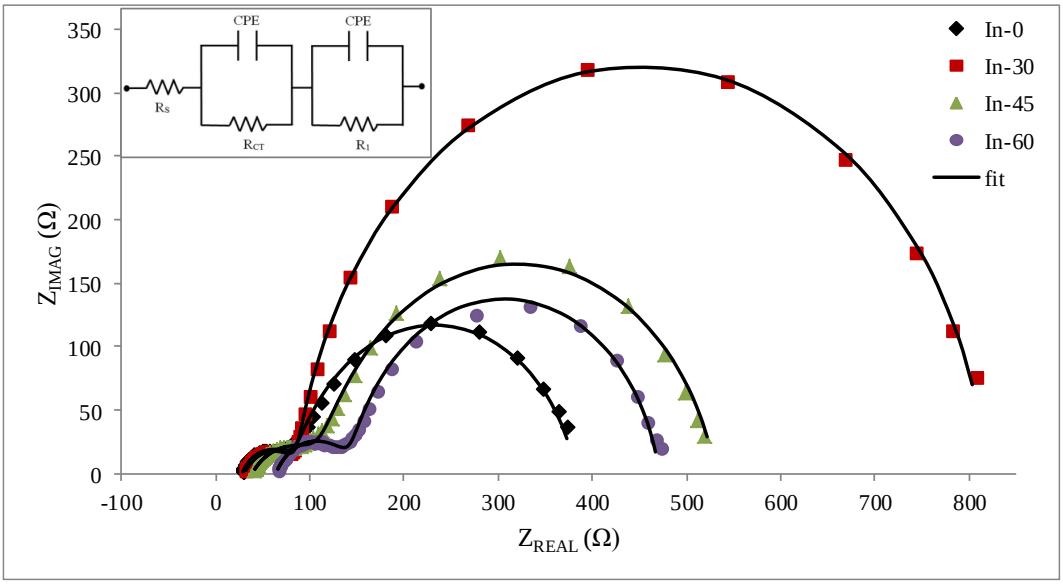

Figure 4. 13 Nyquist plots of dye-sensitized solar cells. Inset is equivalent electrical circuit used for fitting [1]

Table 4. 2 Electrochemical parameters of In0 – In30 cells [1]

Cell	$R_S(\Omega)$	$R_1(\Omega)$	$R_{CT}(\Omega)$
In0	28	56.7	297.9
In30	30.4	56.7	732.9
In45	38.6	76.4	416.3
In60	63.8	80.7	326.4

4.5 Stability of the cell

The stability of cells, In0 and In30, were studied over the duration of 300 h. The DSSCs were kept at ambient conditions and their PCE was measured periodically. The stability graph is shown in Fig.4.14. The performance of the cells over the test period was found quite stable except some devices exhibiting lower efficiency (85-90 %) than the original value due to the leaking of liquid electrolyte. In general, indium surface doped cell In30 demonstrated comparable result with In0. After 300 hours of test In30 kept 99.4 % of its original PCE, whereas the PCE of the reference cell In0 decreased to 95.3 %.

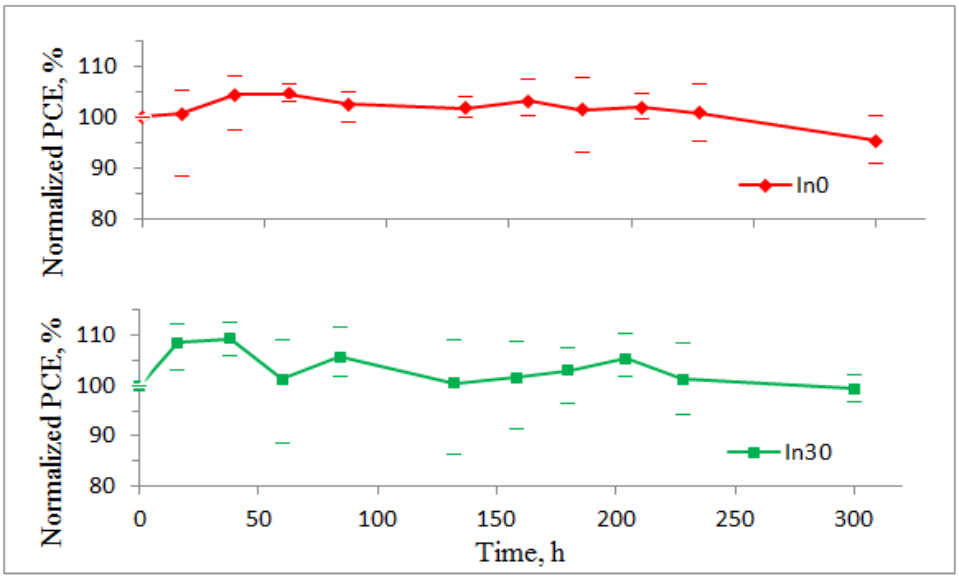

Figure 4. 14 Stability of the efficiency of In0 and In30 [1]

4.6 Summary of the chapter

In this chapter indium surface-doped TiO_2 photoanode for dye-sensitized solar cells was prepared by a simple procedure of soaking the mesoporous oxide film in In^{3+} acidic solution at 70°C followed by sintering at 450°C. The incorporation of indium was confirmed by several instrumental technics as SEM, TEM, EDX, XRD and Raman Spectroscopy. The effect of soaking step duration on photovoltaic and electrochemical behavior of the photoanode was investigated. The results demonstrated that In surface-doping caused downward movement of TiO_2 conduction band and slow down of charge recombination. The net outcome of these two effects is a significant increase in the cell photovoltage. The photocurrent, on the other hand, was not affected at lower soaking time; however, increasing soaking time led to drop in J_{SC} for surface-doped cells compared to undoped cell. The possible reason for retarded recombination is reduction of the number of surface trap states caused by indium passivation. High degree of surface doping (longer soaking time) generates extra surface traps by the dopant which can act as recombination center.

Overall, similar to bulk doping reported earlier [221-222], In surface-doping of TiO_2 led to downward movement of conduction band, decrease of recombination. However, the main difference is a remarkable improvement of cell photovoltage and fill factor without altering the photocurrent. Thus, compared to undoped TiO_2 cell, In surface-doped TiO_2 cell demonstrated 18 % increase in

cell efficiency. This shows surface-doping could be as efficient as bulk doping as a method of DSSC photoanode modification but at lower cost.

Chapter 5

5 Control of porphyrin dye aggregation by axial coordination with pyridine-based ligands

5.1 Introduction

Porphyrin dyes are one of the best performing sensitizers by virtue of their wide (400 – 700 nm) light absorption characteristics. However, their planar structure makes them prone to aggregate on the surface of semiconductor. Controlling porphyrin dye aggregation is critical in generating high efficiency. Hence, the highly efficient SM315 porphyrin sensitizer has four oxyoctyl units which wrap the dye preventing it from π-π stacking [45]. This complicates the synthesis and adds to the cost of the dye. To cut down the expense and facilitate easy preparation we propose a self-assembly approach which is based on axial coordination of metalloporphyrin dyes with a ligand. The coordination of the central metal of metalloporphyrin with Lewis base nitrogen through D-A bonding has been known for long [236]. The positive effect of the interactions of this nature is also observed when Lewis base solvent is applied for dye loading accounting for 17 % improvement of cell PCE compared to non-coordinating solvent [211]. The utilization of axially-coordinated porphyrins in DSSCs has been reported [237-240]. All of them use umbrella-type configuration where porphyrin is light absorbing moiety, whereas the axially-coordinated ligand acts as dye anchoring unit. However, their PCE is very low due to weak charge transfer from porphyrin to the ligand. In this chapter we use axially-coordinated pyridine-based ligands to suppress porphyrin dye aggregation.

5.2 Axial coordination of porphyrin dye with pyridine-based ligands

To investigate the effect of axial coordination on porphyrin dye performance we used ZnP dye (cyano-3-(2′-5′,10′,15′,20′-tetraphenylporphyrinatozinc(II)yl) acrylic acid) and 4-methylpyridine (Py) and 4,4’-bipyridine (biPy) as Lewis base ligands (Fig.5.1).

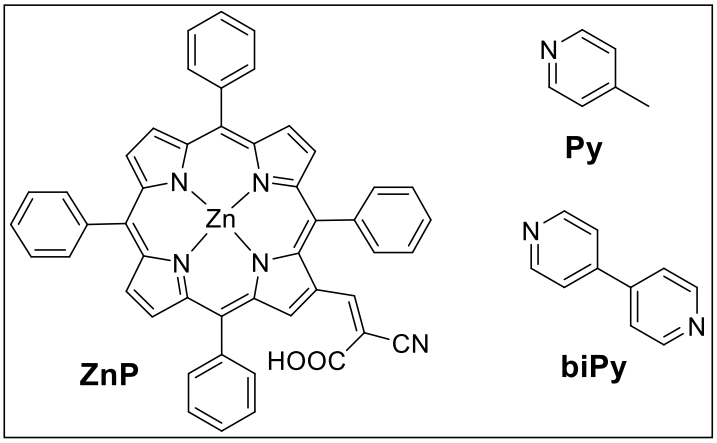

Figure 5. 1 Structures of porphyrin dye and N-bearing ligands

ZnP-Py and ZnP-biPy complexes were analyzed with density functional theory (DFT) calculations. The illustration of the complex structures can be seen in Fig.5.2. The adsorption energies E_{ads} of the complexes were calculated based on supermolecular method following the next equation 5.1:

$$E_{ads} = E_{complex} - (E_{ZnP} - n \times E_{Ligand}) \quad (5.1)$$

$E_{complex}$ stands for the energy of ZnP-Py or ZnP-biPy complex, E_{ZnP} and E_{Ligand} are the energies of detached molecules. The adsorption eneries for penta- and hexacoordinated ZnP-Py complexes are – 14.6 kcal/mol and – 16.1 kcal/mol, respectively, whereas for ZnP-biPy complex E_{ads} = - 27.5 kcal/mol [2]. The analysis revealed that ZnP-biPy complex is thermodynamically stable compared to both 4-methylpyridine complexes. The calculations also reavel the distance between the complexes: 6.06 Å and 12.84 Å for penta- and hexacoordinated ZnP-Py complexes, respectively, and 11.50 Å for ZnP-biPy complex [2]. The distance between two bipyridine complexes is similar to the gap between oxygen atoms of a ruthenium based N3 sensitizer and suitable for the attachment over semiconductor [241]. The distance between hexacoordinated ZnP-Py complexes is large resulting in lower dye uptake and uncovered surface areas easily accessible for electrolyte species which may lead to increased back electron transfer.

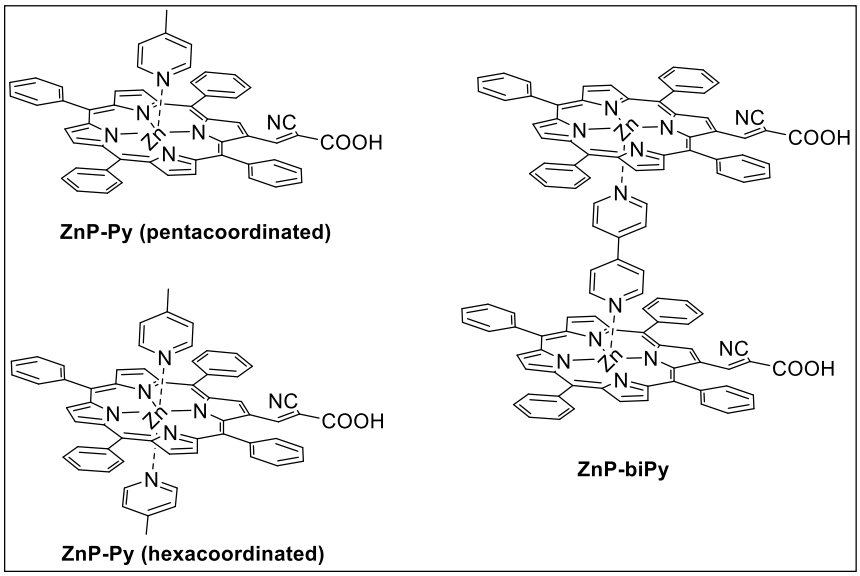

Figure 5. 2 Illustration of pentacoordinated and hexacoordinated ZnP–Py and ZnP–biPy complexes

5.3 Photovoltaic performance of axially-coordinated porphyrin complexes

The results of the photovoltaic performance of porphyrin complexes are presented in Table 5.1. The obtained values are compared with the photovoltaic parameters of a cell with ZnP dye [211]. The utilization of ZnP complexes with pyridines results in significant increase of photovoltage for all dye:ligand configurations (1:0.5, 1:1 and 1:2) indicating the positive effect of complexation. ZnP-biPy 1:0.5 complex generated the highest cell efficiency 5.23 %. Notably, the DSSC with this complex was found the only cell producing higher J_{SC} than the original ZnP cell. Among ZnP-Py cells the one with ZnP-Py 1:1 ratio was found the best producing 4.63 % efficiency. The hexacoordinated ZnP-Py (1:2) complex demonstrated lower PCE of 4.36 %. This result supports our findings in theoretical calculation where the formation of hexacoordinated ZnP-Py complex makes the semiconductor susceptible to recombination and photovoltaic measurements revealed lower V_{OC} for ZnP-Py cell.

Table 5. 1 Photovoltaic parameters of cells with ZnP dye and ZnP-Py or ZnP-biPy complexes [2]

Mole ratio				V_{OC} (mV)	J_{SC} (mA cm^{-2})	FF (%)	PCE (%)
a)	ZnP			424[a]	13.6[a]	62.7[a]	3.62[a]
b)	ZnP	:	Py				
	1	:	0.5	510	11.2	68.6	3.93
	1	:	1	540	12.4	68.9	4.63
	1	:	2	530	12.1	68.3	4.36
c)	ZnP	:	biPy				
	1	:	0.5	556	13.9	68.0	5.23
	1	:	1	561	13.2	67.6	5.00
	1	:	2	550	12.9	67.5	4.78

[a] Data from reference [211].

To assess the effect of complexation on dye uptake, the amount of TiO_2 loaded dyes were calculated. To do so freshly sintered TiO_2 on FTO were soaked in 0.2 mM toluene solutions of ZnP, ZnP-Py and ZnP-biPy for 2 hours and excess dye was removed by rinsing. The dye loaded TiO_2/FTO were placed in 5 mL of 0.1 M KOH in methanol overnight to desorb the dye. Dye concentrations in desorption solution were determined by UV/Vis absorption spectroscopy prior calibrated with ZnP, ZnP-Py and ZnP-biPy solutions in desorption solvent (Appendices A Fig.A.1 – A.7). From obtained values the amount of dye per unit area of the semiconductor was calculated (Table 5.2). The results suggest that complexation with pyridines decrease the amount of ZnP dye indicating the positive effect of complexation in reducing dye aggregation. To clarify this further we obtained the UV-Vis absorption spectra of ZnP, ZnP-Py and ZnP-biPy in solution and in TiO_2 film. Since broadening of the spectrum is indication of aggregation, the absorption spectra in solution and in film were superimposed to compare (Fig.5.4). It can be clearly observed that the complexation with bipyridine (ZnP-biPy) remarkably reduces the dye agglomeration compared to ZnP-Py complexation and led to higher J_{SC} and V_{OC} compared to ZnP cell. The poor efficiency of ZnP-Py in suppressing dye aggregation is explained by possible desorption of 4-methylpyridine ligand. Since the coordination of 4-methylpyridine with ZnP is thermodynamically less stable, some of the pyridines may adsorb on semiconductor surface and, thus, induce band-edge movement. In DSSCs, the addition of pyridines is known to lower J_{SC} but increase V_{OC} [40, 242]. This is ascribed to the effect of pyridines shifting band-edge of TiO_2 in negative direction [139-140]. Therefore, V_{OC} in ZnP-Py cells were higher than in

ZnP. Additionally, the lowered electron injection energy and aggregation of dyes led to observed lower J_{SC} in ZnP-Py complexes compared to ZnP cell.

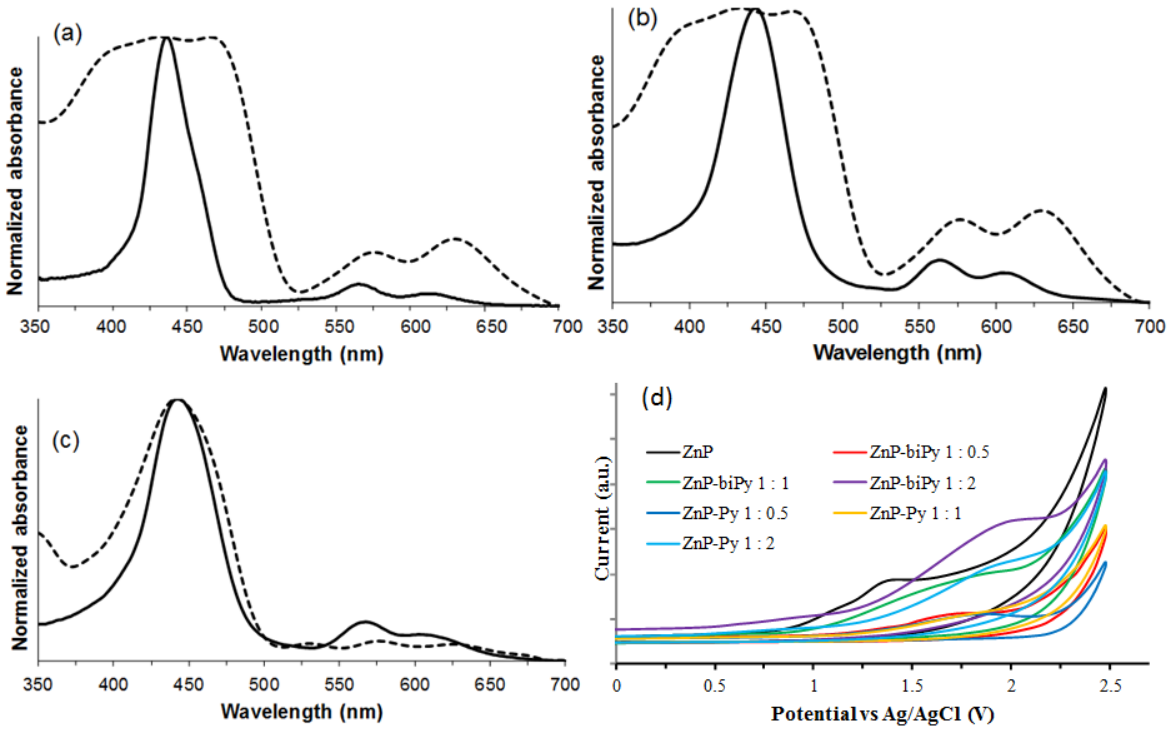

Figure 5. 3 Absorption spectra of (a) ZnP, (b) ZnP-Py and (c) ZnP-biPy in solution (solid line) and in TiO_2 film (dashed line). (d) CV curves of ZnP, ZnP-Py and ZnP-biPy [2]

To understand the effect of ligands on dye energetics cyclic voltammetry analysis (CV) was carried out (Fig.5.4d). The energetics of the dyes are calculated via following equations:

$$HOMO = -[4.8 + (E_{OX} - E_{ferrocene})] \quad (5.2)$$

$$LUMO = HOMO + E_{0-0} \quad (5.3)$$

$$-\Delta G_{INJ} = LUMO + E_{CB} \quad (5.4)$$

where E_{OX} is the first oxidation potential onset, $E_{ferrocene}$ is found as 0.6 V, $E_{0\text{-}0}$ is calculated from absorption onset at lower energy level, ΔG_{inj} stands for electron injection energy and E_{CB} is conduction band energy of TiO_2 which is –4.05 eV [243]. The analysis showed that the complexation with 4-methylpyridine shifts the LUMO in positive direction. This minimizes the ΔG_{inj} but there is still enough energy for electron injection, therefore, lower J_{SC} of ZnP-Py can be understood as inefficient coordination with ligand and dye aggregation. In addition, CV results demonstrated similar positive shift of LUMO for ZnP-biPy; nevertheless,

ΔG_{inj} is sufficient for successful electron injection. However, unlike to ZnP-Py, the J_{SC} of ZnP-biPy systems did not show decrease. The increase in J_{SC}, therefore, can be ascribed to minimized dye aggregation due to coordination of ZnP porphyrin dye with bipyridine ligand.

Table 5. 2 Dye loading amount and the electrochemical and electron injection free-energy change parameters of ZnP complexes [2]

Mole ratio	Amount of dye (nmol cm^{-2})	HOMO (eV)	LUMO (eV)	$-\Delta G_{inj}$ (eV)
a) ZnP	41[a]	-5.08	-3.25	0.80
b) ZnP : Py				
1 : 0.5	40	-5.38	-3.55	0.50
1 : 1	39	-5.42	-3.59	0.46
1 : 2	37	-5.42	-3.59	0.46
c) ZnP : biPy				
1 : 0.5	36	-5.42	-3.59	0.46
1 : 1	36	-5.28	-3.45	0.60
1 : 2	34	-5.42	-3.59	0.46

[a] Data from reference [211].

5.4 Summary of the chapter

In this chapter we applied pyridine based ligands axially coordinated to porphyrin sensitizer to control dye aggregation. The self-assembly of porphyrin with 4,4'-bipyridine or 4-methylpyridine ligands was investigated by spectroscopic, computational, electrochemical and photovoltaic methods. The results demonstrated that axial coordinated ligands, especially 4,4'-bipyridine, were successful in suppressing porphyrin dye aggregation. The complexation with the ligands caused downward movement of porphyrin dye energetics (HOMO / LUMO) but in a range which does not affect electron injection. As a result, porphyrin – 4-methylpyridine (1:1) complex exhibited 4.63 % PCE, while porphyrin – 4,4'-bipyridine (1:0.5) complex showed 5.23 % efficiency demonstrating 28 % and 44 % improvement, respectively, as compared to porphyrin dye (3.62 %).

Chapter 6

6.1 Pt-free counter electrode based on the composite of CoS and orange fiber derived carbon

6.1.1 Introduction

The replacement of Pt as counter electrode of dye-sensitized solar cells has been addressed since the advent of DSSCs due to the scarcity and high cost of the metal. In addition, Pt counter electrodes have stability related problems limiting their long-term use in solar cells [154-158, 169]. Therefore, the development of Pt-free alternative counter electrode has been a hot topic in recent years. Among many candidates carbon based materials are of utmost interest due to their porous structure, desirable surface area and versatility of carbon source [187, 244-245]. Carbon composites have become attractive as Pt-free catalyst for DSSCs because of synergistic effect of components leading to remarkable performance and versatility of materials [246-248]. The composites of carbon with cobalt sulfide are highly attractive since the latter has demonstrated excellent property in reducing triiodide into iodide [195]. One common way of the preparation of such composites involves electrodeposition [249-250]. In this section, we present orange fiber derived mesoporous carbon embedded cobalt sulfide as an alternative to the Pt counter electrode of DSSCs. The proposed composite is synthesized using one-pot solvothermal method.

6.1.2 Characterization

The solvothermal reaction of orange fiber powder, sulfur and Co^{2+} in ethanol generated carbon embedded mixtures of cobalt sulfide. The XRD analysis of this as prepared product, OFC@Co_xS_y-AP, helped to identify different phases of cobalt sulfide (Fig.6.1). The peaks at 30.8°, 35.4°, 47.1°, 54.7° indicated the presence of CoS with planes (100), (101), (102), (110), whereas the peaks at 26.3°, 31.7° and 39.1°, 52.3° suggested the existence of Co_3S_4 and Co_9S_8 phases, respectively [251-253]. The same analysis of the product sintered at 200^{o}C, OFC@Co_xS_y-200, did not reveal any noticeable difference of the structure. On the other hand, the XRD analysis of the product sintered at 300^{o}C, OFC@Co_xS_y-300, produced peaks at 29.8°, 31.4°, 38.2°, 47.6°, 52.1°, 55.2° implying the structure of Co_9S_8 with (311), (222), (331), (511), (440) and (531) planes. This led to conclusion that sintering the product at 300^{o}C causes compositional and structural change producing pure Co_9S_8 phase without other 'parasitic' structures.

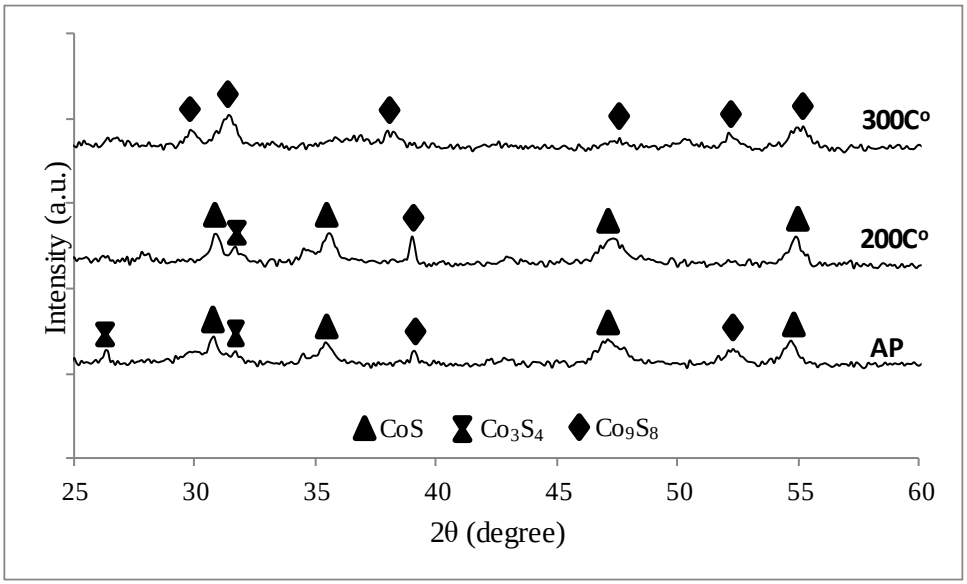

Figure 6. 1 XRD of as prepared and sintered at 200°C and 300°C samples [4]

To further investigate the effect of heating on OFC@Co_xS_y, the samples were analyzed on thermogravimetrical analyzer (TGA) (Fig.6.2). Heating the as prepared sample OFC@Co_xS_y-AP up to 900°C in air with 10°C/min rate produced a TGA curve with five distinct parts including three flat regions (Fig.6.2). At first, the sample is heated until 180°C where the weight is loss is minimal ~ 4 %. This is understood as the evaporation of solvent and adsorbed moisture. Further heating leads to a rapid drop in weight ~ 70 % and then the weight change is stabilized around 223°C. This drop is ascribed to the oxidation of unreacted orange fiber and partial removal of sulfur from cobalt sulfide phases which were demonstrated by XRD analysis (Fig.6.1). Further heating between 223 – 690°C went with no explicit weight change and this could be interpreted as the formation and heating of OFC@Co_xS_y-300. Beyond 690°C there is a small weight drop which is then stabilized. This weight change could be ascribed to the oxidation / combustion of embedded carbonaseous part and / or partial removal of sulfur. Similar analysis of OFC@Co_xS_y-200 and OFC@Co_xS_y-300 samples on TGA produced curves which are shown in Fig.6.2. Both TGA curves are comparable. Up until sintering temperatures (200 and 300°C) no weight loss is observed. Heating beyond sintering point leads to a rapid drop around 220°C for OFC@Co_xS_y-200. This is similar process as in the case of OFC@Co_xS_y-AP where this drop was ascribed to oxidation of unreacted orange fiber and partial removal of sulfur. Further heating proceeds with small weight loss for both OFC@Co_xS_y-200 and OFC@Co_xS_y-300 samples and this is explained as partial removal of sulfur and oxidation / combustion of embedded carbon.

The as prepared and sintered samples were also characterized by Fourier-transform infrared spectroscopy (FTIR) to analyze the organic portion and observe the effect of sintering (Fig.6.3). The graphs of OFC@Co_xS_y-AP and OFC@Co_xS_y-200 samples were found identical. The broad peaks at 3350–3100 cm^{-1} imply the presence of O-H bonding. This may come from organic portion of the samples containing cellulose, citric and ascorbic acids and other components. The signal at 2950–2850 cm^{-1} could be ascribed to the stretching vibrations of $-CH_2$, $-CH_3$, whereas the signals at 1585, 1364 and 1027 cm^{-1} imply the presence of carbon – oxygen chemical bonds such as C=O, COO^- and C-O. A weak signal at 823 cm^{-1} could be caused by conjugated C=C bonding. These findings support our previous claim of incomplete oxidation of orange fiber in OFC@Co_xS_y-AP and OFC@Co_xS_y-200 samples derived from XRD and TGA results. Therefore, sintering at 300^oC eliminated all these signals which can be seen from the FTIR graph of OFC@Co_xS_y-300 (Fig.6.3) and proves the oxidation of unreacted orange fiber. This claim was also demonstrated via elemental analysis. OFC@Co_xS_y-AP sample, according to the result, contains 13.81 ± 0.44 % carbon and 3.96 ± 0.12 % hydrogen which changes to 6.51 ± 0.12 % and 0.43 ± 0.01 %, respectively, upon sintering at 300^oC. This result also supports our assumption that ~ 7% weight loss around 700 °C of TGA analysis is due to the oxidation of embedded carbon.

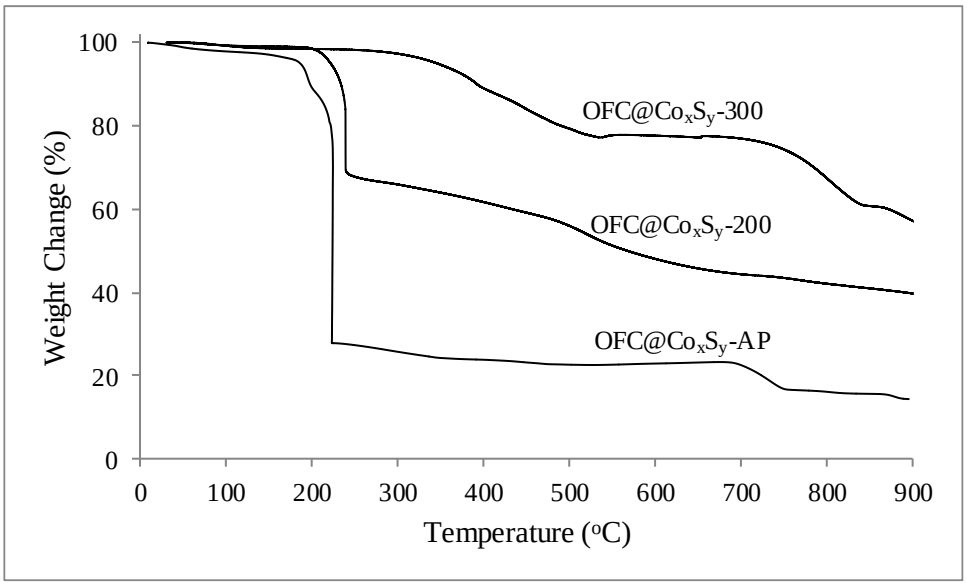

Figure 6. 2 TGA ramping curves of as prepared and sintered samples [4]

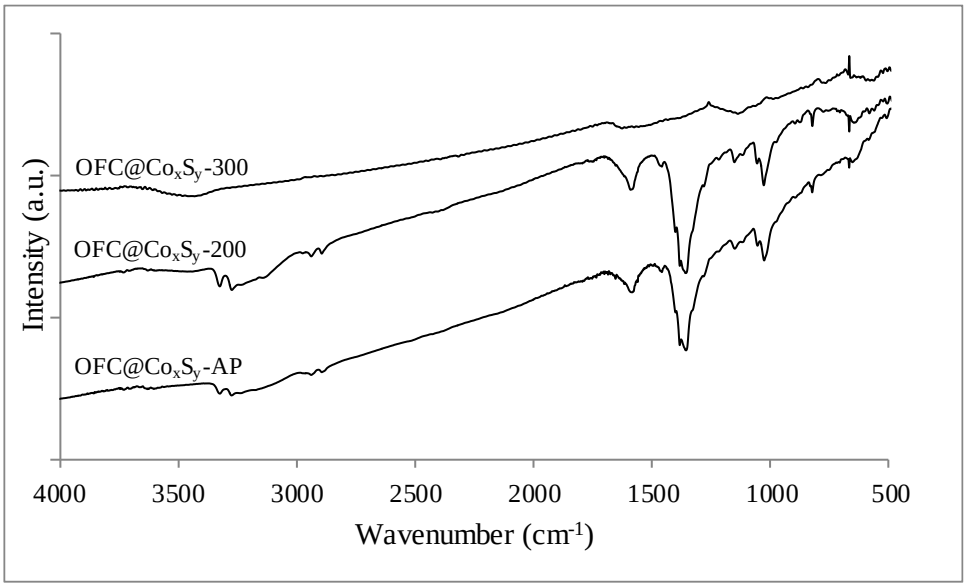

Figure 6. 3 FTIR spectrum of as prepared and sintered samples [4]

The valence states and elemental composition of OFC@Co_xS_y-300 were analyzed by X-Ray Phosphorescence Spectroscopy (XPS) and the spectra are presented in Fig.6.4. Due to extended contact with air the spectra are broad (FWHM > 3 eV). The peaks at 779.2 eV and 795.0 eV resulted from Co $2p_{3/2}$ and Co $2p_{1/2}$, respectively, with their equivalent satellites at 783.6 eV and 800.8 eV demonstrating II valence cobalt states (Fig.6.4a). These signals are by cause of Co-S bonding in Co_9S_8 [254]. The XPS spectrum of S was peak-fitted with three analogous spectra and shows a broad peak at 160 – 161.5 eV which is ascribed to S $2p_{3/2}$ and S $2p_{1/2}$ of Co-S bonds of Co_9S_8 (Fig.6.4b). The peak at 169.3 eV results from S-O species which appear due to superficial oxidation of sulfur with atmospheric oxygen [250, 254]. A broad peak corresponding to C 1s is found deconvoluted (Fig.6.4c). These include the signals of graphitic sp^2 (C=C) at 283.1 eV and amorphous sp^3 (C-C) carbon at 285.4 eV.

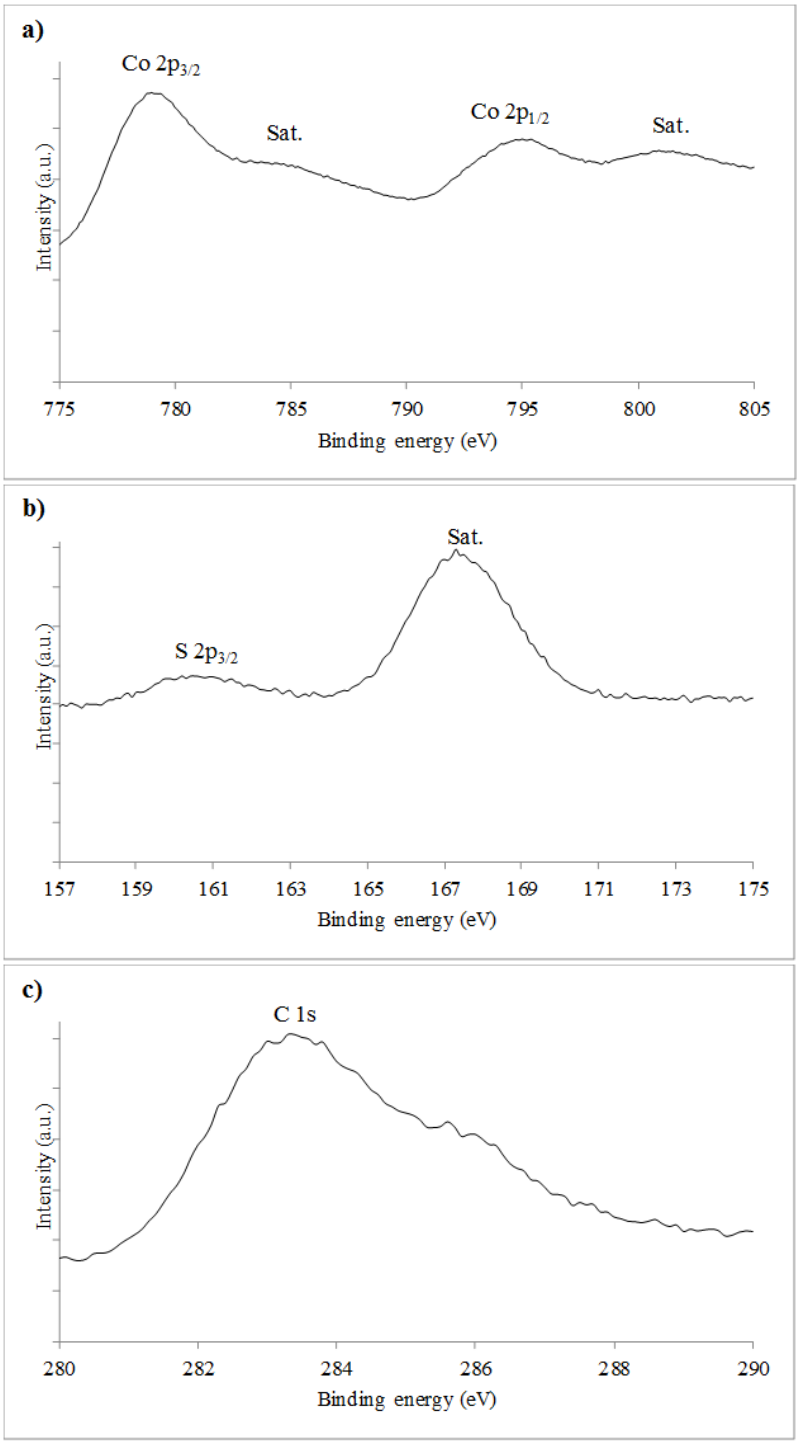

Figure 6. 4 XPS spectra of a) Co, b) S and c) C [4]

The characterization of as prepared and sintered samples on Scanning Electron Microscopy (SEM) exhibited nano-structured clusters of platelet / flake-like morphology with the size of a plate about 100 – 200 nm (Fig.6.5).

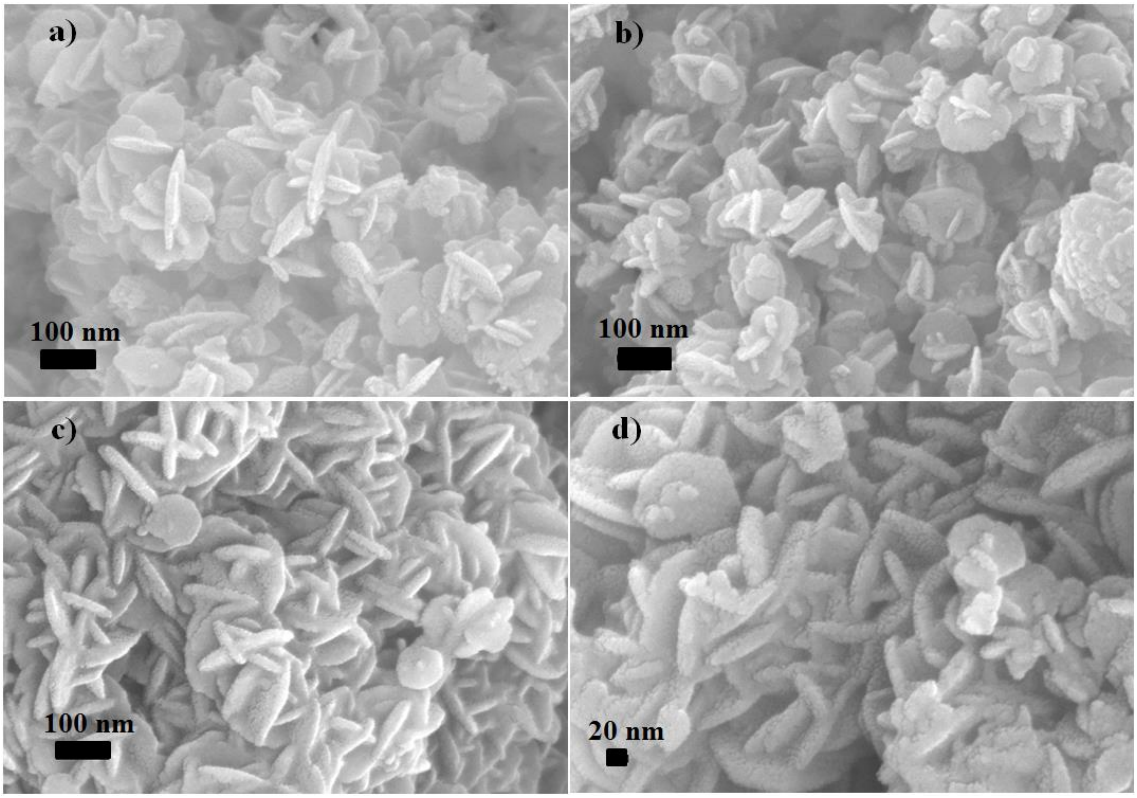

Figure 6. 5 SEM images of a) OFC@Co_xS_y-AP, b) OFC@Co_xS_y-200 and c-d) OFC@Co_xS_y-300

Compared to OFC@Co_xS_y-AP and OFC@Co_xS_y-200, the nanoflakes of OFC@Co_xS_y-300 are distinctly visible (Fig.6.5a-c) as the former two samples contain unreacted orange fiber. The nanoflakes of OFC@Co_xS_y-300 are well-defined as a result of the oxidation of the organic component due to heating above 200^oC which was witnessed on TGA analysis. These nanoflakes are cobalt sulfide structures which are comparable to other literature findings [252, 255-257]. To confirm this, the structures were further analyzed via Energy Dispersive X-Ray Spectroscopy (EDX) (Fig.6.6). The EDX spectra obtained from OFC@Co_xS_y-AP and OFC@Co_xS_y-200 samples precisely show the signals corresponding to Co, S and C (Fig.6.6 A-B). Similar signals were demonstrated by the OFC@Co_xS_y-300 sample EDX spectrum which, in addition, exhibit uniform distribution of the elements all over the film. The peaks corresponding to Sn on OFC@Co_xS_y-300 EDX spectrums were caused by the fluorine-doped tin oxide glass substrate.

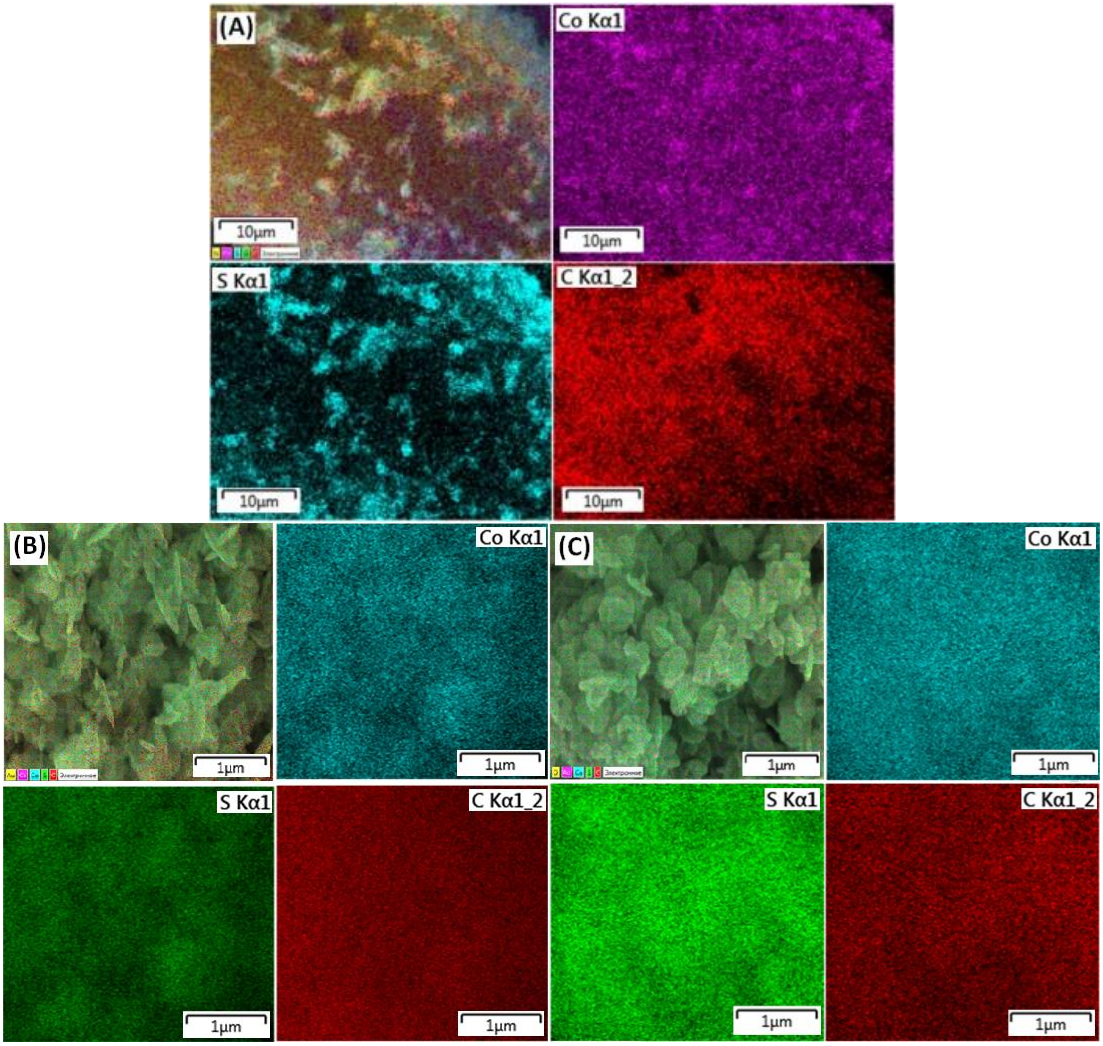

Figure 6. 6 EDX mapping of (A) OFC@Co_xS_y-AP, (B) OFC@Co_xS_y-200 and (C) OFC@Co_xS_y-300

The porosity and surface area of the sintered samples were examined by nitrogen porosimeter. The obtained graphs of pore size distribution and adsorption – desorption isotherms are depicted in Fig.6.7. Careful observation of the adsorption-desorption curves revealed that both of them represented isotherm of Type IV with a characteristic type H3 hysteresis loop caused by irreversible capillary condensation-evaporation within pores. This brought us to conclude that the structures of OFC@Co_xS_y-200 and OFC@Co_xS_y-300 are of mesoporous nature [258]. The former sample has a very small hysteresis loop of $0.8 < P / P_0 < 1.0$, whereas the hysteresis loop of OFC@Co_xS_y-300 is bigger and in the range of $0.5 < P / P_0 < 1.0$ (Fig.6.7a-b). According to literature [259] this type of loops tells about aggregates of plate-like particles of slit-shaped pores. The distribution of pore size was derived from adsorption isotherms of corresponding sample (Fig.6.7). It was calculated that the pore size of both

samples is within 2 – 50 nm with 24 nm dominant pore size for OFC@Co_xS_y-200 and 4 – 15 nm for OFC@Co_xS_y-300. The BET (Brunauer–Emmett–Teller) surface areas of the sintered samples were calculated and found to be higher for OFC@Co_xS_y-300 than for OFC@Co_xS_y-200, 9.9 and 7.4 m^2/g, respectively. This is explained as the effect of high temperature sintering leading to oxidation of organic component.

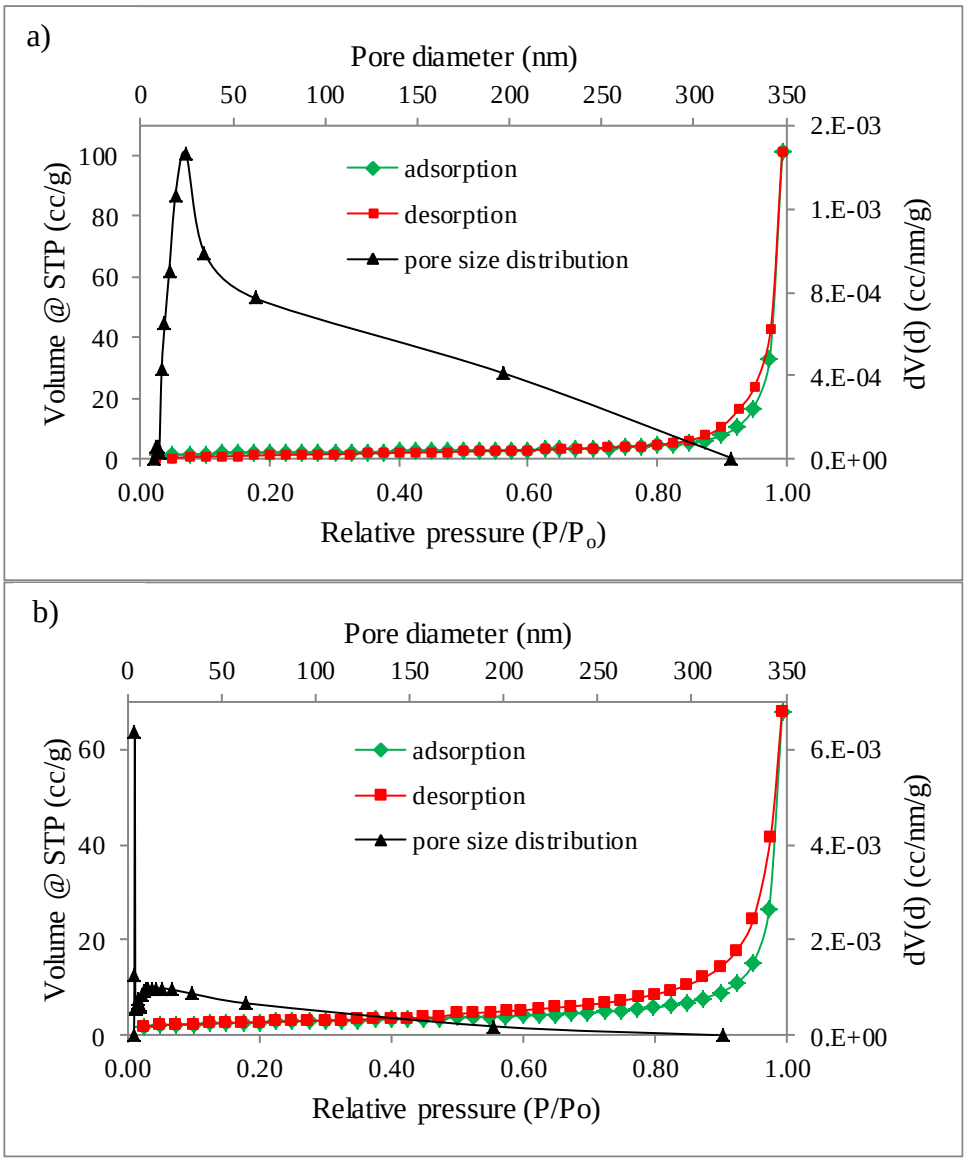

Figure 6. 7 N_2 adsorption-desorption isotherms and pore size distribution of a) OFC@Co_xS_y-200 and b) OFC@Co_xS_y-300 [4]

6.1.3 Photovoltaic performance

DSSCs were fabricated to evaluate the photovoltaic behavior of counter electrodes made of OFC@Co_xS_y catalyst. The counter electrodes (CEs) were prepared from the paste of the catalyst doctor bladed over FTO substrates and sintered at 200ºC and 300ºC for 30 min under air. To prepare the paste the

catalyst was dispersed in ethylene glycol / terpineol (10:1) mixture using agate mortar. Optimal concentration of the catalyst was found by varying its amount from 2.5 mg to 40 mg in 400 µL of 10:1 ethylene glycol / terpineol mixture. Doctor bladed FTO substrates were sintered at 300°C for 30 min under air before assembling into DSSCs. The photovoltaic results of CEs with different amounts of the catalyst are shown in Appendices B Fig.B.1 and Table B.1. As the result demonstrated, CE prepared from a paste with 5 mg of OFC@Co_xS_y-AP dispersed in 400 µL of binder mixture showed the best performance. This concentration was used in the preparation of pastes for OFC@Co_xS_y-200 and OFC@Co_xS_y-300 CEs. The photovoltaic I-V characterization and parameters of these cells are shown in Fig.6.8 and Table 6.1. Pt CE was used as a control cell. As the results demonstrate the differences in the values of open-circuit photovoltage V_{OC} and short-circuit photocurrent density J_{SC} between three cells are minimal. Fill factor FF values, on the contrary, have significant differences which can be seen from the shapes of the I-V curves of the cells (Fig.6.8).

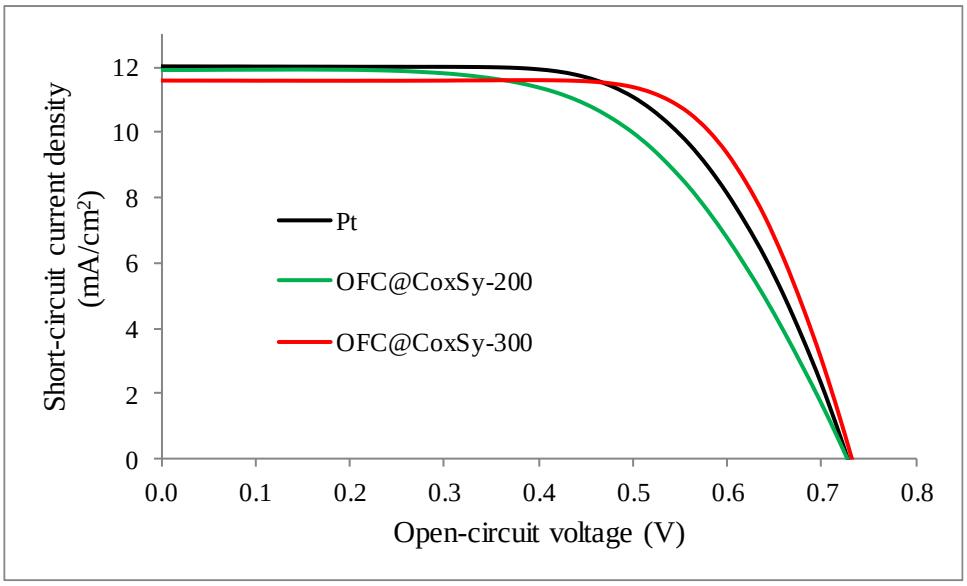

Figure 6. 8 I-V characterizations of solar cells [4]

Principally, there are two factors that govern the shape of I-V curves: series resistance R_S and shunt resistance R_{Sh}. An ideal solar cell with FF close to unit has negligible series resistance value and huge shunt resistance value making the shape of I-V graph close to a rectangle. Each of the resistances affect a particular side of the rectangle. Minimal series resistance induces stability of the voltage at higher current making the side of I-V curve to be parallel to y-axis. Similarly, higher shunt resistance causes the stability of cell current at elevated

voltages, thus, making the other side of I-V curve parallel to x-axis. Therefore, we assume high shunt resistances for three DSSCs as the photocurrent is stable at elevated voltages. To the contrary, the decay of voltage at elevated cell current is noticeable different for three DSSCs. For example, OFC@Co_xS_y-200 has the most rapid voltage decrease with increasing current, whereas OFC@Co_xS_y-300 demonstrated the most balanced voltage decay when increasing the current compared to OFC@Co_xS_y-200 and Pt cells (Fig.6.8). This can also be seen from the FF values (Table 6.1): OFC@Co_xS_y-200 < Pt < OFC@Co_xS_y-300 which led us to investigate the behavior of R_S of the DSSCs.

Table 6. 1 Photovoltaic parameters of dye-sensitized solar cells [4]

Cells	Eff (%)	Voc (V)	Jsc (mA/cm^2)	FF
OFC@Co_xS_y-200	5.01±0.28	0.72±0.00	11.91±0.09	0.58±0.03
OFC@Co_xS_y-300	5.94±0.19	0.74±0.00	11.58±0.09	0.69±0.02
Pt	5.57±0.19	0.73±0.01	12.02±0.02	0.64±0.03

6.1.4 Electrochemical performance

The cell resistances are studied via Electrical Impedance Spectroscopy (EIS) method; hence, the solar cells were analyzed on EIS with -0.72 V forward bias, 10 mV amplitude and 10^{-1} - 10^{5} Hz frequency range under dark condition. The results were obtained as Nyquist plots which were fitted by an EIS program on computer using an equivalent circuit (Fig.6.9).

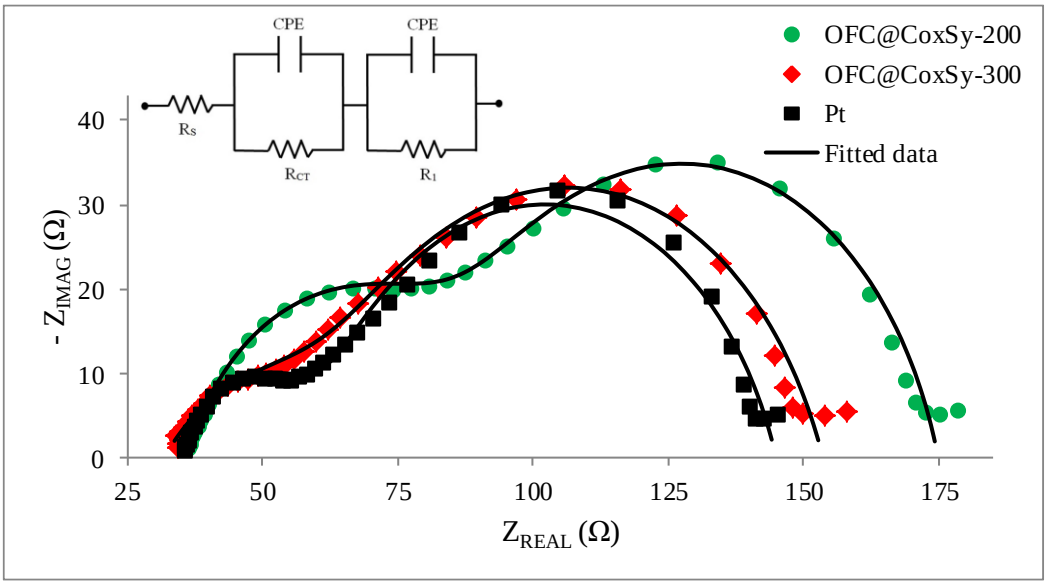

Figure 6. 9 Nyquist plots of solar cells and equivalent electrical circuit (inset) [4]

Table 6. 2 Electrochemical parameters of the solar cells [4]

Cells	R_S	R_1	R_{CT}
Pt	34.74	83.64	26.6
OFC@Co_xS_y-200	35.82	86.64	52.47
OFC@Co_xS_y-300	31.79	85.67	36.22

The Nyquist plots contain two semicircles which were fitted using the equivalent circuit shown in Fig.6.9 as inset. The intercept of the Nyquist plots with x-axis represents series resistance (R_S). The first and smaller semicircle portrays charge transfer resistance at electrolyte / CE interface (R_{CT}), whereas the second and bigger semicircle stands for the charge transfer resistance at TiO_2 / dye / electrolyte interface (R_1). In general, the series resistance of DSSCs is the combination of internal cell resistances as resistance of transparent conducting oxide (TCO) layer (R_h), Nernst diffusion resistance of electrolyte (R_W) and charge transfer resistance at electrolyte / CE interface (R_{CT}):

$$R_S = R_h + R_W + R_{CT} \tag{6.1}$$

Since R_{CT} is determined separately, the presented R_S in Table 6.2 can be viewed as the sum of R_h and R_W. The findings of EIS analysis revealed that the values of R_S and R_1 are almost alike since TCO and diffusion resistances (R_h and R_W) are assumed constant in all three cells; moreover, the TiO_2 / dye / electrolyte interface for the solar cells are also identical. Consequently, the

difference of FFs can be explained in terms of R_{CT} values. OFC@Co_xS_y-200 has the lowest FF (Table 6.1) and the EIS experiment revealed that its charge transfer resistance at electrolyte / CE interface is the highest. This implies that OFC@Co_xS_y-200 demonstrated poor catalytic activity in regenerating I_3^- to I^-. Such low catalytic activity could be the result of insufficient oxidation of the organic component. Contrarily, OFC@Co_xS_y-300 cell exhibited much superior catalytic activity in electrolyte regeneration than OFC@Co_xS_y-200 cell, having significantly lower R_{CT}, 36.22 Ω which led to higher FF = 0.69. This is explained as the effect of oxidation of the orange fiber upon sintering at 300^{o}C. The R_{CT} of Pt cell was found the lowest, 26.6 Ω; however, its FF is inferior to that of OFC@Co_xS_y-300. This could be the result of other factors as some literature claim that apart from R_{CT}, FF value is affected by the rate of V_{OC} decay and recombination, open-circuit photovoltage and ideality factor [260-261]. Thus, the catalytic activity of OFC@Co_xS_y-300 was found to be closer to that of Pt CE which led to the highest 5.94 % PCE outperforming the reference Pt cell with 5.57 % efficiency.

6.1.5 Stability of OFC@Co_xS_y-300 device

The stability of OFC@Co_xS_y-300 CE activity in solar cell was also tested at ambient conditions (T = 298^{o}K). The device was kept in the dark at ambient temperature and its efficiency was measured periodically. The cells demonstrated fairly stable behavior over the period of 10 days. At the end of the indicated period the cells maintained 87 % of its initial parameter (Fig.6.10).

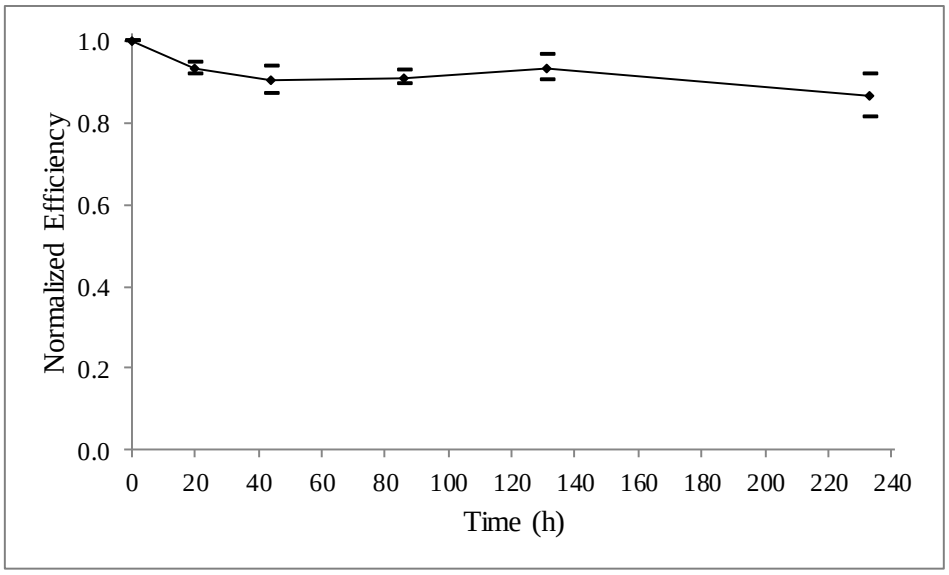

Figure 6. 10 Stability of champion device OFC@Co_xS_y-300 [4]

6.1.6 Summary of section 6.1

In this section a composite of cobalt sulfide and orange fiber derived carbon was prepared using one-pot solvothermal synthesis and sintering at 200^{o}C and 300^{o}C to ensure carbonization (oxidation) of the organic components. Detailed instrumental analysis revealed nanoflake-like structured cobalt sulfide decorated with orange fiber derived carbon. High temperature sintering guarantees complete carbonization, whereas incomplete oxidation of the organic component was observed at 200^{o}C sintering. Sintering at 300^{o}C produces a mesoporous composite with pore diameter 4-15 nm. The photovoltaic and electrochemical analysis demonstrates remarkable catalytic activity of the sample as counter electrode for dye-sensitized solar cells with liquid electrolyte exhibiting 5.94 % PCE. This is higher than the reference Pt-based device (5.57 %).

6.2 Pt-free counter electrodes based on Cu-Co-S ternary sulfides

6.2.1 Introduction

Transition metal sulfides and their composites have demonstrated outstanding results as alternative to Pt CEs [200, 262-264]. The idea of using more than one metal sulfide to further improve their performance led to the development of ternary and quaternary transition metal sulfide counter electrodes. Presence of more than one metal allows changing their ratio to tune redox potentials, band-gap and electronic properties. There are many successful candidates that exhibited impressive performance as DSSC CE. Some of them are $CoIn_2S_4$ [209], $Ni_{1-x}Mo_xS$ [265], $Ni_{0.5}Fe_{0.5}S_2$ [207], $NiCo_2S_4$ [266], $CoMoS_4$ and $NiMoS_4$ [267]. However, there is lack of research on ternary Cu-Co-S complexes as counter electrodes for DSSCs. Therefore, in this section, we describe the use of ternary sulfide Cu-Co-S solvothermally grown on TCO substrate as Pt-free CE for the reduction of triiodide redox species.

6.2.2 Characterization

The direct growth of binary copper-cobalt-sulfide on FTO glass substrate via solvothermal method with different reagent ratio produced three $Cu_xCo_yS_z$ covered FTO (Fig.6.11). From visual inspection, the substrate surfaces were covered by the product but at different levels.

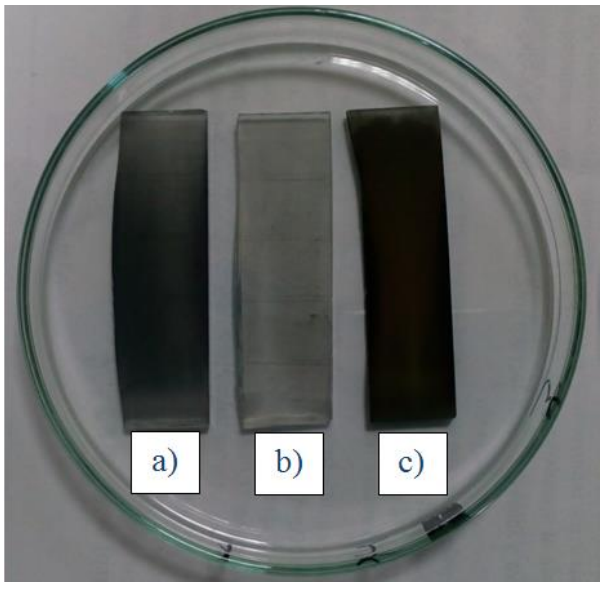

Figure 6. 11 FTO glass substrates with solvothermally grown a) $Cu_xCo_yS_z$-1 b) $Cu_xCo_yS_z$-2 and c) $Cu_xCo_yS_z$-3

Scanning Electron Microscopy analysis reveals that the samples $Cu_xCo_yS_z$-1 and $Cu_xCo_yS_z$-3 have fully covered surfaces, whereas $Cu_xCo_yS_z$-2 demonstrates

isolated cluster of micro-sized structures reaching 10 µm (Fig.6.12). Because of incomplete surface covering in $Cu_xCo_yS_z$-2 parts of FTO is exposed. The crystals of $Cu_xCo_yS_z$-1 are of matching sizes and the crystals of $Cu_xCo_yS_z$-3 are evenly stacked. The Energy Dispersive X-Ray Spectroscopy (EDX) analysis show homogeneous distribution of Cu, Co and S (Fig.6.13). The ratio of the elements was obtained from the same analysis (Table 6.3). Among all, the composition of $Cu_xCo_yS_z$-1 sample mostly resembles $CuCo_2S_4$.

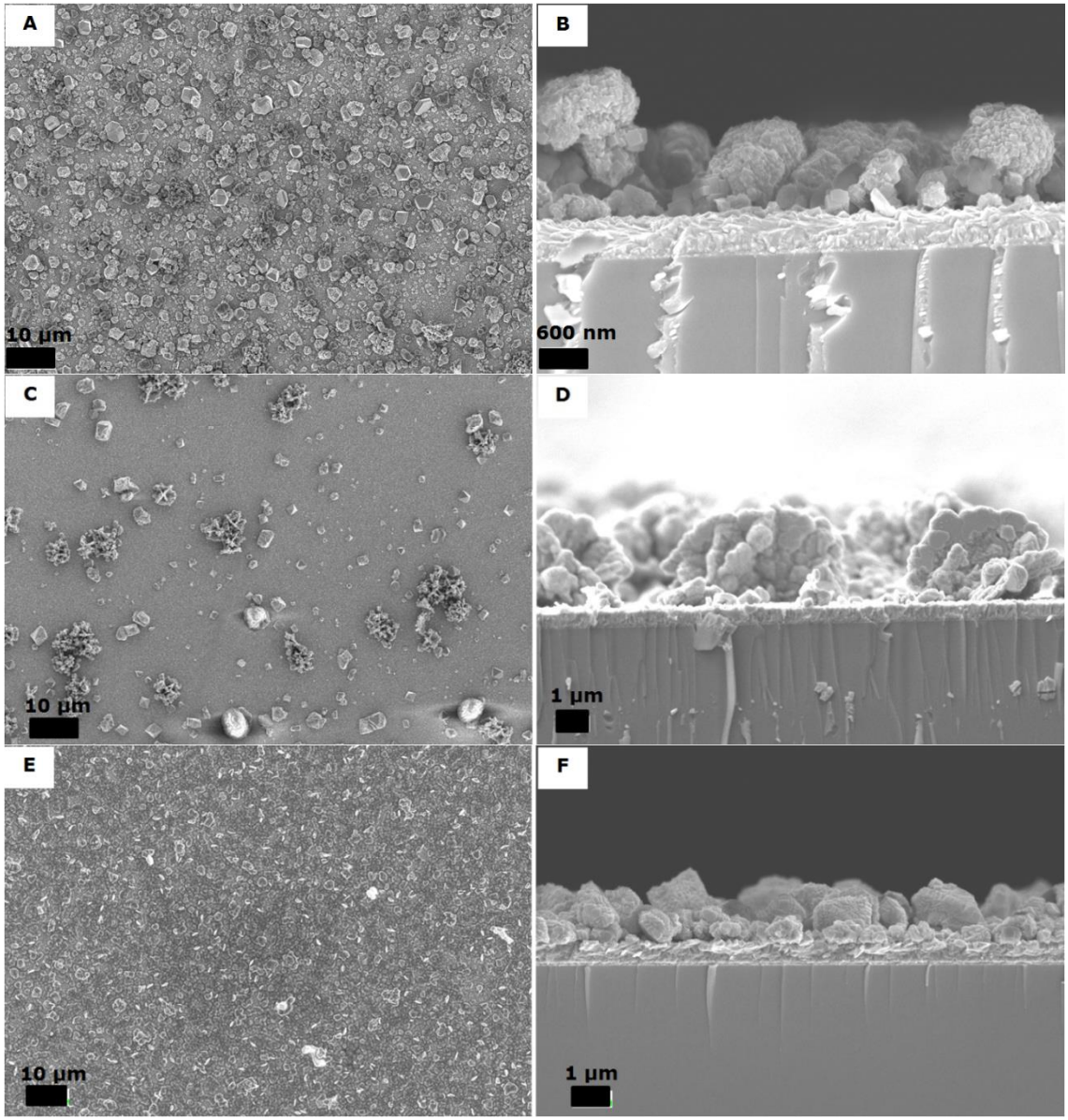

Figure 6. 12 SEM images and cross-section of $Cu_xCo_yS_z$-1 (A-B), $Cu_xCo_yS_z$-2 (C-D) and $Cu_xCo_yS_z$-3 (E-F) counter electrodes

X-Ray Diffraction (XRD) analysis of the samples exhibited carrollite-like structure ($CuCo_2S_4$) (Fig.6.14). The signals at 26.6º, 31.2º, 37.8º, 46.3º, 49.8º and 54.8º for samples $Cu_xCo_yS_z$-1 and $Cu_xCo_yS_z$-2 correspond to (2 2 0), (3 1 1), (4 0 0), (4 2 2), (5 1 1) and (4 4 0) faces of $CuCo_2S_4$, respectively (RRUFF ID: R040165.1),

whereas the signals at 27.9º and 32.3º could result from 'parasitic' CuS structures (RRUFF ID:R060129.1). The additional peak at 39.0º in $Cu_xCo_yS_z$-1 could be caused by Cu_2S structure (RRUFF ID: R180023). Unlike the first two samples, the XRD of $Cu_xCo_yS_z$-3 is only composed of peaks at 26.6º, 31.2º, 37.8º, 49.8º and 54.8º characteristic of (2 2 0), (3 1 1), (4 0 0), (5 1 1) and (4 4 0) planes of $CuCo_2S_4$, respectively, but without a signal at 46.3º.

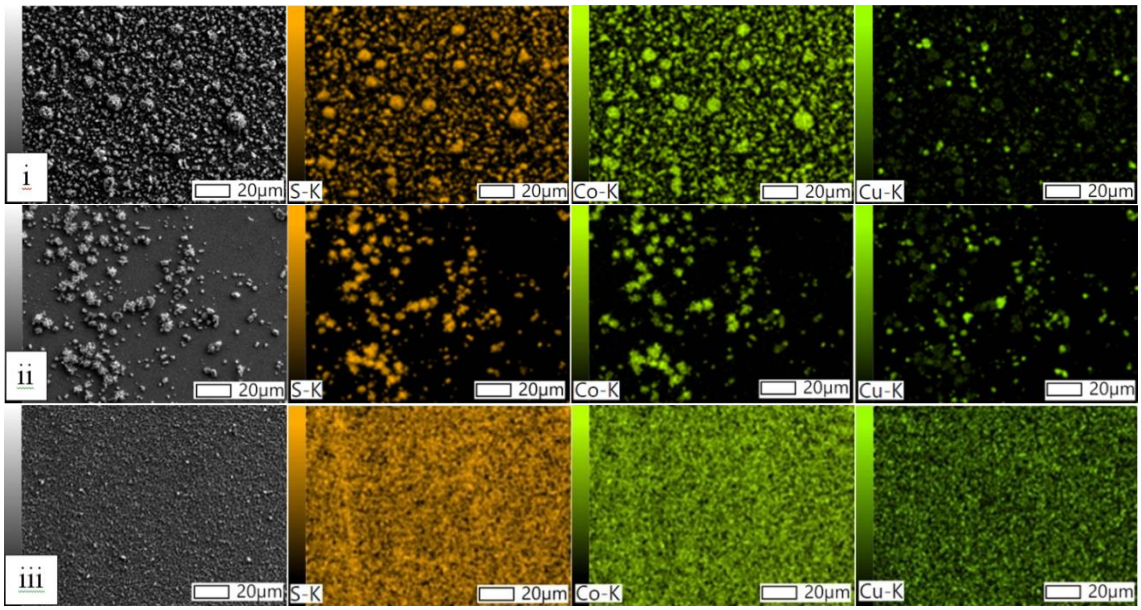

Figure 6. 13 EDX spectra of $Cu_xCo_yS_z$-1 (i), $Cu_xCo_yS_z$-2 (ii) and $Cu_xCo_yS_z$-3 (iii)

Table 6. 3 Percent composition of the samples [5]

Sample	Cu, wt%	Co, wt%	S, wt%	Formula
$Cu_xCo_yS_z$-1	20.47±0.07	41.59±0.08	37.94±0.05	$CuCo_{2.2}S_{3.7}$
$Cu_xCo_yS_z$-2	39.44±0.16	22.93±0.1	37.63±0.08	$Cu_{1.6}CoS_3$
$Cu_xCo_yS_z$-3	8.26±0.04	44.02±0.07	47.72±0.04	$CuCo_{5.8}S_{11.5}$

The Raman spectra of the samples compose of three peaks (Fig.6.15). The results of $Cu_xCo_yS_z$-1 and $Cu_xCo_yS_z$-3 are identical having peaks at 681 cm^{-1}, 515 cm^{-1}, and 476 cm^{-1} which is close to $CuCo_2S_4$. The peaks at 681 cm^{-1} and 515 cm^{-1} are caused by Co-S bonding, whereas the third signal is the result of Cu-S bond [268]. $Cu_xCo_yS_z$-2 sample has also three peaks; however, the signals are blue-shifted (Fig.6.15). This could be caused by the stress within the structure by the presence of extra CuS components. Moreover, the peak at the highest wavenumber is sharper which implies high degree of crystallinity in $Cu_xCo_yS_z$-3 sample than in other two.

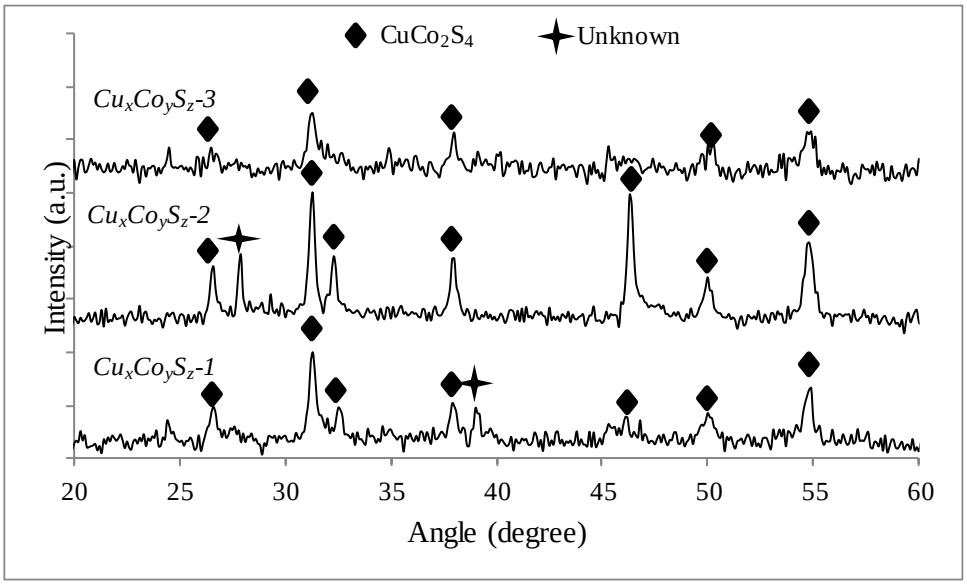

Figure 6. 14 XRD spectra of $Cu_xCo_yS_z$ samples [5]

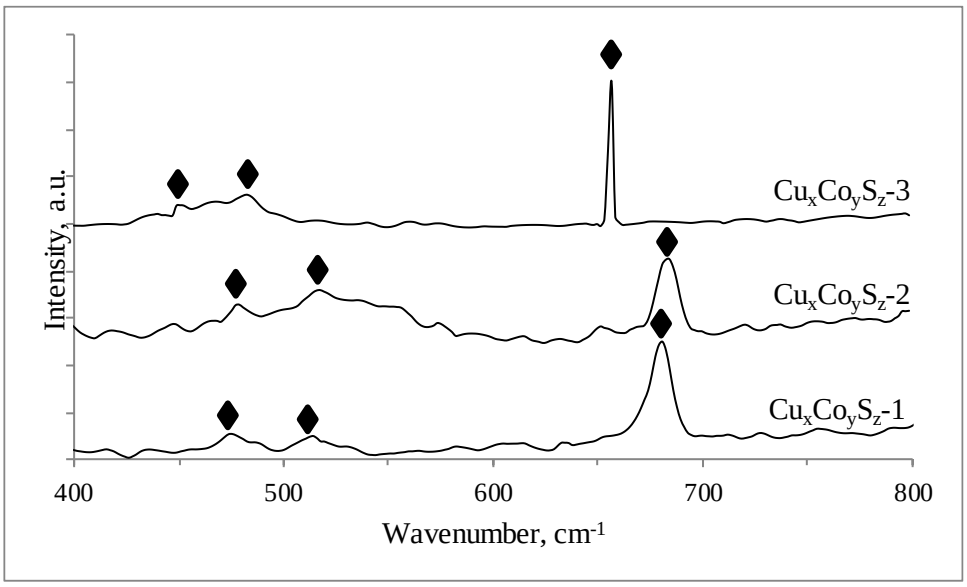

Figure 6. 15 Raman spectra of $Cu_xCo_yS_z$ samples [5]

6.2.3 Photovoltaic and Electrochemical Performance

DSSCs were fabricated using $Cu_xCo_yS_z$ electrodes to investigate their photovoltaic performance and compare with reference solar cell assembled using Pt counter electrode, see Fig.6.16. The catalytic activity of the counter electrodes in regenerating oxidized triiodide species were assessed by Electrochemical Impedance Spectroscopy (EIS) and obtained Nyquist plots are presented in Fig.6.17. The collected parameters are shown in Table 6.4.

Table 6. 4 Photovoltaic and Electrochemical Parameters of DSSCs [5]

DSSCs	Eff (%)	Voc (V)	Jsc ($mAcm^{-2}$)	FF	R_{CT}
Pt	7.75±0.08	0.73±0.01	18.69±0.78	0.57±0.02	36.73
$Cu_xCo_yS_z$-1	7.61±0.02	0.72±0.00	17.79±0.53	0.60±0.02	37.16
$Cu_xCo_yS_z$ -2	6.59±0.24	0.72±0.00	18.81±0.26	0.49±0.02	46.82
$Cu_xCo_yS_z$ -3	8.60±0.08	0.72±0.00	19.44±0.27	0.62±0.00	32.66

Generally all $Cu_xCo_yS_z$ samples demonstrated remarkable performance as counter electrodes with comparable PCEs with Pt CE. The V_{OC} of all cells are identical and the difference is in the photocurrent and fill factor. $Cu_xCo_yS_z$-1, for example, showed 98 % efficiency of the reference cell due to inferior J_{SC} although its FF was higher than that of Pt. Low photocurrent of $Cu_xCo_yS_z$-1 is the result of its minor deficiency in reducing oxidized electrolyte compared to Pt as seen from its charge transfer resistance R_{CT}. The latter is derived from Nyquist plots by fitting it using equivalent circuit shown as inset (Fig.6.17). The smaller semi-circle represents charge transfer resistance at counter electrode / electrolyte interface R_{CT}. It is inversely proportional to exchange current density at counter electrode / electrolyte boundary J_0 which can be assumed equal to short-circuit current density J_{SC}. The equation 6.2 describing the relationship between R_{CT} and J_0 is given below [269]:

$$R_{CT} = \frac{RT}{nFJ_0} \tag{6.2}$$

where R is universal gas constant, T is absolute temperature, n is number of electrons (for $I_3^- + 2e \rightarrow 3I^-$ n = 2) and F is Faraday's constant. $Cu_xCo_yS_z$-2, on the other hand, generated higher J_{SC} than Pt cell but due to smaller fill factor it exhibited 6.59 % PCE which is 85 % the efficiency of Pt. From the equation 6.2, the high photocurrent of $Cu_xCo_yS_z$-2 may imply lower charge transfer resistance at CE / electrolyte interface; however, the EIS analysis shows significantly high R_{CT} (46.82Ω) compared to Pt. This is explained by poor surface coverage of $Cu_xCo_yS_z$-2 with large exposed FTO area as shown by SEM images. This is also the reason of low FF for the cell. Therefore, it is assumed that improving the surface coverage by increasing reagent concentrations or synthesis time may lower R_{CT} and boost FF. The third candidate $Cu_xCo_yS_z$-3 demonstrated

outstanding photovoltaic performance outperforming Pt reference cell in PCE by 11 %. This was achieved by notably superior J_{SC} and FF. The EIS analysis revealed impressive electrocatalytic activity of Cu_xCo_ySz-3 counter electrode in regenerating redox electrolyte. The charge transfer resistance of Cu_xCo_ySz-3 is noticeably lower than that of Pt. Hence, Cu_xCo_ySz-3 was found excellent candidate as Pt – free counter electrode for dye-sensitized solar cell.

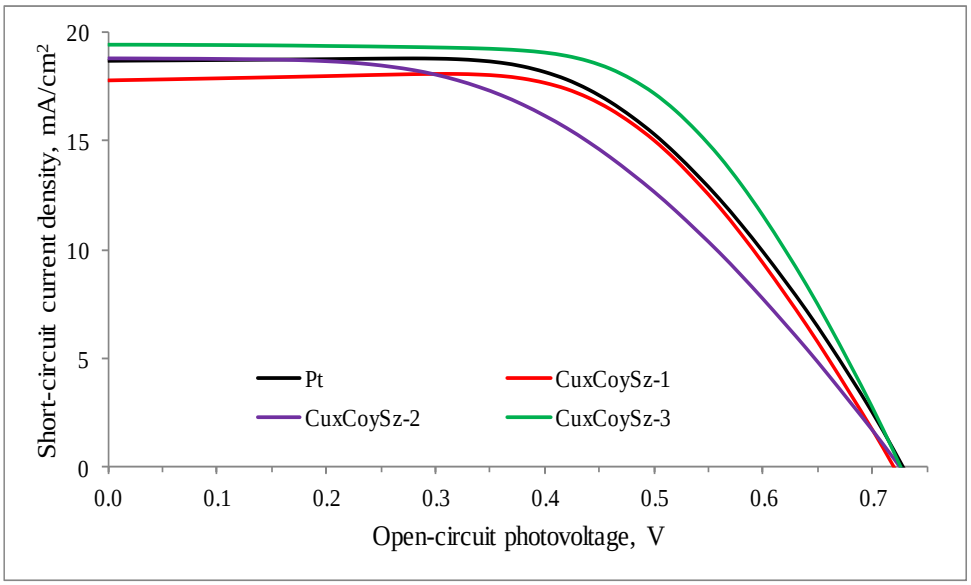

Figure 6. 16 I-V characterization of cells [5]

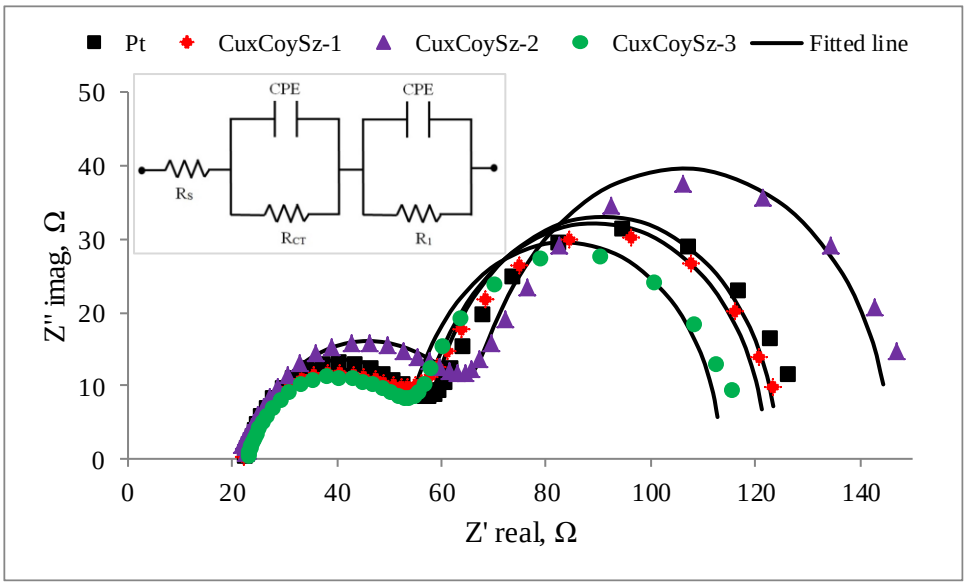

Figure 6. 17 Nyquist plots of the cells and equivalent electrical circuit (inset) used in data fitting [5]

6.2.4 Summary of the section

In this section ternary copper-cobalt-sulfide (Cu-Co-S) counter electrodes were prepared following direct growth on fluorine-doped tin oxide glass substrate via

solvothermal synthesis and characterized by SEM, EDX, XRD and Raman Spectroscopy. Changing the concentrations of reactants allowed to obtain three samples with different component ratios ($Cu_xCo_yS_z$-1, $Cu_xCo_yS_z$-2 and $Cu_xCo_yS_z$-3). The sample $Cu_xCo_yS_z$-3 (formula $CuCo_{5.8}S_{11.5}$) exhibited excellent photovoltaic and electrochemical properties and the efficiency of DSSC with $Cu_xCo_yS_z$-3 CE (8.60 %) was 11 % higher than that of Pt CE (7.75 %).

6.3 Ternary $CuCo_2S_4$ nanoflowers as efficient CE for DSSCs

6.3.1 Introduction

Following the remarkable performance of binary copper-cobalt-sulfides, $Cu_xCo_yS_z$ which were prepared by mixing copper, cobalt and sulfur sources in different ratios [5], an attempt was made to synthesize $CuCo_2S_4$ to apply it as Pt-free counter electrode for dye-sensitized solar cell. The compound has attractive properties as high conductivity, excellent electrochemical characteristics and low cost. It has been successfully used as cathode in energy storage devices [270], supercapacitor [271] and catalyst [272-273]. These properties make it a suitable candidate as counter electrode material for DSSC. In this section we present the synthesis and characterization of $CuCo_2S_4$ as Pt-free counter electrode for DSSC application.

6.3.2 Preparation and Characterization

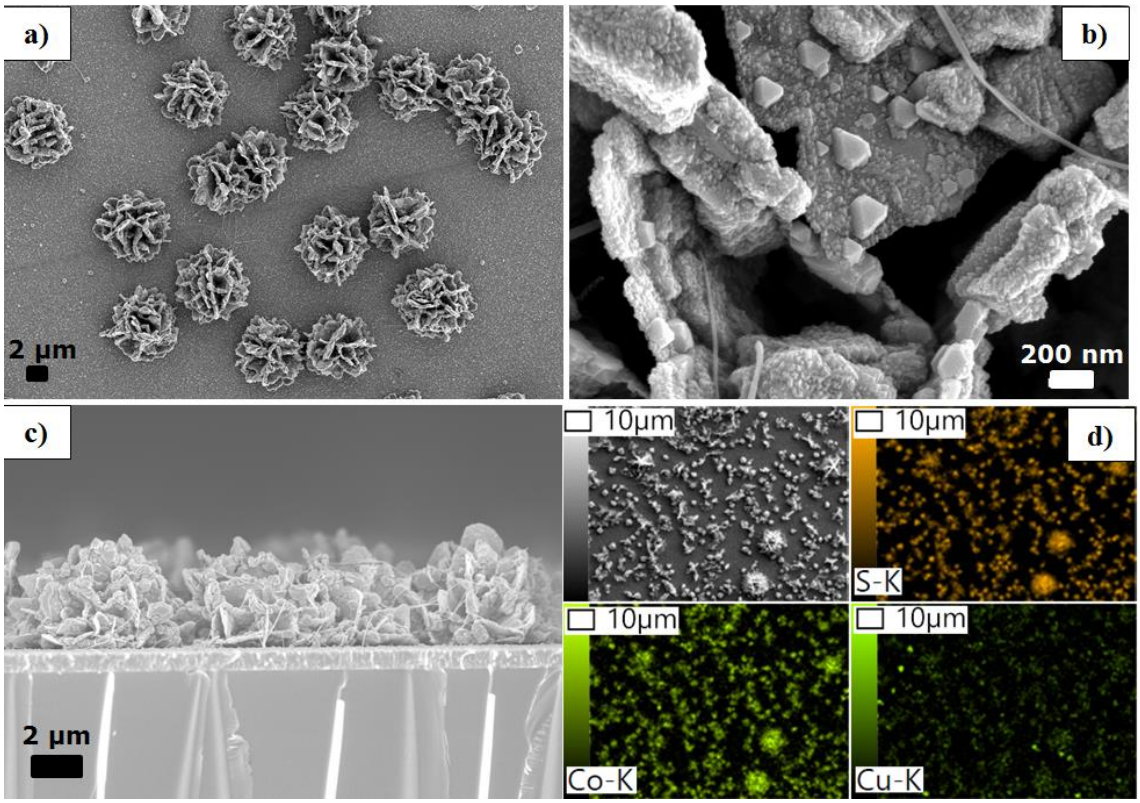

Figure 6. 18 SEM images (a-c) and EDX mapping (d) of nano structured $CuCo_2S_4$ flowers

In an attempt to synthesize $CuCo_2S_4$ covered FTO electrode, the reagents were mixed in ratio to make Cu:Co:S = 1:2:8 (sulfur source was taken in excess) and treated solvothermally at 200^oC for 4 hours similar to previously reported method [5]. The analysis of the obtained product on Scanning Electron Microscopy (SEM) revealed flower shaped structures with nanopetals (Fig.6.18). The

thickness of the petals is around 100 – 300 nm range from a close observation on SEM (Fig.6.18b). A complex network of such petals make a flower shaped structure with approximate diameter of 8–9 µm. The height of the structures is around 4-5 µm as seen from SEM analysis of the cross-section (Fig.6.18c). The sample is composed of Cu, Co and S which are evenly distributed over the nanoflowers as seen from Energy Dispersive X-Ray Spectroscopy analysis (Fig.6.18d). However, the EDX signals of Cu are less intense compared to Co and S. The weight percent distribution calculated from EDX for Cu:Co:S is almost the same as the actual $CuCo_2S_4$ compound (Table 6.5).

Table 6. 5 Elemental composition by weight

Elements	Wt % from EDX	Wt % Actual
Cu	20.30±0.19	20.52
Co	38.61±0.19	38.06
S	41.09±0.12	41.41

The study of the nanoflower sample on X-Ray Diffractometer gives a graph with peaks at 26.6º, 31.2º, 38.1º, 46.7º, 50.1º and 54.9º (Fig.6.19). These signals correspond to (220), (311), (400), (422) (511) and (440) facets of $CuCo_2S_4$ (JCPDS card No.42-1450). The obtained d-spacing for each facet is 0.334nm, 0.286nm, 0.235nm, 0.194nm, 0.181nm and 0.167nm, respectively. The Raman spectrum of the nanoflower sample contains three peaks (Fig.6.20). The peak at 466 cm^{-1} is due to lattice vibrational mode (S-S stretching) of Cu-S [274]. The peaks at 509 cm^{-1} and 670 cm^{-1} are due to F^1_{2g} and A_{1g} modes of Co-S [275]. The blue-shifting of the peaks is caused by structural disorders with more residual stress [276].

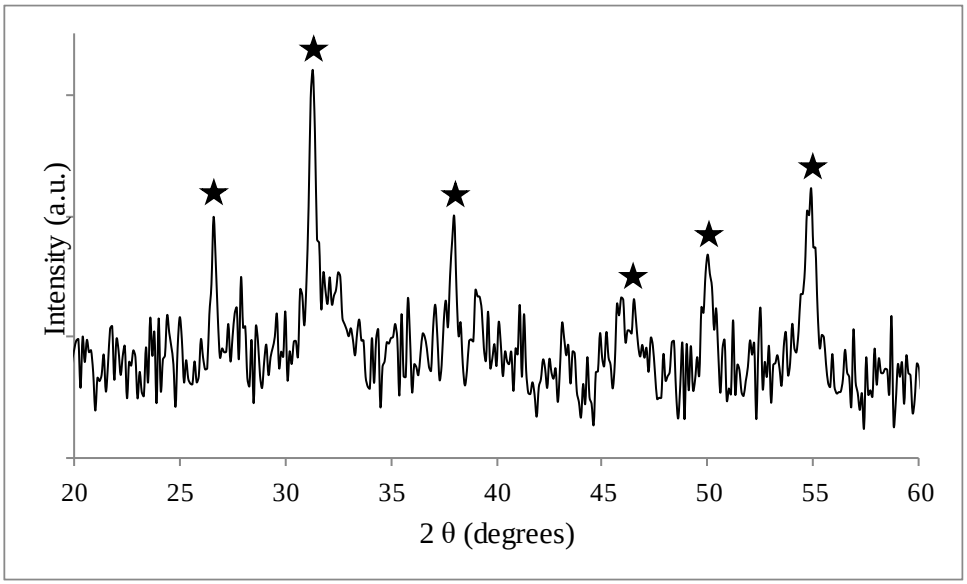

Figure 6. 19 XRD spectrum of $CuCo_2S_4$ nanoflower

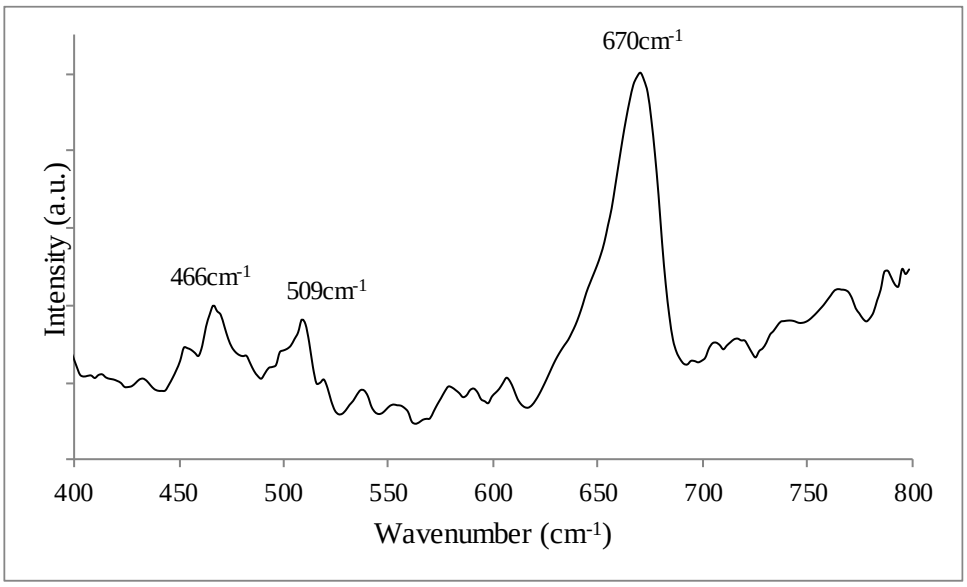

Figure 6. 20 Raman spectrum of $CuCo_2S_4$ nanoflower

N_2 porosimetry study of the product was performed to obtain adsorption – desorption isotherms and collect information about its pore size and specific surface area. The produced adsorption-desorption curve implies very weak interaction of the product with N_2 and the shape represents type IV isotherm (Fig.6.21) indicative of mesoporous nature of the nanoflowers. The BET surface area was calculated to be 36.99 m^2/g. The BJH pore size distribution is shown in Fig.6.22 and the dominating pore size is 3.72 nm. For sulfides the surface area is considered remarkably high [277]. This is desirable for superior electrocatalytic performance of the catalyst.

Thus, the extensive characterization of the product revealed successful formation of nanostructured flower shaped $CuCo_2S_4$ with mesoporous nature.

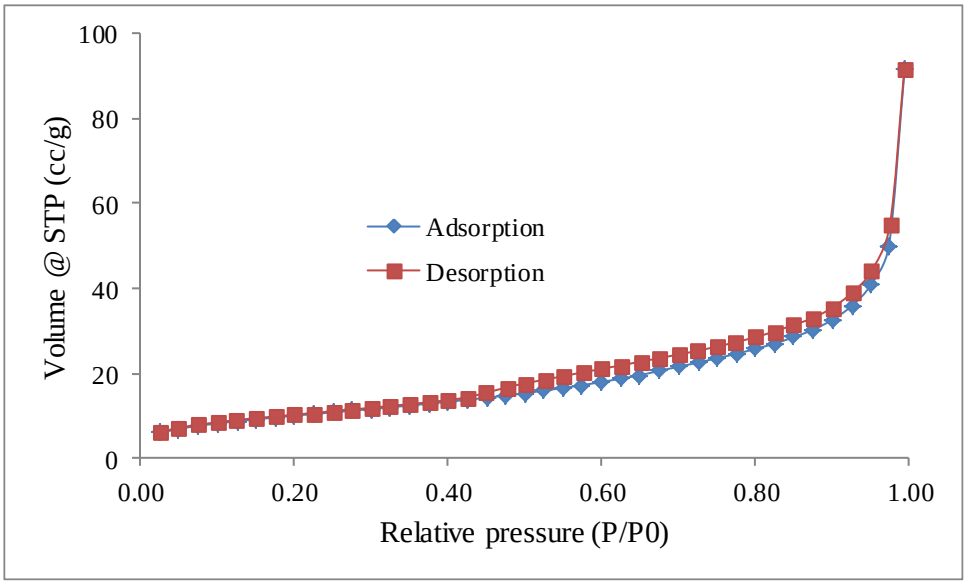

Figure 6. 21 Adsorption-desorption isotherm of $CuCo_2S_4$ nanoflower

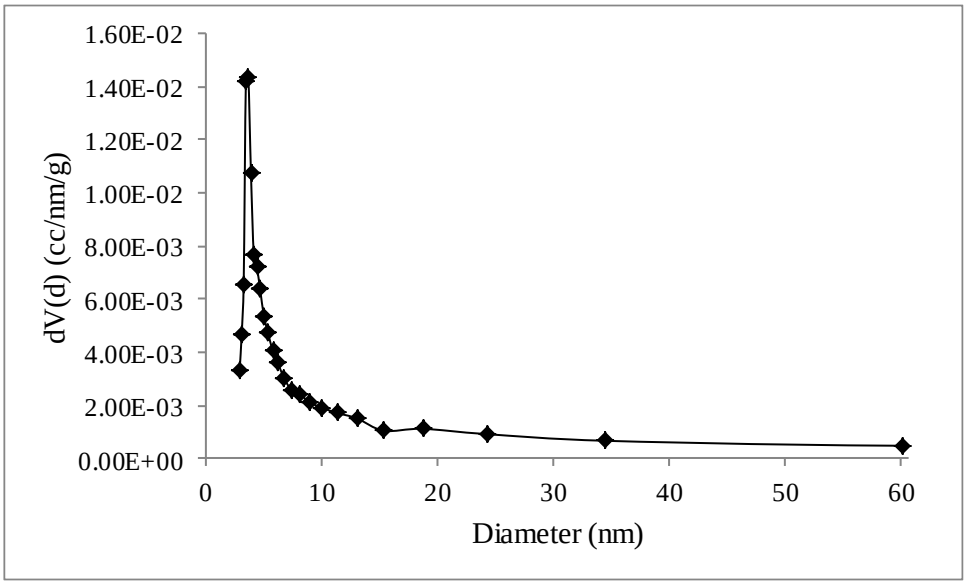

Figure 6. 22 Pore size distribution of $CuCo_2S_4$ nanoflower

6.3.3 Photovoltaic and Electrochemical Performance

The nanostructured flower shaped $CuCo_2S_4$ solvothermally grown on FTO glass substrate was assembled into dye-sensitized solar cell as counter electrode to test its photovoltaic and electrochemical behavior. The results were compared with that of reference cell made of Pt counter electrode, see Fig.6.23 and Fig.6.24.

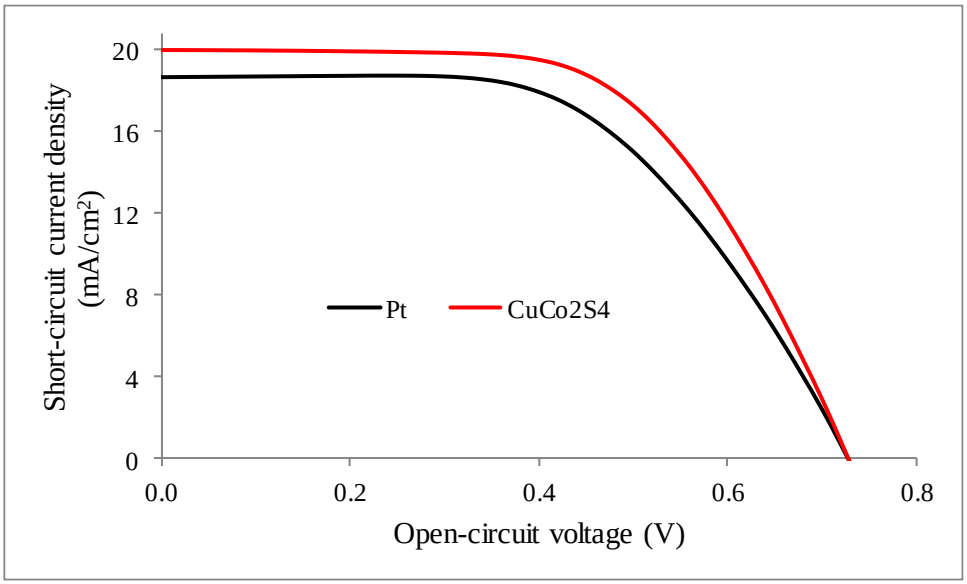

Figure 6. 23 I-V characterization

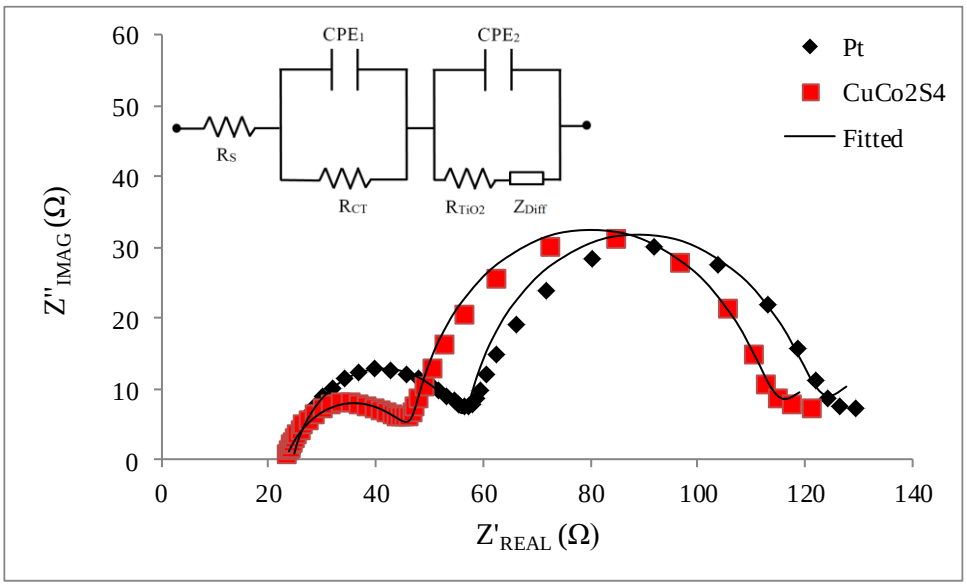

Figure 6. 24 Nyquiost plot of Pt and $CuCo_2S_4$. Inset: equivalent electrical circuit used for fitting

As a result $CuCo_2S_4$ CE demonstrated superior performance than Pt CE. The photovoltage of the cells were found the same, whereas the device with $CuCo_2S_4$ CE generated higher photocurrent than the cell with Pt CE (Table 6.6). Similar trend is observed for cell fill factors. The reason for the excellent performance of $CuCo_2S_4$ catalyst comes from its high surface area and mesoporous structure. Also the Electrical Impedance Spectroscopy analysis revealed better electrocatalytic activity of $CuCo_2S_4$ compared with Pt (Table 6.7). The series resistance R_S, recombination resistance R_{TiO2} and electrolyte diffusion resistance Z_{DIFF} of the devices are identical but the charge transfer resistances at CE / electrolyte interface R_{CT} differ significantly. A low R_{CT} of

$CuCo_2S_4$ cell compared with Pt shows that electrons flow faster at CE / electrolyte boundary of the former indicating better regeneration of the oxidized triiodide species by $CuCo_2S_4$ catalyst. This property assisted the generation of higher J_{SC} by $CuCo_2S_4$ device.

Table 6. 6 Photovoltaic parameters of Pt and $CuCo_2S_4$ cells

Cells	Eff (%)	Voc (V)	Jsc (mA/cm^2)	FF
Pt	7.62±0.14	0.73±0.01	18.67±0.55	0.56±0.01
$CuCo_2S_4$	8.68±0.18	0.73±0.01	20.00±0.25	0.59±0.01

Table 6. 7 EIS parameters of Pt and $CuCo_2S_4$

Cells	R_S	R_{CT}	R_{TiO2}	Z_{DIFF}	CPE_1 ×E+05	CPE_2
Pt	24.57	32.91	61.88	6.97	1.64	0.0005
$CuCo_2S_4$	23.20	24.61	63.63	6.29	4.94	0.0005

6.3.4 Stability of $CuCo_2S_4$ device

The stability of the device with $CuCo_2S_4$ counter electrode was studied over 960 hours at ambient conditions periodically measuring photovoltaic parameters of the cell, see Fig.6.25. The result demonstrated that the catalyst is remarkably stable. The efficiency of the $CuCo_2S_4$ cell did not show any noticeable change within 10 days (240 h) of study. After the pass of 40 days (960 h) the PCE exhibited only minor decrease demonstrating excellent catalytic activity of the product as Pt-free counter electrode for dye-sensitized solar cells.

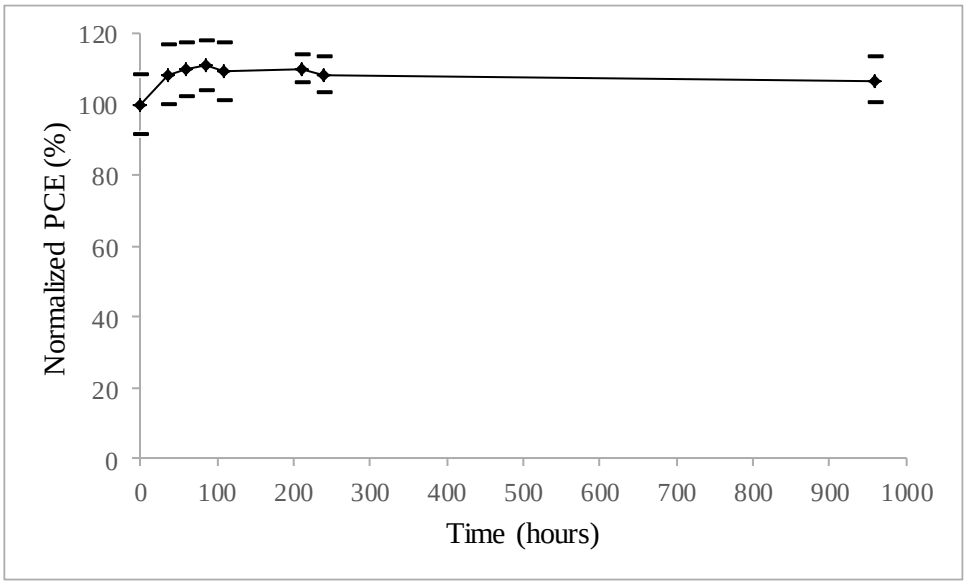

Figure 6. 25 Stability of $CuCo_2S_4$ solar cell

6.3.5 Summary of section 6.3

In this section flower shaped nanostructured $CuCo_2S_4$ was synthesized by solvothermal method. The content of the product was verified by EDX, XRD and Raman Spectroscopy. N_2 porosimetry analysis revealed unusually high surface area for $CuCo_2S_4$. Further characterization of the product by photovoltaic and electrochemical measurements demonstrated outstanding performance of $CuCo_2S_4$ as counter electrode for DSSC. It showed 8.68 % PCE, outperforming Pt (7.62 % PCE) for 14 % as a result of excellent catalytic activity in reducing triiodide.

Chapter 7

CONCLUSION AND FUTURE WORK

Sun delivers immense amount of energy to Earth. The use of this energy relies on its efficient conversion into electricity which in turn demands adequate technology. Silicon solar cells, being the most advanced type of photovoltaics, hardly compete with traditional fossil fuel based technology due to its high cost. Therefore the development of solar power necessitates low-cost competitive analogs of silicon photovoltaics. Dye-sensitized solar cells are considered potential alternative to Si-based PV owing to its lower price, ease of manufacturing and relatively high efficiency. The future development of DSSC technology requires improvement of its power converting efficiency and bringing down its cost. In our work we focused on the development of economical methods and components for dye-sensitized solar cells.

One of the problems encountered in DSSCs is electron recombination at photoanode / dye / electrolyte interface. Among many methods doping the photoanode is of high interest as it offers improvement of photovoltaic parameters. However, doping is achieved by bulk mixing of the impurity into TiO_2 lattice which necessitates strict control of concentration and reaction conditions. In Chapter 4 we proposed an easy and less expensive way of the modification of TiO_2 photoanode via surface doping. The method is based on post-treatment of the TiO_2 film with In^{3+} acidic solution followed by sintering which, if compared to pristine TiO_2, noticeably increases the charge recombination resistance of the photoanode and the photovoltage which leads to the increase of solar cell efficiency. The improvement of cell photovoltaic parameters is comparable with the results of bulk In doped TiO_2 sensitized solar cells.

In Chapter 5 we investigated the axial coordination of porphyrin dye with pyridine based ligands as a method of controlling dye aggregation. Dye aggregation is a serious problem which is addressed by adding costly components into the dye cocktail or attaching bulky groups into the dye structure which again adds to the cost. The proposed method allows the use of simple porphyrin structures free of bulky groups which in turn makes the preparation of porphyrin dyes less expensive.

Platinum is one of the most expensive and rare metals. Its use as counter electrode may threaten wide production of DSSCs. Moreover, Pt counter electrodes have stability related problems. In Chapter 6 we described the development of Pt-free counter electrodes for DSSC. Three alternatives were proposed as catalyst for reducing liquid triiodide electrolyte: orange fiber derived carbon embedded cobalt sulfide sintered at 300ºC (OFC@Co_xS_y-300), ternary transition metal sulfides $CuCo_{5.8}S_{11.5}$ and $CuCo_2S_4$. The obtained products exhibited higher efficiency than reference Pt CE based solar cells and demonstrated excellent stability.

Thus, modification of the TiO_2 photoanode via surface doping with indium caused about 18 % increase of the cell efficiency compared to undoped TiO_2 cell. The axial coordination of ZnP porphyrin with 4,4'-bipyridine ligand led to about 40 % improvement of PCE compared to uncoordinated ZnP cell due to suppressed aggregation of the porphyrin dye molecules. The solar cells made of newly developed Pt-free counter electrodes OFC@Co_xS_y-300, $Cu_xCo_yS_z$-3 ($CuCo_{5.8}S_{11.5}$) and $CuCo_2S_4$ exhibited about 7 %, 11 % and 14 % higher PCEs, respectively, compared to traditional Pt CE based DSSCs. If to compare all three results, In surface doping of TiO_2 photoanode could be considered the most effective method of enhancing cell efficiency which allows the highest V_{OC}, 0.8 V. If the same photovoltage (0.8 V) was obtained with the nanostructured $CuCo_2S_4$ CE based DSSC while keeping other cell parameters unchanged, the overall improvement of PCE would be by 25 %.

The novel counter electrode materials OFC@Co_xS_y-300, $Cu_xCo_yS_z$-3 and $CuCo_2S_4$ demonstrated excellent regeneration of triiodide species. However, their performance with Co-based redox media is unknown while Co-based electrolytes are considered better than iodide-based electrolyte in generating higher V_{OC}. If the developed catalysts can regenerate Co-based electrolyte efficiently, then cell efficiency can be even higher than with triiodide / iodide electrolyte. This hypothesis can be the task for future work.

We strongly believe the obtained experimental results are valuable to scientific community and can be continued to further improve the performance of dye-sensitized solar cells and bring down its cost for its commercialization. The following are the proposed and planned scope of future work in this direction:

- Surface doping of TiO_2 could be accomplished by other abundant elements which can shift the conduction band in negative direction. This is quite interesting in terms of further improvement of V_{OC}. Another approach of improving V_{OC} would be the use of cobalt based electrolytes with surface doped TiO_2 photoanode.
- The axial coordination of pyridine based ligands could be studied using porphyrin dyes with strong acceptor units that allow better charge transfer. We propose to use porphyrin sensitizer with benzothiadiazole unit as in the example of SM315 dye but without long alkyl groups.
- To further improve the stability of DSSCs the developed Pt-free counter electrodes can be applied with quasi-solid state and solid state electrolytes.

LIST OF REFERENCES

1. Bakhytzhan Baptayev, Salimgerey Adilov, Mannix P. Balanay. “Surface modification of TiO2 photoanodes with In3+ using a simple soaking technique for enhancing the efficiency of dye-sensitized solar cells”, Journal of Photochemistry & Photobiology A: Chemistry 394 (2020) 112468. DOI: 10.1016/j.jphotochem.2020.112468.
2. Bakhytzhan Baptayev, Sang Hee Lee, Dong Hee Kim, Mannix P.Balanay. “Controlling aggregation using self-assembled axially coordinated pyridine-based ligands on porphyrin analogues for dye-sensitized solar cells”, Chemical Physics Letters, 730 (2019) 407–410. DOI: 10.1016/j.cplett.2019.06.008.
3. B. Baptayev, A. Rysbekova, D. Kalpakov, A. Aukenova, D. Mustazheb, Z. Salkenova, M. Kazaliyev,, M. Balanay. “Control of porphyrin dye aggregation using bis(4-pyridyl)alkanes in dye sensitized solar cells”, Eurasian Chem. Tech. J., vol. 21, no. 1, pp. 63-67, Feb. 2019. DOI: 10.18321/ectj792.
4. Bakhytzhan Baptayev, Ainura Aukenova, Dias Mustazheb, MirasKazaliyev, Mannix P.Balanay. “Pt-free counter electrode based on orange fiber-derived carbon embedded cobalt sulfide nanoflakes for dye-sensitized solar cells”, Journal of Photochemistry & Photobiology A: Chemistry 383 (2019) 111977. DOI: 10.1016/j.jphotochem.2019.111977.
5. B. Baptayev, D. Mustazheb, M.P. Balanay. “Binary Transition Metal Sulfides as an Economical Pt-free Counter Electrodes for Dye-sensitized Solar Cells”, Materials Today: Proceedings, DOI: 10.1016/j.matpr.2019.10.170.
6. UN Dept Econ and Social Affairs. “World population projected to reach 9.8 billion in 2050, and 11.2 billion in 2100”. United Nations. https://www.un.org/development/desa/en/news/population/world-population-prospects-2017.html (accessed 03/Sep/2019)
7. Euan Mearns. “Global Energy Forecast to 2100”. EuanMearns. http://euanmearns.com/global-energy-forecast-to-2100/ (accessed 03/Sep/2019).
8. NASA Global Climate Change. “GLOBAL LAND-OCEAN TEMPERATURE INDEX”. NASA. https://climate.nasa.gov/vital-signs/global-temperature/ (accessed 03/Sep/2019).

9. Sims REH, Schock RN, Adegbululgbe A, Fenhann J, Konstantinaviciute I, Moomaw W, et al. Energy supply. In: Metz B, Davidson OR, Bosch PR, Dave R, Meyer LA, editors. *Climate change 2007: mitigation*. Cambridge, UK: CUP; 2007. p. 251–322.
10. Enerdata. “Global Energy Statistical Yearbook 2019”. Enerdata. https://yearbook.enerdata.net/total-energy/world-consumption-statistics.html (accessed 03/Sep/2019).
11. Ken Tomabechi, “Energy Resources in the Future,” *Energies*, 3, 686-695, 2010. doi:10.3390/en3040686.
12. Patrick Moriarty, Damon Honnery, “What is the global potential for renewable energy?,” *Renewable and Sustainable Energy Reviews*, 16, 244–252, 2012. doi:10.1016/j.rser.2011.07.151.
13. Richard E. Smalley. “Future Global Energy Prosperity: The Terawatt Challenge,” *MRS BULLETIN*, 30, 412 – 417, June 2005.
14. Ehsanul Kabir, Pawan Kumar, Sandeep Kumar, Adedeji A. Adelodun, Ki-Hyun Kim. “Solar energy: Potential and future prospects,” *Renewable and Sustainable Energy Reviews*, Vol.82, Part 1, Pg. 894-900, February 2018.
15. Avenston, “Changes in world energy are inevitable,” Avenston, https://avenston.com/en/articles/changes-in-energy-are-inevitable/ (accessed 04/Sep/2019).
16. EWS, “Energy economy,” Photovoltaics, https://www.pv.de/en/photovoltaics/market-development/energy-economy/ (accessed 04/Sep/2019).
17. Joseph Kalowekamo, Erin Baker. “Estimating the manufacturing cost of purely organic solar cells”, Solar Energy 83 (2009) 1224-1231. DOI: 10.1016/j.solener.2009.02.003.
18. A.E. Becquerel, "Recherches sur les effets de la radiation chimique de la lumiere solaire au moyen des courants electriques", Comptes Rendus de L'Academie des Sciences, Vol. 9, pp. 145-149, 1839; also Annalen der Physik und Chemie, Vol. 54, pp. 18-34, 1841.
19. A.E. Becquerel, "Memoire sur les effects electriques produits sous l'influence des rayons solaires", Comptes Rendus de L'Academie des Sciences, Vol. 9, pp. 561- 567, 1839; also Annalen der Physik und Chemie, Vol. 54, pp. 35-42, 1841.

20. Willoughby Smith. “Effect of Light on Selenium During the Passage of An Electric Current”, Nature, volume 7, page 303 (1873).
21. W.G. Adams, R.E. Day, The action of light on selenium. Proc R Soc A25, 113 (1877).
22. Hoang, Samantha, "The Environmental History of Solar Photovoltaic Cells" (2017). Student Library Research Awards. 24. http://repository.wellesley.edu/library_awards/24
23. Einstein, Albert. "Über einen die Erzeugung und Verwandlung des Lichtes betreffenden heuristischen Gesichtspunkt" [On a Heuristic Point of View about the Creation and Conversion of Light]. Annalen der Physik (in German). 17 (6): 132–148. (1905). doi:10.1002/andp.19053220607.
24. Millikan, R. "A Direct Determination of "h."". Physical Review. 4 (1): 73–75. (1914). doi:10.1103/PhysRev.4.73.2.
25. L. M. Fraas, Low-Cost Solar Electric Power, DOI: 10.1007/978-3-319-07530-3_1, Springer International Publishing Switzerland 2014.
26. William Shockley and Hans J. Queisser. “Detailed Balance Limit of Efficiency of p-n Junction Solar Cells”, Journal of Applied Physics 32, 510 (1961); DOI: 10.1063/1.1736034.
27. Martin A. Green. “Limiting photovoltaic efficiency under new ASTM International G173-based reference spectra”, Prog. Photovolt: Res. Appl. 20: 954–959; 2012, DOI: 10.1002/pip.1156.
28. PVEducation, “Atmospheric Effects”, Copyright 2019 PVeducation, https://www.pveducation.org/pvcdrom/properties-of-sunlight/%EB%8C%80%EA%B8%B0-%ED%9A%A8%EA%B3%BC-atmospheric-effects#footnote2_k836kfx (accessed 10/Sep/2019).
29. Fraunhofer Institute for Solar Energy Systems, ISE. “Photovoltaics report”, Fraunhofer, https://www.ise.fraunhofer.de/content/dam/ise/de/documents/publications/studies/Photovoltaics-Report.pdf (accessed on 11/Sep/2019).
30. T. Wang, “Record lab solar cell efficiency worldwide in 2017, by type”, Statista. https://www.statista.com/statistics/677062/efficiency-of-solar-cells-by-type/ (accessed on 11/Sep/2019).
31. Yifeng Chen et.al. “From Laboratory to Production: Learning Models of Efficiency and Manufacturing Cost of Industrial Crystalline Silicon and Thin-Film Photovoltaic Technologies”, IEEE Journal Of Photovoltaics,

Vol.8, Issue: 6, Pg.1531–1538, Nov. 2018. DOI: 10.1109/JPHOTOV.2018.2871858.

32. Breeze P., “Types of solar cells. Solar Power Generation”, 57-70, 2016. DOI: 10.1016/B978-0-12-804004-1.00009-9.
33. NREL, “Best Research-Cell Efficiency Chart”, NREL. https://www.nrel.gov/pv/cell-efficiency.html (accessed 11/Sep/2019).
34. Tinoco, T.; Rincón, C.; Quintero, M.; Pérez, G. Sánchez. "Phase Diagram and Optical Energy Gaps for $CuIn_yGa_{1-y}Se_2$ Alloys". Physica Status Solidi A. 124 (2): 427. 1991. Bibcode:1991PSSAR.124..427T. doi:10.1002/pssa.2211240206
35. Yiming Cao, Yuhang Liu, Shaik Mohammed Zakeeruddin, Anders Hagfeldt, and Michael Gra¨tzel. “Direct Contact of Selective Charge Extraction Layers Enables High-Efficiency Molecular Photovoltaics”, Joule 2, 1108–1117, June 20, 2018. Doi: 10.1016/j.joule.2018.03.017
36. O'Regan B, Grätzel M. A low-cost, high-efficiency solar cell based on dye-sensitized colloidal TiO2 films. Nature. 1991; 353 (6346): 737–740. doi: 10.1038/353737a0.
37. Udo BachYasuhiro TachibanaJacques-E. MoserSaif A. HaqueJames R. DurrantMichael GrätzelDavid R. Klug. “Charge Separation in Solid-State Dye-Sensitized Heterojunction Solar Cells” J. Am. Chem. Soc.1999, 121, 32, 7445-7446.
38. Michael Gratzel. “Solar Energy Conversion by Dye-Sensitized Photovoltaic Cells”, Inorg. Chem. 2005, 44, 6841−6851. Doi: 10.1021/ic0508371.
39. Ryuzi Katoha, Akihiro Furube. “Electron injection efficiency in dye-sensitized solar cells”, Journal of Photochemistry and Photobiology C: Photochemistry Reviews 20 (2014) 1–16. Doi: 10.1016/j.jphotochemrev.2014.02.001.
40. S. Y. Huang, G. Schlichtho, A. J. Nozik, M. Gra1tzel and A. J. Frank. “Charge Recombination in Dye-Sensitized Nanocrystalline TiO2 Solar Cells”, J. Phys. Chem. B 1997, 101, 2576-2582. Doi: 10.1021/jp962377q.
41. Iacopo Benesperi, Hannes Michaels and Marina Freitag. “The researcher’s guide to solid-state dye-sensitized solar cells”, J. Mater. Chem. C, 2018, 6, 11903. DOI: 10.1039/c8tc03542c.

42. Thomas W. Hamann, Rebecca A. Jensen, Alex B. F. Martinson, Hal Van Ryswyk and Joseph T. Hupp. “Advancing beyond current generation dye-sensitized solar cells”, Energy Environ. Sci., 2008, 1, 66–78. DOI: 10.1039/b809672d.
43. Chia-Yuan Chen, Mingkui Wang , Jheng-Ying Li, Nuttapol Pootrakulchote, Leila Alibabaei, Cevey-ha Ngoc-le , Jean-David Decoppet , Jia-Hung Tsai , Carole Grätzel , Chun-Guey Wu, Shaik M. Zakeeruddin and Michael Grätzel. “Highly Efficient Light-Harvesting Ruthenium Sensitizer for Thin-Film Dye-Sensitized Solar Cells”. ACS Nano, 2009, Vol.3 issue 10, pp 3103–3109. DOI: 10.1021/nn900756s.
44. Yella A, Lee HW, Tsao HN, Yi C, Chandiran AK, Nazeeruddin MK, Diau EW, Yeh CY, Zakeeruddin SM, Grätzel M. “Porphyrin-Sensitized Solar Cells with Cobalt (II/III)–Based Redox Electrolyte Exceed 12 Percent Efficiency”, Science. 2011-Nov 4; Vol.334, issue 6056, pp. 629-34. doi: 10.1126/science.1209688.
45. Simon Mathew, Aswani Yella, Peng Gao, Robin Humphry-Baker, Basile F. E. Curchod, Negar Ashari-Astani, Ivano Tavernelli, Ursula Rothlisberger, Md. Khaja Nazeeruddin & Michael Grätzel. “Dye-sensitized solar cells with 13% efficiency achieved through the molecular engineering of porphyrin sensitizers”, Nature Chemistry vol.6, pages 242–247 (2014). Doi: 10.1038/nchem.1861.
46. Kenji Kakiage, Yohei Aoyama, Toru Yano, Keiji Oya, Jun-ichi Fujisawa and Minoru Hanaya. “Highly-efficient dye-sensitized solar cells with collaborative sensitization by silyl-anchor and carboxy-anchor dyes”, Chem. Commun., 2015, 51, 15894. DOI: 10.1039/c5cc06759f.
47. Takuya Kawashima, Tetsuya Ezure, Kenichi Okada, Hiroshi Matsui, Kenji Goto, Nobuo Tanabe. “FTO/ITO double-layered transparent conductive oxide for dye-sensitized solar cells”, Journal of Photochemistry and Photobiology A: Chemistry 164 (2004) 199–202. doi:10.1016/j.jphotochem.2003.12.028.
48. Cornelia Sima, Constantin Grigoriu, Stefan Antohe. “Comparison of the dye-sensitized solar cells performances based on transparent conductive ITO and FTO”, Thin Solid Films 519 (2010) 595–597. doi:10.1016/j.tsf.2010.07.002.

49. M. K. NazeeruddinA. KayI. RodicioR. Humphry-BakerE. MuellerP. LiskaN. VlachopoulosM. Graetzel. “Conversion of light to electricity by cis-X2bis(2,2'-bipyridyl-4,4'-dicarboxylate)ruthenium(II) charge-transfer sensitizers (X = Cl-, Br-, I-, CN-, and SCN-) on nanocrystalline titanium dioxide electrodes”, J. Am. Chem. Soc., Vol. 115, No. 14, 1993. doi: 10.1021/ja00067a063.
50. Michael Grätzel. “Photoelectrochemical cells”, Nature volume 414, pages 338–344 (2001). doi: 10.1038/35104607.
51. Muhammad Shakeel Ahmad, A.K. Pandey, Nasrudin Abd Rahim. “Advancements in the development of TiO2 photoanodes and its fabrication methods for dye sensitized solar cell (DSSC) applications. A review”, Renewable and Sustainable Energy Reviews 77 (2017) 89–108. doi: 10.1016/j.rser.2017.03.129.
52. R. Vittal, Kuo-Chuan Ho. “Zinc oxide based dye-sensitized solar cells: A review”, Renewable and Sustainable Energy Reviews 70 (2017) 920–935, doi: 10.1016/j.rser.2016.11.273.
53. Qamar Wali, Azhar Fakharuddin, Rajan Jose. “Tin oxide as a photoanode for dye-sensitised solar cells: Current progress and future challenges”, Journal of Power Sources 293 (2015) 1039-1052. doi: 10.1016/j.jpowsour.2015.06.037.
54. A. Le Viet, R. Jose, M. V. Reddy, B. V. R. Chowdari† and S. Ramakrishna. “Nb2O5 Photoelectrodes for Dye-Sensitized Solar Cells: Choice of the Polymorph”, J. Phys. Chem. C 2010, 114, 21795–21800. doi: 10.1021/jp106515k.
55. Nurnaeimah Jamalullail, Ili Salwani Mohamad, Mohd Natashah Norizan, Norsuria Mahmed, and Bibi Nadia Taib. “Recent improvements on TiO2 and ZnO nanostructure photoanode for dye sensitized solar cells: A brief review”, EPJ Web of Conferences 162, 01045 (2017). DOI: 10.1051/epjconf/201716201045.
56. Zhang J, Zhou P, Liu J, Yu J. “New understanding of the difference of photocatalytic activity among anatase, rutile and brookite TiO2”, Physical Chemistry Chemical Physics 2014; 16 (38): 20382–20386. doi: 10.1039/C4CP02201G.

57. N.-G. Park, J. van de Lagemaat, and A. J. Frank. “Comparison of Dye-Sensitized Rutile- and Anatase-Based TiO2 Solar Cells”, J. Phys. Chem. B, Vol. 104, No. 38, 2000. doi: 10.1021/jp994365l.
58. D. Pourjafari, D. Reyes-Coronado, A. Vega-Poot, R. Escalante, D. Kirkconnell-Reyes, R. García-Rodríguez, J. A. Anta and G. Oskam. “Brookite-Based Dye-Sensitized Solar Cells: Influence of Morphology and Surface Chemistry on Cell Performance”, J. Phys. Chem. C 2018, 122, 14277−14288. DOI: 10.1021/acs.jpcc.8b02384.
59. R. Hattori and H. Goto, “Carrier leakage blocking effect of high temperature sputtered TiO2 film on dye-sensitized mesoporous photoelectrode,” Thin Solid Films, vol. 515, no. 20-21, pp. 8045–8049, 2007. doi: 10.1016/j.tsf.2007.03.079.
60. Hua Yu, Shanqing Zhang, Huijun Zhaoa, Geoffrey Will, Porun Liu. “An efficient and low-cost TiO2 compact layer for performance improvement of dye-sensitized solar cells”, Electrochimica Acta 54 (2009) 1319–1324. doi:10.1016/j.electacta.2008.09.025.
61. S.-J. Roh, R. S. Mane, S.-K. Min, W.-J. Lee, C. D. Lokhande, and S.-H. Han, “Achievement of 4.51% conversion efficiency using ZnO recombination barrier layer in TiO2 based dyesensitized solar cells,” Applied Physics Letters, vol. 89, no. 25, Article ID 253512, 2006. DOI: 10.1063/1.2410240.
62. Seok-Min Yong, Nikolay Tsvetkov, Liudmila Larina, Byung Tae Ahn, Do Kyung Kim. “Ultrathin SnO2 layer for efficient carrier collection in dye-sensitized solar cells”, Thin Solid Films 556 (2014) 503–508. doi: 10.1016/j.tsf.2014.01.008.
63. J. Xia, N. Masaki, K. Jiang, and S. Yanagida, “Sputtered Nb2O5 as a novel blocking layer at conducting glass/TiO2 interfaces in dye-sensitized ionic liquid solar cells,” Journal of Physical Chemistry C, vol. 111, no. 22, pp. 8092–8097, 2007. doi: 10.1021/jp0707384.
64. Anthony Burke, Seigo Ito, Henry Snaith, Udo Bach, Joe Kwiatkowski and Michael Grätzel. “The Function of a TiO2 Compact Layer in Dye-Sensitized Solar Cells Incorporating “Planar” Organic Dyes”, Nano Lett., Vol. 8, No. 4, 2008, 977-981. doi: 10.1021/nl071588b.
65. Seigo Ito, Paul Liska, Pascal Comte, Raphae¨l Charvet, Peter Pe´chy, Udo Bach, Lukas Schmidt-Mende, Shaik Mohammed Zakeeruddin,

Andreas Kay, Mohammad K. Nazeeruddin and Michael Gra¨tzel. “Control of dark current in photoelectrochemical (TiO2/I2–I32) and dye-sensitized solar cells”, Chem. Commun., 2005, 4351–4353. DOI: 10.1039/b505718c.

66. Tae Sung Eom, Kyung Hwan Kim, Chung Wung Bark, and Hyung Wook Choi. “Influence of TiCl4 Post-Treatment Condition on TiO2 Electrode for Enhancement Photovoltaic Efficiency of Dye-Sensitized Solar Cells”, Journal of Nanoscience and Nanotechnology Vol. 14, 7705–7709, 2014. doi:10.1166/jnn.2014.9449.
67. P.M. Sommeling, B.C. O’Regan, R.R. Haswell, H.J.P. Smit, N.J. Bakker, J.J.T. Smits, J.M. Kroon and J.A.M. van Roosmalen. “Influence of a TiCl4 Post-Treatment on Nanocrystalline TiO2 Films in Dye-Sensitized Solar Cells”, J. Phys. Chem. B 2006, 110, 19191-19197. doi: 10.1021/jp061346k.
68. Arman Sedghi and Hoda Nourmohammadi Miankushki. “Influence of TiCl4 Treatment on Structure and Performance of Dye-Sensitized Solar Cells”, Japanese Journal of Applied Physics 52 (2013) 075002. doi:10.7567/JJAP.52.075002.
69. Seigo Ito, Mohammad K. Nazeeruddin, Shaik M. Zakeeruddin, Peter Pechy, Pascal Comte, Michael Gratzel, Takaki Mizuno, Atsushi Tanaka and Tsuguo Koyanagi. “Study of Dye-Sensitized Solar Cells by Scanning Electron Micrograph Observation and Thickness Optimization of Porous TiO2 Electrodes”, Int. J. of Photoenergy, V.2009, Article ID 517609, 8 pages, doi:10.1155/2009/517609.
70. Zhipan Zhang, Seigo Ito, Brian O’Regan, Daibin Kuang, Shaik Mohammed Zakeeruddin, Paul Liska, Raphaël Charvet, Pascal Comte, Mohammad Khaja Nazeeruddin, Peter Pechy, Robin Humphry-Baker, Tsuguo Koyanagi, Takaki Mizuno and Michael Grätzel. “The Electronic Role of the TiO2 Light-Scattering Layer in Dye-Sensitized Solar Cells”, Z. Phys. Chem. 221 (2007) 319–327; DOI 10.1524/zpch.2007.221.3.319.
71. Min-Kyu Son, Hyunwoong Seo, Soo-Kyoung Kim, Na-Yeong Hong, Byung-Man Kim, Songyi Park, Kandasamy Prabakar and Hee-Je Kim. “Analysis on the Light-Scattering Effect in Dye-Sensitized Solar Cell according to the TiO2 Structural Differences”, Int. J. of Photoenergy, V.2012, Article ID 480929, 8 pages. doi:10.1155/2012/480929.

72. Zhang Zhe, Zhou Baoxue, Ge Weijie, Xiong Bitao, Zheng Qing & Cai Weimin. “Charge recombination in dye-sensitized nanoporous TiO2 solar cell”, Chinese Science Bulletin 2005 Vol. 50 No. 21 2408—2412. DOI: 10.1360/982005-42.
73. Nafiseh Memarian Isabella Concina Antonio Braga Seyed Mohammad Rozati Alberto Vomiero Giorgio Sberveglieri. “Hierarchically Assembled ZnO Nanocrystallites for High-Efficiency Dye-Sensitized Solar Cells”, Angew Chem Int Ed 2011; 50 (51):12321–5. doi: 10.1002/anie.201104605.
74. Marıa Quintana, Tomas Edvinsson, Anders Hagfeldt and Gerrit Boschloo. “Comparison of Dye-Sensitized ZnO and TiO2 Solar Cells: Studies of Charge Transport and Carrier Lifetime”, J. Phys. Chem. C 2007, 111, 1035-1041. doi: 10.1021/jp065948f.
75. Karin Keis, Jan Lindgren, Sten-Eric Lindquist, and Anders Hagfeldt. “Studies of the Adsorption Process of Ru Complexes in Nanoporous ZnO Electrodes”, Langmuir 2000, 16, 4688-4694. doi: 10.1021/la9912702.
76. Shin YJ, Lee JH, Park JH, Park NG. “Enhanced Photovoltaic Properties of SiO2-treated ZnO Nanocrystalline Electrode for Dye-sensitized Solar Cell”, Chem Lett. 2007; 36(12):1506–7. doi:10.1246/cl.2007.1506.
77. Shin YJ, Kim KS, Park NG, Ryu KS, Chang SH. “Enhancement of photovoltaic properties of Ti-modified nanocrystalline ZnO electrode for dye-sensitized solar cell”, Bull Korean Chem Soc 2005;26(12):1929–30.
78. Zhengdao Li, Yong Zhou, Ruzhong Sun, Yan Xiong, Haiquan Xie, Zhigang Zou. “Nanostructured SnO2 photoanode-based dye-sensitized solar cells”, Chin. Sci. Bull. (2014) 59(18):2122–2134. DOI: 10.1007/s11434-013-0079-3.
79. Zhenghong Dong Hao Ren Colin M. Hessel Jiangyan Wang Ranbo Yu Quan Jin Mei Yang Zhudong Hu Yunfa Chen Zhiyong Tang Huijun Zhao Dan Wang. “Quintuple-Shelled SnO2 Hollow Microspheres with Superior Light Scattering for High-Performance Dye-Sensitized Solar Cells”, Adv.Mater.2014, 26, 905–909. DOI: 10.1002/adma.201304010.
80. Ming Liu, Junyou Yang, Shuanglong Feng, Hu Zhu, Jiansheng Zhang, Gen Li, Jiangying Peng. “Composite photoanodes of Zn2SnO4 nanoparticles modified SnO2 hierarchical microspheres for dye-sensitized

solar cells", Materials Letters 76 (2012) 215–218. doi: 10.1016/j.matlet.2012.02.110.

81. Haidong Zheng, Yasuhiro Tachibana and Kourosh Kalantar-zadeh. "Dye-Sensitized Solar Cells Based on WO3", Langmuir 2010, 26(24), 19148–19152. DOI: 10.1021/la103692y.
82. D.W. Kim, S.S. Shin, I.S. Cho, S. Lee, D.H. Kim, C.W. Lee, H.S. Jung, K.S. Hong. "Synthesis and photovoltaic property of fine and uniform Zn2SnO4 nanoparticles", Nanoscale 2012, 4, 557. DOI: 10.1039/C1NR11063B.
83. Dong Wook Kim, Seong Sik Shin, Sangwook Lee, In Sun Cho, Dong Hoe Kim, Chan Woo Lee, Hyun Suk Jung and Kug Sun Hong. "BaSnO3 Perovskite Nanoparticles for High Efficiency DyeSensitized Solar Cells", ChemSusChem 2013, 6, 449 – 454. DOI: 10.1002/cssc.201200769.
84. Sousan Gholamrezaei, Masoud Salavati-Niasari. "An efficient dye sensitized solar cells based on SrTiO3 nanoparticles prepared from a new amine-modified sol-gel route", Journal of Molecular Liquids 243 (2017) 227–235. doi: 10.1016/j.molliq.2017.08.031.
85. Wu-Qiang Wu, Yang-Fan Xu, Cheng-Yong Su and Dai-Bin Kuang. "Ultra-long anatase TiO2 nanowire arrays with multi-layered configuration on FTO glass for high-efficiency dye-sensitized solar cells", Energy Environ. Sci., 2014, 7, 644. DOI: 10.1039/c3ee42167h.
86. Wu-Qiang Wu, Bing-Xin Lei, Hua-Shang Rao, Yang-Fan Xu, Yu-Fen Wang, Cheng-Yong Su & Dai-Bin Kuang. "Hydrothermal Fabrication of Hierarchically Anatase TiO2 Nanowire arrays on FTO Glass for Dye-sensitized Solar Cells", Scientific Reports volume3, Article number: 1352 (2013). DOI: 10.1038/srep01352.
87. Carmen Cavallo, Francesco Di Pascasio, Alessandro Latini, Matteo Bonomo, and Danilo Dini. "Nanostructured Semiconductor Materials for Dye-Sensitized Solar Cells", Journal of Nanomaterials, V. 2017, Article ID 5323164, 31 pages, doi:10.1155/2017/5323164.
88. Martinson ABF, Mc Garrah JE, Parpia MOK, Hupp JT. "Dynamics of charge transport and recombination in ZnO nanorod array dye-sensitized solar cells", Phys Chem Chem Phys 2006; 8: 4655–9. DOI: 10.1039/b610566a.

89. M. Law, L. E. Greene, J. C. Johnson, R. Saykally, and P. Yang, “Nanowire dye-sensitized solar cells,” Nature Materials, vol. 4, no. 6, pp. 455–459, 2005. doi:10.1038/nmat1387.
90. Myrsini Giannouli, Katerina Govatsi, George Syrrokostas, Spyros N. Yannopoulos and George Leftheriotis. “Factors Affecting the Power Conversion Efficiency in ZnO DSSCs: Nanowire vs. Nanoparticles”, Materials 2018, 11, 411; doi:10.3390/ma11030411.
91. Alex B. F. MartinsonJeffrey W. ElamJoseph T. HuppMichael J. Pellin. “ZnO Nanotube Based Dye-Sensitized Solar Cells”, Nano Lett. 2007, 7, 8, 2183-2187. doi: 10.1021/nl070160+.
92. R. Ranjusha, P. Lekha, K.R.V. Subramanian, V. Nair Shantikumar, A. Balakrishnan. “Photoanode Activity of ZnO Nanotube Based Dye-Sensitized Solar Cells”, J.of Mat.Sci. & Tech., V.27, Iss.11, November 2011, Pages 961-966. doi: 10.1016/S1005-0302(11)60170-9.
93. Rangga Winantyo, Kenji Murakami. “ZnO nanorods formation for dye-sensitized solar cells applications”, Int. J. of Tech. (2017) 8: 1462-1469. doi: 10.14716/ijtech.v8i8.733.
94. Wei Chen and Shihe Yang. “Dye-sensitized solar cells based on ZnO nanotetrapods”, Front. Optoelectron. China 2011, 4(1): 24–44. DOI 10.1007/s12200-011-0207-0.
95. Suresh Gubbala, Harry B. Russell, Hemant Shah, Biswapriya Deb, Jacek Jasinski, Heather Rypkema and Mahendra K. Sunkara. “Surface properties of SnO2 nanowires for enhanced performance with dye-sensitized solar cells”, Energy Environ. Sci., 2009, 2, 1302–1309. DOI: 10.1039/b910174h.
96. Junchao Huo, Yanjie Hu, Hao Jiang, Wenjuan Huang and Chunzhong Li. “SnO2 nanorod@TiO2 hybrid material for dye sensitized solar cells”, J. Mater. Chem. A, 2014, 2, 8266. DOI: 10.1039/c4ta00083h.
97. Md. K. Nazeeruddin, P. Pechy and M. Gr ´ atzel. “Efficient panchromatic sensitization of nanocrystalline TiO2 films by a black dye based on a trithiocyanato–ruthenium complex”, Chem. Commun. 1997, 1705. DOI: 10.1039/A703277C.
98. Mohammad K. Nazeeruddin, Filippo De Angelis, Simona Fantacci, Annabella Selloni, Guido Viscardi, Paul Liska, Seigo Ito, Bessho Takeru, and Michael Gra¨tzel. “Combined Experimental and DFT-TDDFT

Computational Study of Photoelectrochemical Cell Ruthenium Sensitizers", J. AM. CHEM. SOC. 2005, 127, 16835-16847 9. DOI: 10.1021/ja052467l.

99. K. Kalyanasundaram, N. Vlachopoulos, V. Krishnan, A. Monnier, and M. Grátzel. "Sensitization of TiO2 in the Visible Light Region Using Zinc Porphyrins", J. Phys. Chem., 1987, 91, 2342–2347. DOI: 10.1021/j100293a027.

100. Andreas Kay and Michael Graetzel. "Artificial photosynthesis. 1. Photosensitization of titania solar cells with chlorophyll derivatives and related natural porphyrins", J. Phys. Chem.1993, 97, 23, 6272-6277. DOI: 10.1021/j100125a029.

101. Lingamallu Giribabu and Ravi Kumar Kanaparthi. "Are porphyrins an alternative to ruthenium(II) sensitizers for dye-sensitized solar cells?", Current Science, Vol. 104, No. 7, 10 April 2013.

102. Q. Wang, W. M. Campbell, E. E. Bonfantani, K. W. Jolley, D. L. Officer, P. J. Walsh, K. Gordon, R. Humphry-Baker, M. K. Nazeeruddin and M. Grätzel. "Efficient Light Harvesting by Using Green Zn-Porphyrin-Sensitized Nanocrystalline TiO2 Films", J. Phys. Chem. B, 2005, 109, 15397–15409. DOI: 10.1021/jp052877w.

103. W. M. Campbell, K. W. Jolley, P. Wagner, K. Wagner, P. J. Walsh, K. C. Gordon, L. Schmidt-Mende, M. K. Nazeeruddin, Q. Wang, M. Grätzel and D. L. Officer. "Highly Efficient Porphyrin Sensitizers for Dye-Sensitized Solar Cells", J. Phys. Chem. C, 2007, 111, 11760–11762. DOI: 10.1021/jp0750598.

104. Hsueh-Pei Lu, Chen-Yuan Tsai, Wei-Nan Yen, Chou-Pou Hsieh, Cheng-Wei Lee, Chen-Yu Yeh and Eric Wei-Guang Diau. "Control of Dye Aggregation and Electron Injection for Highly Efficient Porphyrin Sensitizers Adsorbed on Semiconductor Films with Varying Ratios of Coadsorbate", J. Phys. Chem. C 2009, 113, 20990–20997. DOI: 10.1021/jp908100v.

105. Takeru Bessho, Shaik M. Zakeeruddin, Chen-Yu Yeh, Eric Wei-Guang Diau, and Michael Gratzel. "Highly Efficient Mesoscopic Dye-Sensitized Solar Cells Based on Donor–Acceptor-Substituted Porphyrins", Angew. Chem. Int. Ed. 2010, 49, 6646 –6649. DOI: 10.1002/anie.201002118.

106. Sandra M. Feldt, Elizabeth A. Gibson, Erik Gabrielsson, Licheng Sun, Gerrit Boschloo and Anders Hagfeldt. “Design of Organic Dyes and Cobalt Polypyridine Redox Mediators for High-Efficiency Dye-Sensitized Solar Cells”, J. AM. CHEM. SOC. 2010, 132, 16714–16724. DOI: 10.1021/ja1088869.

107. Maxence Urbani, Michael Grätzel, Mohammad Khaja Nazeeruddin and Tomás Torres. “Meso-Substituted Porphyrins for Dye-Sensitized Solar Cells”, Chem. Rev. 2014, 114, 12330−12396. DOI: 10.1021/cr5001964.

108. Yella A, Mai CL, Zakeeruddin SM, Chang SN, Hsieh CH, Yeh CY, Grätzel M. “Molecular engineering of push-pull porphyrin dyes for highly efficient dye-sensitized solar cells: the role of benzene spacers”, Angew Chem Int Ed Engl. 2014 Mar 10; 53 (11): 2973-7. doi: 10.1002/anie.201309343.

109. Tomohiro Higashino and Hiroshi Imahori. “Porphyrins as excellent dyes for dye-sensitized solar cells: recent developments and insights”, Dalton Trans., 2015, 44, 448. DOI: 10.1039/c4dt02756f.

110. Maxence Urbani, Maria-Eleni Ragoussi, Mohammad Khaja Nazeeruddin, Tomás Torres. “Phthalocyanines for dye-sensitized solar cells”, Coordination Chemistry Reviews 381 (2019) 1–64. DOI: 10.1016/j.ccr.2018.10.007.

111. Cid JJ1, Yum JH, Jang SR, Nazeeruddin MK, Martínez-Ferrero E, Palomares E, Ko J, Grätzel M, Torres T. “Molecular cosensitization for efficient panchromatic dye-sensitized solar cells”, Angew Chem Int Ed Engl. 2007;46(44):8358-62. DOI: 10.1002/anie.200703106.

112. Mutsumi Kimura, Hirotaka Nomoto, Naruhiko Masaki, Shogo Mori. “Dye Molecules for Simple Co-Sensitization Process: Fabrication of Mixed-Dye-Sensitized Solar Cells”, Angew. Chem. Int. Ed.2012,51, 4371 –4374. DOI: 10.1002/anie.201108610.

113. Lijuan Yu, Ke Fan, Tainan Duan, Xingguo Chen, Renjie Li and Tianyou Peng. “Efficient Panchromatic Light Harvesting with Co-Sensitization of Zinc Phthalocyanine and Bithiophene-Based Organic Dye for DyeSensitized Solar Cells”, ACS Sustainable Chem. Eng. 2014, 2, 718−725. DOI: 10.1021/sc400532g.

114. Maria-Eleni Ragoussi, Jun-Ho Yum, Aravind Kumar Chandiran, Mine Ince, Gema de la Torre, Michael Gratzel, Mohammad K. Nazeeruddin and Toms Torres. “Sterically Hindered Phthalocyanines for Dye-Sensitized Solar Cells: Influence of the Distance between the Aromatic Core and the Anchoring Group”, ChemPhysChem 2014, 15, 1033 – 1036. DOI: 10.1002/cphc.201301118.

115. Takuro Ikeuchi, Hirotaka Nomoto, Naruhiko Masaki, Matthew J. Griffith, Shogo Mori and Mutsumi Kimura. “Molecular engineering of zinc phthalocyanine sensitizers for efficient dye-sensitized solar cells”, Chem. Commun., 2014, 50, 1941. DOI: 10.1039/c3cc47714b.

116. Takuro Ikeuchi, Saurabh Agrawal, Masayuki Ezoe, Shogo Mori and Mutsumi Kimura. “Enhanced Charge Separation Efficiency in Pyridine-Anchored Phthalocyanine-Sensitized Solar Cells by Linker Elongation”, Chem. Asian J. 2015, 10, 2347 – 2351. DOI: 10.1002/asia.201500756.

117. P.Y. Reddy, L. Giribabu, C. Lyness, H.J. Snaith, C. Vijaykumar, M. Chandrasekharam, M. Lakshmikantam, J.-H. Yum, K. Kalyanasundaram, M. Grätzel, M.K. Nazeeruddin. “Efficient sensitization of nanocrystalline TiO2 films by a near-IR-absorbing unsymmetrical zinc phthalocyanine”, Angew. Chem., Int. Ed. 46 (2007) 373–376. DOI: 10.1002/anie.200603098.

118. Qu SanYin, Hua JianLi & Tian He. “New D-π-A dyes for efficient dye-sensitized solar cells”, Sci China Chem May (2012) Vol.55 No.5. 677–697. doi: 10.1007/s11426-012-4517-x.

119. Takayuki Kitamura, Masaaki Ikeda, Koichiro Shigaki, Teruhisa Inoue, Neil A. Anderson, Xin Ai, Tianquan Lian and Shozo Yanagida. “Phenyl-Conjugated Oligoene Sensitizers for TiO2 Solar Cells”, Chem. Mater. 2004, 16, 1806-1812. DOI: 10.1021/cm0349708.

120. Marappan Velusamy, K. R. Justin Thomas, Jiann T. Lin, Ying-Chan Hsu and Kuo-Chuan Ho. “Organic Dyes Incorporating Low-Band-Gap Chromophores for Dye-Sensitized Solar Cells”, Org. Lett., Vol. 7, No. 10, 2005. DOI: 10.1021/ol050417f.

121. Zheng-Ming Tang, Ting Lei, Ke-Jian Jiang, Yan-Lin Song and Jian Pei. “Benzothiadiazole Containing D-p-A Conjugated Compounds for DyeSensitized Solar Cells: Synthesis, Properties, and Photovoltaic

Performances", Chem. Asian J. 2010, 5, 1911 – 1917. DOI: 10.1002/asia.201000158.

122. Dong Hyun Lee, Myung Jun Lee, Hae Min Song, Bok Joo Song, Kang Deuk Seo, Mariachiara Pastore, Chiara Anselmi, Simona Fantacci, Filippo De Angelis, Mohammad K. Nazeeruddin, Michael Gräetzel, Hwan Kyu Kim. "Organic dyes incorporating low-band-gap chromophores based on p-extended benzothiadiazole for dye-sensitized solar cells", Dyes and Pigments 91 (2011) 192-198. doi:10.1016/j.dyepig.2011.03.015.

123. Mesude Zeliha Yigit, Hakan Bilgili, Emre Sefer, Serafettin Demic, Ceylan Zafer, Mustafa Can, Sermet Koyuncu. "Effect of a pi-bridging unit in triphenylamine-benzothiadiazole based donor acceptor chromophores for dye-sensitized solar cells", Electrochimica Acta 147, (2014), 617–625. DOI: 10.1016/j.electacta.2014.09.138.

124. Hao Qin, Sophie Wenger, Mingfei Xu, Feifei Gao, Xiaoyan Jing, Peng Wang, Shaik M. Zakeeruddin and Michael Gratzel. "An Organic Sensitizer with a Fused Dithienothiophene Unit for Efficient and Stable Dye-Sensitized Solar Cells", J. Am. Chem. Soc. 2008, 130, 9202–9203. DOI: 10.1021/ja8024438.

125. Guangliang Zhang, Hari Bala, Yueming Cheng, Dong Shi, Xueju Lv, Qingjiang Yu and Peng Wang. "High efficiency and stable dye-sensitized solar cells with an organic chromophore featuring a binary p-conjugated spacer", Chem. Commun., 2009, 2198–2200. DOI: 10.1039/b822325d.

126. Wangdong Zeng, Yiming Cao, Yu Bai, Yinghui Wang, Yushuai Shi, Min Zhang, Fangfang Wang, Chunyue Pan and Peng Wang. "Efficient Dye-Sensitized Solar Cells with an Organic Photosensitizer Featuring Orderly Conjugated Ethylenedioxythiophene and Dithienosilole Blocks", Chem. Mater. 2010, 22, 1915–1925 1915. DOI:10.1021/cm9036988.

127. Xing Qian, Yi-Zhou Zhu, Jian Song, Xue-Ping Gao and Jian-Yu Zheng. "New Donor-π-Acceptor Type Triazatruxene Derivatives for Highly Efficient Dye-Sensitized Solar Cells", Org. Lett., Vol. 15, No. 23, 2013. DOI: 10.1021/ol402931u.

128. Bin Pan, Yi-Zhou Zhu, Dan Ye, Feng Li, Yi-Fan Guo and Jian-Yu Zheng. "Effects of ethynyl unit and electron acceptors on the performance

of triazatruxene-based dye-sensitized solar cells", NewJ.Chem., 2018, 42, 4133. DOI: 10.1039/c7nj04629d.

129. Li Zhang, Xichuan Yang, Weihan Wang, Gagik G. Gurzadyan, Jiajia Li, Xiaoxin Li,Jincheng An, Ze Yu, Haoxin Wang, Bin Cai, Anders Hagfeldt and Licheng Sun. "13.6% Efficient Organic Dye-Sensitized Solar Cells by Minimizing Energy Losses of the Excited State", ACS Energy Lett. 2019, 4, 943−951. DOI: 10.1021/acsenergylett.9b00141.

130. Nansra Heo, Yongseok Jun & Jong Hyeok Park. "Dye molecules in electrolytes: new approach for suppression of dye-desorption in dye-sensitized solar cells", Scientific Reports. 3: 1712. DOI: 10.1038/srep01712.

131. Seigo Ito, Md. Khaja Nazeeruddin, Paul Liska, Pascal Comte, Raphaël Charvet, Péter Péchy, Marie Jirousek, Andreas Kay, Shaik M. Zakeeruddin, Michael Grätzel. "Photovoltaic characterization of dye-sensitized solar cells: effect of device masking on conversion efficiency", Prog. Photovolt: Res. Appl. 2006; 14: 589–601. DOI: 10.1002/pip.683.

132. Chengcheng Xi, Yiming Cao, Yueming Cheng, Mingkui Wang, Xiaoyan Jing, Shaik M. Zakeeruddin, Michael Grätzel, Peng Wang. "Tetrahydrothiophenium-Based Ionic Liquids for High Efficiency Dye-Sensitized Solar Cells", J. Phys. Chem. C. 2008, 112, 29, 11063-11067. DOI: 10.1021/jp802798k.

133. Minna Toivola, Fredrik Ahlskog, Peter Lund. "Industrial sheet metals for nanocrystalline dye-sensitized solar cell structures", Solar Energy Materials & Solar Cells 90 (2006) 2881–2893. doi: 10.1016/j.solmat.2006.05.002.

134. Wang, M.; Gratzel, C.; Zakeeruddin, S. M.; Gratzel, M. "Recent developments in redox electrolytes for dye-sensitized solar cells", Energy Environ. Sci. 2012, 5, 9394. DOI:10.1039/C2EE23081J.

135. Marcus, R. "On the Theory of Oxidation-Reduction Reactions Involving Electron Transfer. I", J. Chem. Phys. 1956, 24, 966. DOI: 10.1063/1.1742723.

136. Teng, C., Yang, X., Yuan, C., Li, C., Chen, R., Tian, H., Li, S., Hagfeldt, A., Sun, L. "Two novel carbazole dyes for dye-sensitized solar cells with open-circuit voltages up to 1 V based on Br(-)/Br(3)(-) electrolytes", Org. Lett. 2009, 11, 5542. DOI: 10.1021/ol9022936.

137. Wang, P., Zakeeruddin, S., Moser, J., Baker, R., Gratzel, M. “A Solvent-Free, SeCN-/(SeCN)3- Based Ionic Liquid Electrolyte for High-Efficiency Dye-Sensitized Nanocrystalline Solar Cells”, J. Am. Chem. Soc. 2004, 126, 7164. DOI: 10.1021/ja048472r.

138. Nusbaumer, H., Moser, J., Zakeeruddin, S., Nazeeruddin, M., Gratzel, M. “$Co^{II}(dbbip)_2^{2+}$ Complex Rivals Tri-iodide/Iodide Redox Mediator in Dye-Sensitized Photovoltaic Cells”, J. Phys. Chem. B 2001, 105, 10461. DOI: 10.1021/jp012075a.

139. Schlichthorl, G., Huang, S., Sprague, J., Frank, A. “Band Edge Movement and Recombination Kinetics in Dye-Sensitized Nanocrystalline TiO2 Solar Cells: A Study by Intensity Modulated Photovoltage Spectroscopy”, J. Phys. Chem. B 1997, 101, 8141. DOI: 10.1021/jp9714126.

140. Boschloo, G., Haggman, L., Hagfeldt, A. “Quantification of the Effect of 4-tert-Butylpyridine Addition to I-/I3- Redox Electrolytes in Dye-Sensitized Nanostructured TiO2 Solar Cells”, J. Phys. Chem. B 2006, 110, 13144. DOI: 10.1021/jp0619641.

141. Jennings, J., Wang, Q. “Influence of Lithium Ion Concentration on Electron Injection, Transport, and Recombination in Dye-Sensitized Solar Cells”, J. Phys. Chem. C 2010, 114, 1715. DOI: 10.1021/jp9104129.

142. Koops, S., O’Regan, B., Barnes, P., Durrant, J. “Parameters Influencing the Efficiency of Electron Injection in Dye-Sensitized Solar Cells”, J. Am. Chem. Soc. 2009, 131, 4808. DOI: 10.1021/ja8091278.

143. Zhang, C., Huang, Y., Huo, Z., Chen, S., Dai, S. “Photoelectrochemical Effects of Guanidinium Thiocyanate on Dye-Sensitized Solar Cell Performance and Stability”, J. Phys. Chem. C 2009, 113, 21779. DOI: 10.1021/jp909732f.

144. Gratzel, M. “Conversion of Sunlight to Electric Power by Nanocrystalline Dye Sensitized Solar Cells”, J. Photochem. Photobiol., A 2004, 164, 3. DOI: 10.1016/j.jphotochem.2004.02.023.

145. Yu, Z., Gorlov, M., Boschloo, G., Kloo, L. “Synergistic Effect of N-Methylbenzimidazole and Guanidinium Thiocyanate on the Performance of Dye-Sensitized Solar Cells Based on Ionic Liquid Electrolytes”, J. Phys. Chem. C 2010, 114, 22330. DOI: 10.1021/jp1073686.

146. Wu, J., Hao, S., Lan, Z., Lin, J., Huang, M., Huang, Y., Fang, L., Yin, S., Sato, T. “A Thermoplastic Gel Electrolyte for Stable Quasi-Solid-State Dye-Sensitized Solar Cells”, Adv. Funct. Mater. 2007, 17, 2645. DOI: 10.1002/adfm.200600621.

147. Komiya, R., Han, L., Yamanaka, R., Islam, A., Mitate, T. “Highly efficient quasi-solid state dye-sensitized solar cell with ion conducting polymer electrolyte”, J. Photochem. Photobiol., A 2004, 164, 123. DOI: 10.1016/j.jphotochem.2003.11.015.

148. Huo, Z., Dai, S., Wang, K., Kong, F., Zhang, C., Pan, X., Fang, X. “Nanocomposite gel electrolyte with large enhanced charge transport properties of an I3 /I redox couple for quasi-solid-state dye-sensitized solar cells”, Sol. Energy Mater. Sol. Cells 2007, 91, 1959. doi: 10.1016/j.solmat.2007.08.003.

149. Tennakone, K., Kumara, G., Kumarasinghe, A., Wijayantha, K., Sirimanne, P. M. “A dye-sensitized nano-porous solid-state photovoltaic cell”, Semicond. Sci. Technol. 1995, 10, 1689.

150. O’Regan, B., Lenzmann, F., Muis, R., Wienke, J. “A Solid-State Dye-Sensitized Solar Cell Fabricated with Pressure-Treated P25−TiO2 and CuSCN: Analysis of Pore Filling and IV Characteristics”, Chem. Mater. 2002, 14, 5023. DOI: 10.1021/cm020572d.

151. Lee, B., Stoumpos, C., Zhou, N., Hao, F., Malliakas, C., Yeh, C., Marks, T., Kanatzidis, M., Chang, R. “Air-stable molecular semiconducting iodosalts for solar cell applications: Cs2SnI6 as a hole conductor”, J. Am. Chem. Soc. 2014, 136, 15379. DOI: 10.1021/ja508464w.

152. Xia, J., Masaki, N., Lira-Cantu, M., Kim, Y., Jiang, K., Yanagida, S. “Efficient solid state dye-sensitized solar cells based on an oligomer hole transport material and an organic dye”, J. Am. Chem. Soc. 2008, 130, 1258. DOI: 10.1039/C3TA13646A.

153. Yiming Cao, Yasemin Saygili, Amita Ummadisingu, Joe¨l Teuscher, Jingshan Luo, Norman Pellet, Fabrizio Giordano, Shaik Mohammed Zakeeruddin, Jacques-E. Moser, Marina Freitag, Anders Hagfeldt & Michael Gra¨tzel. “11% efficiency solid-state dye-sensitized solar cells with copper(II/I) hole transport materials”, NATURE COMMUNICATIONS, 2017, 8: 15390. DOI: 10.1038/ncomms15390.

154. A. Kay, M. Grätzel. “Low cost photovoltaic modules based on dye sensitized nanocrystalline titanium dioxide and carbon powder”, Sol. Energy Mater. Sol. Cells, 44 (1996), pp. 99-117. DOI: 10.1016/0927-0248(96)00063-3.

155. K. Hara, Z.-S. Wang, Y. Cui, A. Furube, N. Koumura. “Long-term stability of organic–dye-sensitized solar cells based on an alkyl-functionalized carbazole dye”, Energy Environ. Sci., 2 (2009), pp. 1109-1114. DOI: 10.1039/B907486D.

156. E. Olsen, G. Hagen, S. Eric Lindquist. “Dissolution of platinum in methoxy propionitrile containing LiI/I2”, Sol. Energy Mater. Sol. Cells, 63 (2000), pp. 267-273. DOI: 10.1016/S0927-0248(00)00033-7.

157. Z.X. Shu, S. Bruckenstein. “Iodine adsorption studies at platinum”, J. Electroanal. Chem. Interfacial Electrochem., 317 (1991), pp. 263-277. DOI: 10.1016/0022-0728(91)85019-L.

158. D.C. Johnson. “A study of the adsorption and desorption of iodine and iodide at platinum electrodes in 1.0M sulfuric acid”, J. Electrochem. Soc., 119 (1972), pp. 331-339. DOI: 10.1149/1.2404197.

159. G. Wang, Y. Lin, X. Xiao, X. Li, W. Wang. “X-ray photoelectron spectroscopy analysis of the stability of platinized catalytic electrodes in dye-sensitized solar cells”, Surf. Interface Anal., 36 (2004), pp. 1437-1440. DOI: 10.1002/sia.1905.

160. Yunyoung Noh, Kicheon Yoo, Jae-Yup Kim, Ohsung Song, Min Jae Ko. “Iridium catalyst based counter electrodes for dye-sensitized solar cells”, Current Applied Physics 13 (2013) 1620-1624. DOI: 10.1016/j.cap.2013.06.007.

161. Krishnaiah Mokurala, Anvita Kamble, Parag Bhargava, Sudhanshu Mallick. “RF Sputtered Iridium (Ir) Film as a Counter Electrode for Dye-Sensitized Solar Cells”, Journal of ELECTRONIC MATERIALS, Vol. 44, No. 11, 2015. DOI: 10.1007/s11664-015-3957-4.

162. Jeesoo Seok, Ka Yeon Ryu, Jin Ah Lee, Inyoung Jeong, Nam-Suk Lee, Jeong Min Baik, Joo Gon Kim, Min Jae Ko, Kyungkon Kim, Myung Hwa Kim. “Ruthenium based nanostructures driven by morphological controls as efficient counter electrodes for dye-sensitized solar cells”, Phys. Chem. Chem. Phys., 2015, 17, 3004. DOI: 10.1039/c4cp04506h.

163. Benlin He, Xin Meng, and Qunwei Tang. “Low-Cost Counter Electrodes From CoPt Alloys For Efficient DyeSensitized Solar Cells”, ACS Appl. Mater. Interfaces 2014, 6, 4812−4818. DOI: 10.1021/am405706q.

164. Yanyan Duan, Qunwei Tang, Benlin He, Ru Lia, Liangmin Yu. “Transparent nickel selenide alloy counter electrodes for bifacial dye-sensitized solar cells exceeding 10% efficiency”, Nanoscale, 2014, 6, 12601. DOI: 10.1039/c4nr03900a.

165. Teketel Yohannes and O Inganäs. “Photoelectrochemical studies of the junction between poly[3-(4-octylphenyl)thiophene] and a redox polymer electrolyte”, Sol. En. Mat. and Sol. Cells, 51, 2, 1998, Pg 193-202. DOI: 10.1016/S0927-0248(97)00213-4.

166. Lasse Bay, Keld West, Bjørn Winther-Jensen, Torben Jacobsen. “Electrochemical reaction rates in a dye-sensitised solar cell—the iodide/tri-iodide redox system”, Sol. En. Mat. and Sol. Cells, 90, 3, 2006, pg 341-351. DOI: 10.1016/j.solmat.2005.04.040.

167. J. Pringle, V. Armel, D. MacFarlane. “Electrodeposited PEDOT-on-plastic cathodes for dye-sensitized solar cells”, Chem. Commun.,2010, 46, 5367–5369. DOI: 10.1039/C0CC01400A.

168. R. Trevisan, M. Dobbelin, P. Boix, E. Barea, R. Tena-Zaera, B. Mora-Sero. “PEDOT Nanotube Arrays as High Performing Counter Electrodes for Dye Sensitized Solar Cells. Study of the Interactions Among Electrolytes and Counter Electrodes”, Adv. Energy Mater., 2011, 1, 781–784. DOI: 10.1002/aenm.201100324.

169. Jin Soo Kang, Jin Kim, Jae-Yup Kim, Myeong Jae Lee, Jiho Kang, Yoon Jun Son, Juwon Jeong, Sun Ha Park, Min Jae Ko, Yung-Eun Sung. “Highly Efficient Bifacial Dye-Sensitized Solar Cells Employing Polymeric Counter Electrodes”, ACS Appl. Mater. Interfaces 2018, 10, 10, 8611-8620. DOI: 10.1021/acsami.7b17815.

170. Q. Li, J. Wu, Q. Tang, Z. Lan, P. Li, J. Lin, L. Fan. “Application of microporous polyaniline counter electrode for dye-sensitized solar cells”, Electrochem. Commun., 2008, 10, 1299–1302. DOI: 10.1016/j.elecom.2008.06.029.

171. H. Wang, Q. Feng, F. Gong, Y. Li, G. Zhou, Z. Wang. “In situ growth of oriented polyaniline nanowires array for efficient cathode of

Co(III)/Co(II) mediated dyesensitized solar cell", J. Mater. Chem. A, 2013, 1, 97–104. DOI: 10.1039/c2ta00705c.

172. J. Wu, Y. Li, Q. Tang, G. Yue, J. Lin, M. Huang, L. Meng. "Bifacial dye-sensitized solar cells: A strategy to enhance overall efficiency based on transparent polyaniline electrode", Sci. Rep., 2014, 4, 4028. DOI: 10.1038/srep04028.

173. Jihuai Wu, Zhang Lan, Jianming Lin, Miaoliang Huang, Yunfang Huang, Leqing Fan, Genggeng Luo, Yu Lin, Yimin Xie, Yuelin Wei. "Counter electrodes in dye-sensitized solar cells", Chem. Soc. Rev., 2017, 46, 5975. DOI: 10.1039/c6cs00752j.

174. J. Wu, Q. Li, L. Fan, Z. Lan, P. Li, J. Lin, S. Hao. "High-performance polypyrrole nanoparticles counter electrode for dye-sensitized solar cells", J. Power Sources, 2008, 181, 172–176. DOI: 10.1016/j.jpowsour.2008.03.029.

175. S. Jeon, C. Kim, J. Ko, S. Im. "Spherical polypyrrolenanoparticles as a highly efficient counter electrode for dye-sensitized solar cells", J. Mater. Chem., 2011, 21, 8146–8151. DOI: 10.1039/C1JM10112A.

176. J. Nam, Y. Park, B. Kim, J. Lee. "Enhancement of the efficiency of dye-sensitized solar cell by utilizing carbon nanotube counter electrode", Scr. Mater., 2010, 62, 148–150. DOI: 10.1016/j.scriptamat.2009.10.008.

177. T. Murakami, S. Ito, Q. Wang, M. Nazeeruddin, T. Bessho, I. Cesar, P. Liska, R. Humphry-Baker, P. Comte, P. Pechy, M. Gratzel. "Highly Efficient Dye-Sensitized Solar Cells Based on Carbon Black Counter Electrodes", J. Electrochem. Soc., 2006, 153, A2255–2261. DOI: 10.1149/1.2358087.

178. H. Guo, Y. Zhu, W. Li, H. Zheng, K. Wu, K. Ding, B. Ruan, A. Hagfeldt, T. Ma, M. Wu. "Synthesis of highly effective Pt/carbon fiber composite counter electrode catalyst for dye-sensitized solar cells", Electrochim. Acta, 2015, 176, 997–1000. DOI: 10.1016/j.electacta.2015.07.103.

179. I. Jeon, H. Kim, I. Choi, K. Lim, J. Ko, J. Kim, H. Choi, M. Ju, J. Lee, H. Kim, J.B. Baek. "High-performance dye-sensitized solar cells using edge-halogenated graphene nanoplatelets as counter electrodes", Nano Energy, 2015, 13, 336–345. DOI: 10.1016/j.nanoen.2015.02.037.

180. C. Wu, T. Chang, H. Teng, Y. Lee. “High performance carbon black counter electrodes for dye-sensitized solar cells”, Energy, 2016, 115, 513–518. DOI: 10.1016/j.energy.2016.09.052.

181. M. Wu, X. Lin, T. Wang, J. Qiu, T. Ma. “Low-cost dye-sensitized solar cell based on nine kinds of carbon counter electrodes”, Energy Environ. Sci., 2011, 4, 2308–2315. DOI: 10.1039/C1EE01059J.

182. Xiuting Luo, Yaojia Zhang, Soo Hyung Kim. “Incorporation of Nanostructured Carbon Composite Materials into Counter Electrodes for Highly Efficient Dye-Sensitized Solar Cells”, Nanoscale Res Lett. 2018; 13: 274. doi: 10.1186/s11671-018-2692-1.

183. Sedong Kim,Otgonbayar Dovjuu, Soon-Ho Choi, Hyomin Jeong, Ji-Tae Park. “Photovoltaic Characteristics of Multiwalled Carbon Nanotube Counter-Electrode Materials for Dye-Sensitized Solar Cells Produced by Chemical Treatment and Addition of Dispersant”, Coatings 2019, 9(4), 250; DOI: 10.3390/coatings9040250.

184. Senthilkumar R, Raj SM, Ramakrishnan S, Kumaresan D, Kothurkar NK. “Thermally Reduced Graphene Oxide as a Counter Electrode Material for Dye-Sensitized Solar Cells”, J Nanosci Nanotechnol. 2019 Apr 1; 19 (4): 2158-2165. doi: 10.1166/jnn.2019.16360.

185. C. Yu, Z. Liu, X. Meng, B. Lu, D. Cui, J. Qiu. “Nitrogen and phosphorus dual-doped graphene as a metal-free high-efficiency electrocatalyst for triiodide reduction”, Nanoscale, 2016, 8, 17458–17464. DOI: 10.1039/C6NR00839A.

186. Y. Li, C. Li, M. Yeh, K. Huang, P. Chen, R. Vittal, K. Ho. “Graphite with Different Structures as Catalysts for Counter Electrodes in Dye-sensitized Solar Cells”, Electrochim. Acta, 2015, 179, 211–219. DOI: 10.1016/j.electacta.2015.06.007.

187. R. Kumar, S. Nemala, S. Mallick, P. Bhargava. “High efficiency dye sensitized solar cell made by carbon derived from sucrose”, Opt. Mater., 2017, 64, 401–405. DOI: 10.1016/j.optmat.2017.01.013.

188. Cristina Giordano, Markus Antonietti. “Synthesis of crystalline metal nitride and metal carbide nanostructures by sol—gel chemistry”, Nano Today (2011) 6, 366—380. DOI: 10.1016/j.nantod.2011.06.002.

189. R.S.Ningthoujam, N.S.Gajbhiye. “Synthesis, electron transport properties of transition metal nitrides and applications”, Progress in Materials Science 70 (2015) 50–154. DOI: 10.1016/j.pmatsci.2014.11.004.

190. Anand P. Tiwari, Travis G. Novak, Xiuming Bu, Johnny C. Ho, Seokwoo Jeon. “Layered Ternary and Quaternary Transition Metal Chalcogenide Based Catalysts for Water Splitting”, Catalysts 2018, 8, 551. DOI: 10.3390/catal8110551.

191. M. Wu, X. Lin, Y. Wang, L. Wang, W. Guo, D. Qu, X. Peng, A. Hagfeldt, M. Gratzel, T. Ma. “Economical Pt-Free Catalysts for Counter Electrodes of Dye-Sensitized Solar Cells”, J. Am. Chem. Soc., 2012, 134, 3419–3428. DOI: 10.1021/ja209657v.

192. K. Soo, M. Park, J. Kim, S. Park, Y. Dong, S. Yu, J. Kim, J. Park, J. Choi, J. Lee. “Reactively sputtered nickel nitride as electrocatalytic counter electrode for dye- and quantum dot-sensitized solar cells”, Sci. Rep., 2015, 5, 10450. DOI: 10.1038/srep10450.

193. V. Paranthaman, S. Muthu, P. Alagarsamy, H. Ming, R. Perumalsamy. “Influence of zirconium dioxide and titanium dioxide binders on the photovoltaic performance of dye sensitized solar cell tungsten carbide nanorods based counter electrode”, Electrochim. Acta, 2016, 211, 375–384. DOI: 10.1016/j.electacta.2016.06.057.

194. Abdul Hai Alami, Bilal Rajab, Jehad Abed, Mohammed Faraj, Abdullah Abu Hawili, Hussain Alawadhi. “Investigating various copper oxides-based counter electrodes for dyesensitized solar cell applications”, Energy 174 (2019) 526-533. DOI: 10.1016/j.energy.2019.03.011.

195. M. Wang, A. Anghel, B. Marsan, N. Ha, N. Pootrakulchote, S. Zakeeruddin, M. Gratzel. “CoS supersedes Pt as efficient electrocatalyst for triiodide reduction in dye-sensitized solar cells”, J. Am. Chem. Soc. 131 (2009) 15976. DOI: 10.1021/ja905970y.

196. J. Lin, J. Liao, S. Chou. “Cathodic electrodeposition of highly porous cobalt sulfide counter electrodes for dye-sensitized solar cells”, Electrochim. Acta 56 (2011) 8818. DOI: 10.1016/j.electacta.2011.07.080.

197. C. Kung, H. Chen, C. Lin, K. Huang, R. Vittal, K. Ho. “CoS acicular nanorod arrays for the counter electrode of an efficient dye-sensitized solar cell”, ACS nano 6 (2012) 7016. DOI: 10.1021/nn302063s.

198. S. Hsu, C. Li, H. Chien, R. Salunkhe, N. Suzuki, Y. Yamauchi, K. Ho, K. Wu. “Platinum-free counter electrode comprised of metal-organic-framework (MOF)-derived cobalt sulfide nanoparticles for efficient dye-sensitized solar cells (DSSCs)”, Scientific Reports 4 (2014) 6983. DOI: 10.1038/srep06983.

199. M. Congiu, L. Albano, F. Decker, C. Graeff. “Single precursor route to efficient cobalt sulphide counter electrodes for dye sensitized solar cells”, Electrochim. Acta 151 (2015) 517. DOI: 10.1016/j.electacta.2014.11.001.

200. Jinghao Huo, Min Zheng, Yongguang Tu, Jihuai Wu, Linhua Hub, Songyuan Dai. “A high performance cobalt sulfide counter electrode for dye-sensitized solar cells”, Electrochimica Acta 159 (2015) 166–173. DOI: 10.1016/j.electacta.2015.01.214.

201. Qiongzhe Yu, Yashuai Pang, Qiwei Jiang. “NiS submicron cubes with efficient electrocatalytic activity as the counter electrode of dye-sensitized solar cells”, R. Soc. Open Sci. 5: 180186. DOI: 10.1098/rsos.180186.

202. Xiao Yang, Lei Zhou, Ali Feng, Huaibao Tang, Haijun Zhang, Zongling Ding, Yongqing Ma, Mingzai Wu, Shaowei Jin. “Synthesis of nickel sulfides of different phases for counter electrodes in dye-sensitized solar cells by a solvothermal method with different solvents”, J. Mater. Res., Vol. 29, No. 8, Apr 28, 2014. DOI: 10.1557/jmr.2014.74.

203. Yanyan Duan, Qunwei Tang, Juan Liu, Benlin He, Liangmin Yu. “Transparent Metal Selenide Alloy Counter Electrodes for High-Efficiency Bifacial Dye-Sensitized Solar Cells”, Angew. Chem. Int. Ed. 2014, 53, 1 – 7. DOI: 10.1002/anie.201409422.

204. Jie Yin, Yuqiao Wang, Wenfei Meng, Tianyue Zhou, Baosong Lib, Tao Wei, Yueming Sun. “Honeycomb-like NiCo2S4 nanosheets prepared by a rapid electrodeposition as a counter electrode for dye-sensitized solar cells”, Nanotechnology. 2017 Aug 25; 28 (34): 345403. DOI: 10.1088/1361-6528/aa76b2.

205. Si Yun Khoo, Jianwei Miao, Hong Bin Yang, Ziming He, Kam Chew Leong, Bin Liu, Timothy Thatt Yang Tan. “One-Step Hydrothermal Tailoring of NiCo2S4 Nanostructures on Conducting Oxide Substrates as

an Efficient Counter Electrode in Dye-Sensitized Solar Cells", Adv. Mater. Interfaces 2015, 2, 1500384. DOI: 10.1002/admi.201500384.

206. Liang Chen, Yong Zhou, Hui Dai, Tao Yu, Jianguo Liu, Zhigang Zou. "One-step growth of CoNi2S4 nanoribbonson carbon fibers as platinum-free counter electrodes for fiber-shaped dye-sensitized solar cells with high performance: Polymorph-dependent conversion efficiency", Nano Energy V.11, 2015, Pg. 697-703. DOI: 10.1016/j.nanoen.2014.11.047.

207. Pengkun Wei, Xuemin Li, Jing Li, Jinwu Bai, Chuanjia Jiang, Lu Liu. "A Facile Synthesis of Ternary Nickel Iron Sulfide Nanosphere as Counter Electrode in Dye-Sensitized Solar Cells", Chemistry. 2018 Dec 17; 24 (71): 19032-19037. DOI: 10.1002/chem.201804220.

208. Wenjing Hou, Yaoming Xiao, Gaoyi Han. "Interconnected ternary MIn2S4 (M = Fe, Co, Ni) thiospinels nanosheets array: a type of efficient Pt-free counter electrodes for the dye-sensitized solar cells", Angewandte Chemie 129 (31), June 2017. DOI: 10.1002/ange.201705399.

209. Wenjing Hou, Yaoming Xiao, Gaoyi Han. "The dye-sensitized solar cells based on the interconnected ternary cobalt diindium sulfide nanosheet array counter electrode", Materials Research Bulletin 107 (2018) 204–212. DOI: 10.1016/j.materresbull.2018.07.040.

210. R. Li, M. Zhang, C. Yan, Z. Yao, J. Zhang, P. Wang. "Electron-acceptor-dependent light absorption, excited-state relaxation, and charge generation in triphenylamine dye-sensitized solar cells", ChemSusChem 2015, 8, 97-104. DOI: 10.1002/cssc.201402806.

211. Mannix P.Balanay, Kang Hee Kim, Sang Hee Lee, Dong Hee Kim. "Tuning the photovoltaic parameters of β-substituted porphyrin analogues: An experimental and theoretical approach", J. Photochem. Photobio. A: Chem. 248, (2012), 63–72. DOI: 10.1016/j.jphotochem.2012.08.011.

212. M.J. Frisch, G.W. Trucks, H.B. Schlegel, G.E. Scuseria, M.A. Robb, J.R. Cheeseman,G. Scalmani, V. Barone, G.A. Petersson, H. Nakatsuji, X. Li, M. Caricato, A.V.Marenich, J. Bloino, B.G. Janesko, R. Gomperts, B. Mennucci, H.P. Hratchian, J.V.Ortiz, A.F. Izmaylov, J.L. Sonnenberg, Williams, F. Ding, F. Lipparini, F. Egidi, J.Goings, B. Peng, A. Petrone, T. Henderson, D. Ranasinghe, V.G. Zakrzewski, J. Gao,N. Rega, G. Zheng, W. Liang, M. Hada, M. Ehara, K. Toyota, R. Fukuda, J.Hasegawa, M.

Ishida, T. Nakajima, Y. Honda, O. Kitao, H. Nakai, T. Vreven, K.Throssell,J.A. Montgomery Jr., J.E. Peralta, F. Ogliaro, M.J. Bearpark, J.J. Heyd, E.N. Brothers, K.N. Kudin, V.N. Staroverov, T.A. Keith, R. Kobayashi, J. Normand, K.Raghavachari, A.P. Rendell, J.C. Burant, S.S. Iyengar, J. Tomasi, M. Cossi, J.M.Millam, M. Klene, C. Adamo, R. Cammi, J.W. Ochterski, R.L. Martin, K. Morokuma,O. Farkas, J.B. Foresman, D.J. Fox, Gaussian 16 Rev. A.03. Gaussian, Inc., Wallingford, CT, 2016.

213. R. Dennington, T.A. Kieth, J.M. Millam, GaussView, Version 6, Semichem Inc, Shawnee Mission, KS, 2016.

214. A. Bondarenko, G. Ragoisha, Inverse problem in potentiodynamic electrochemical impedance, in: A.L. Pomerantsev (Ed.), Progress in Chemometrics Research, Nova Science Publishers, New York, 2005, pp. 89–102. DOI: 10.1002/cem.939.

215. A. Garzon-Roman, C. Zuñiga-Islas, E. Quiroga-González. “Immobilization of doped TiO2 nanostructures with Cu or In inside of macroporous silicon using the solvothermal method: Morphological, structural, optical and functional properties”, Ceram. Int., (2019). DOI: 10.1016/j.ceramint.2019.09.082.

216. L. Zhao, J. Wang, Z. Gai, J. Li, J. Liu, J. Wang, C. Wang, X. Wang. “Annealing effects on the structural and dielectric properties of (Nb + In) co-doped rutile TiO2 ceramics”, RSC Adv., 9 (2019) 8364-8368. DOI: 10.1039/C9RA00564A.

217. P. Siriya, W. Tuichai, S. Danwittayakul, N. Chanlek, P. Thongbai. “Surface layer characterizations and sintering time effect on electrical and giant dielectric properties of (In0.05Nb0.05)Ti0.9O2 ceramics”, Ceram. Int., 44 (2018) 7234-7239. DOI: 10.1016/j.ceramint.2018.01.174.

218. H. Yu, F. Chen, L. Ye, H. Zhou, T. Zhao. “Enhanced photocatalytic degradation of norfloxacin under visible light by immobilized and modified In2O3/TiO2 photocatalyst facilely synthesized by a novel polymeric precursor method”, J. Mater. Sci., 54 (2019) 10191-10203. DOI: 10.1007/s10853-019-03636-z.

219. V. Kumaravel, S. Rhatigan, S. Mathew, J. Bartlett, M. Nolan, S.J. Hinder, P.K. Sharma, A. Singh, J.A. Byrne, J. Harrison, S.C. Pillai. “Indium-Doped TiO2 Photocatalysts with High-Temperature Anatase

Stability", J. Phys. Chem. C, 123 (2019) 21083-21096. DOI: 10.1021/acs.jpcc.9b06811.

220. F.S. Al mashary, S. de Castro, A.F. da Silva, J.F. Felix, M.R. Piton, H.V.A. Galeti, A. De Giovanni Rodrigues, Y.G. Gobato, N. Al Saqri, M. Henini, M.M. Al huwayz, A.M. Albadri, A.Y. Alyamani, H.A. Albrithen, S.A. Alhusaini, K.M. Aljaber, A.Z. Alanazi, F.S. Alghamdi. "Effect of growth techniques on the structural, optical and electrical properties of indium doped TiO2 thin films", J. Alloys Compd., 766 (2018) 194-203. DOI: 10.1016/j.jallcom.2018.06.360.

221. A.M. Bakhshayesh, N. Farajisafiloo. "Efficient dye-sensitised solar cell based on uniform In-doped TiO2 spherical particles", Appl. Phys. A, 120 (2015) 199-206. DOI: 10.1007/s00339-015-9150-z.

222. R.J. Beula, S. Devadason, B. Vidhya. "Incorporation of indium in TiO2-based photoanodes for enhancing the photovoltaic conversion efficiency of dye-sensitized solar cells", Appl. Nanosci., 8 (2018) 1389-1397. DOI: 10.1007/s13204-018-0819-4.

223. X. Sun, Q. Zhang, Y. Liu, N. Huang, P. Sun, T. Peng, T. Peng, X.-Z. Zhao. "Photovoltaic performance improvement of dye-sensitized solar cells through introducing In-doped TiO2 film at conducting glass and mesoporous TiO2 interface as an efficient compact layer", Electrochim. Acta, 129 (2014) 276-282. DOI: 10.1016/j.electacta.2014.02.110.

224. S.-M. Chang, W.-S. Liu. "Surface doping is more beneficial than bulk doping to the photocatalytic activity of vanadium-doped TiO2", Appl. Catal., B, 101 (2011) 333-342. DOI: 10.1016/j.apcatb.2010.09.035.

225. C.Y. Xu, P.X. Zhang, L. Yan. "Blue shift of Raman peak from coated TiO2 nanoparticles", J. Raman Spectrosc., 32 (2001) 862-865. DOI: 10.1002/jrs.773.

226. N. Kopidakis, N.R. Neale, A.J. Frank. "Effect of an adsorbent on recombination and band-edge movement in dye-sensitized TiO2 solar cells: evidence for surface passivation", J. Phys. Chem. B, 110 (2006) 12485-12489. DOI: 10.1021/jp0607364.

227. N. Thomas, D. Bechet, P. Becuwe, L. Tirand, R. Vanderesse, C. Frochot, F. Guillemin, M. Barberi-Heyob. "Peptide-conjugated chlorin-type photosensitizer binds neuropilin-1 in vitro and in vivo", J. Photochem. Photobiol., B, 96 (2009) 101-108. DOI: 10.1016/j.jphotobiol.2009.04.008.

228. P.J. Cameron, L.M. Peter, S. Hore. “How important is the back reaction of electrons via the substrate in dye-sensitized nanocrystalline solar cells?”, J. Phys. Chem. B, 109 (2005) 930-936. DOI: 10.1021/jp0405759.

229. A. Zaban, M. Greenshtein, J. Bisquert. “Determination of the electron lifetime in nanocrystalline dye solar cells by open-circuit voltage decay measurements”, ChemPhysChem, 4 (2003) 859-864. DOI: 10.1002/cphc.200200615.

230. K. Fredin, J. Nissfolk, G. Boschloo, A. Hagfeldt. “The influence of cations on charge accumulation in dye-sensitized solar cells”, J. Electroanal. Chem., 609 (2007) 55-60. DOI: 10.1016/j.jelechem.2007.05.013.

231. J. Bisquert, A. Zaban, P. Salvador. “Analysis of the mechanisms of electron recombination in nanoporous TiO2 dye-sensitized solar cells. Nonequilibrium steady-state statistics and interfacial electron transfer via surface states”, J. Phys. Chem. B, 106 (2002) 8774-8782. DOI: 10.1021/jp026058c.

232. Arthur J. Frank, Nikos Kopidakis, Jao van de Lagemaat. “Electrons in nanostructured TiO2 solar cells: transport, recombination and photovoltaic properties”, Coord. Chem. Rev., V.248, Iss.13–14, 2004, Pg. 1165-1179. DOI: 10.1016/j.ccr.2004.03.015.

233. J. van de Lagemaat and A. J. Frank. “Effect of the Surface-State Distribution on Electron Transport in Dye-Sensitized TiO2 Solar Cells: Nonlinear Electron-Transport Kinetics”, J. Phys. Chem. B 2000, 104, 18, 4292-4294. DOI: 10.1021/jp000836o.

234. David Cahen, Gary Hodes, Michael Grätzel, Jean François Guillemoles and Ilan Riess. “Nature of Photovoltaic Action in Dye-Sensitized Solar Cells”, J. Phys. Chem. B 2000, 104, 9, 2053-2059. DOI: 10.1021/jp993187t.

235. Jing Zhang, Jiangwei Feng, Yang Hong, Yuejin Zhu and Liyuan Han. “Effect of different trap states on the electron transport of photoanodesin dye sensitized solar cells”, J. of Power Sources, V.257, 2014, Pg. 264-271. DOI: 10.1016/j.jpowsour.2014.01.086.

236. C.B. Storm, A.H. Corwin, R.R. Arellano, M. Martz, R. Weintraub. “Stability Constants of Magnesium Porphyrin-Pyridine Complexes.

Solvent and Substituent Effects", J. Am. Chem. Soc. 88 (1966) 2525. DOI: 10.1021/ja00963a030.

237. J. Liu, X. Yang, L. Sun. "Axial anchoring designed silicon–porphyrin sensitizers for efficient dye-sensitized solar cells", Chem. Commun. 49 (2013) 11785. DOI: 10.1039/C3CC46581K.

238. K. Takumi, F. Jun-ichi, N. Jotaro, U. Satoshi, K. Takaya, S. Hiroshi. "Visible to Near-Infrared Photoelectric Conversion in a Dye-Sensitized Solar Cell Using Ru(II) Porphyrin with Azopyridine Axial Ligands", Jpn. J. Appl. Phys. 51 (2012) 10NE02. DOI: 10.1143/JJAP.51.10NE02.

239. M. K. Nazeeruddin, R. Humphry-Baker, M. Grätzel, M. K. Nazeeruddin, R. Humphry-Baker, M. Grätzel, B. A. Murrer. "Efficient near IR sensitization of nanocrystalline TiO2 films by ruthenium phthalocyanines", Chem. Commun. (1998) 719. DOI: 10.1039/A708834E.

240. M. Yanagisawa, F. Korodi, J. He, L. Sun, V. Sundström, B. Åkermark. "Ruthenium phthalocyanines with axial carboxylate ligands: Synthesis and function in solar cells based on nanocrystalline TiO2", J. Porphyrins Phthalocyanines 06 (2002) 217. DOI: 10.1142/S1088424602000257.

241. V. Shklover, Y.E. Ovchinnikov, L.S. Braginsky, S.M. Zakeeruddin, M. Grätzel. "Structure of Organic/Inorganic Interface in Assembled Materials Comprising Molecular Components. Crystal Structure of the Sensitizer Bis[(4,4'-carboxy-2,2'-bipyridine)(thiocyanato)]ruthenium(II)", Chem. Mater. 10 (1998) 2533. DOI: 10.1021/cm980303g.

242. Ryuzi Katoh, Motohiro Kasuya, Satoshi Kodate, Akihiro Furube, Nobuhiro Fuke, Naoki Koide. "Effects of 4-tert-Butylpyridine and Li Ions on Photoinduced Electron Injection Efficiency in Black-Dye-Sensitized Nanocrystalline TiO2 Films", J. Phys. Chem. C 2009, 113, 48, 20738-20744. DOI: 10.1021/jp906190a.

243. A. Zaban, O.I. Mićić, B.A. Gregg, A.J. Nozik. "Photosensitization of Nanoporous TiO2 Electrodes with InP Quantum Dots", Langmuir 14 (1998) 3153. DOI: 10.1021/la9713863.

244. B. Lee, D.B. Buchholz, R.P.H. Chang. "An all carbon counter electrode for dye sensitized solar cells", Energy Environ. Sci., 5 (2012), pp. 6941-6952. DOI: 10.1039/C2EE02950B.

245. P. Ma, W. Lu, X. Yan, W. Li, L. Li, Y. Fang, X. Yin, Z. Liu, Y. Lin. “Heteroatom tri-doped porous carbon derived from waste biomass as Pt-free counter electrode in dye-sensitized solar cells”, RSC Adv., 8 (2018), pp. 18427-18433. DOI: 10.1039/C8RA02575D.

246. P. Hasin, V. Amornkitbamrung, N. Chanlek. “Economical nanocomposites of cobalt or nickel species and polyaniline-derived N-doped mesoporous carbons for dye-sensitized solar cells as counter electrodes”, J. Catal., 351 (2017), pp. 19-32. DOI: 10.1016/j.jcat.2017.03.021.

247. M. Bagavathi, A. Ramar, R. Saraswathi. “Fe3O4–carbon black nanocomposite as a highly efficient counter electrode material for dye-sensitized solar cell”, Ceram. Int., 42 (2016), pp. 13190-13198. DOI: 10.1016/j.ceramint.2016.05.111.

248. S. Gnanasekar, P. Kollu, S.K. Jeong, A.N. Grace. “Pt-free, low-cost and efficient counter electrode with carbon wrapped VO2(M) nanofiber for dye-sensitized solar cells”, Sci. Rep., 9 (2019), p. 5177. DOI: 10.1038/s41598-019-41693-1.

249. C. Yu, Z. Liu, Y. Chen, X. Meng, M. Li, J. Qiu. “CoS nanosheets-coupled graphene quantum dots architectures as a binder-free counter electrode for high-performance DSSCs”, Sci. China Mater., 59 (2016), pp. 104-111. DOI: 10.1007/s40843-016-0121-2.

250. L. Sun, Y. Li, Y. Dan, X. Lu, X. Li, F. Wang, X. Han, Y. Zhang. “Self-assembled composite thin film counter electrode of cobalt sulfide/functionalized graphene for dye-sensitized solar cells”, Thin Solid Films, 679 (2019), pp. 8-14. DOI: 10.1016/j.ssi.2018.11.001.

251. K. Dai, D. Li, L. Lu, Q. Liu, J. Lv, G. Zhu. “Facile synthesis of a reduced graphene oxide/cobalt sulfide hybrid and its electrochemical capacitance performance”, RSC Adv., 4 (2014), pp. 29216-29222. DOI: 10.1039/C4RA04103H.

252. B. Xu, L. Pan, Q. Zhu. “Synthesis of Co3S4 nanosheets and their superior supercapacitor property”, J. Mater. Eng. Perform., 25 (2016), pp. 1117-1121. DOI: 10.1007/s11665-016-1955-1.

253. J. Yu, H. Wan, J. Jiang, Y. Ruan, L. Miao, L. Zhang, D. Xia, K. Xu. “Activation mechanism study of dandelion-like Co9S8 nanotubes in

supercapacitors", J. Electrochem. Soc., 161 (2014), pp. A996-A1000. DOI: 10.1149/2.053406jes.

254. L.-L. Feng, M. Fan, Y. Wu, Y. Liu, G.-D. Li, H. Chen, W. Chen, D. Wang, X. Zou. "Metallic Co9S8 nanosheets grown on carbon cloth as efficient binder-free electrocatalysts for the hydrogen evolution reaction in neutral media", J. Mater. Chem. A Mater. Energy Sustain., 4 (2016), pp. 6860-6867. DOI: 10.1039/C5TA08611F.

255. R.B. Rakhi, N.A. Alhebshi, D.H. Anjum, H.N. Alshareef. "Nanostructured cobalt sulfide-on-fiber with tunable morphology as electrodes for asymmetric hybrid supercapacitors", J. Mater. Chem. A, 2 (2014), pp. 16190-16198. DOI: 10.1039/C4TA03341H.

256. Q. Chen, H. Li, C. Cai, S. Yang, K. Huang, X. Wei, J. Zhong. "In situ shape and phase transformation synthesis of Co3S4 nanosheet arrays for high-performance electrochemical supercapacitors", RSC Adv., 3 (2013), pp. 22922-22926. DOI: 10.1039/C3RA44237C.

257. R. Ramachandran, M. Saranya, C. Santhosh, V. Velmurugan, B.P.C. Raghupathy, S.K. Jeong, A.N. Grace. "Co9S8 nanoflakes on graphene (Co9S8/G) nanocomposites for high performance supercapacitors", RSC Adv., 4 (2014), pp. 21151-21162. DOI: 10.1039/C4RA01515K.

258. M. Kruk, M. Jaroniec. "Gas adsorption characterization of ordered organic−inorganic nanocomposite materials", Chem. Mater., 13 (2001), pp. 3169-3183. DOI: 10.1021/cm0101069.

259. K.S.W. Sing. "Reporting physisorption data for gas/solid systems with special reference to the determination of surface area and porosity (Recommendations 1984)", Pure Appl. Chem., 57 (1985), p. 603. DOI: 10.1351/pac198557040603.

260. Y. Tian, C. Hu, Q. Wu, X. Wu, X. Li, M. Hashim. "Investigation of the fill factor of dye-sensitized solar cell based on ZnO nanowire arrays", Appl. Surf. Sci., 258 (2011), pp. 321-326. DOI: 10.1016/j.apsusc.2011.08.058.

261. X. Zhang, S.-T. Wang, Z.-S. Wang. "Effect of metal-doping in TiO2 on fill factor of dye-sensitized solar cells", Appl. Phys. Lett., 99 (2011), Article 113503. DOI: 10.1063/1.3635788.

262. Dinah Punnoose, Hee-Je Kim, CH.S.S. Pavan Kumar, S. Srinivasa Rao, Chandu V.V.M. Gopi, Sang-Hwa Chung. “Highly catalytic nickel sulfide counter electrode for dye-sensitizedsolar cells”, J. Photochem. Photobiol. A, V.306, 2015, Pg. 41-46. DOI: 10.1016/j.jphotochem.2015.03.015.

263. Gentian Yue, Jihuai Wu, Jeng-Yu Lin, Yaoming Xiao, Sheng-Yen Tai, Jianming Lin, Miaoliang Huang, Zhang Lan. “A counter electrode of multi-wall carbon nanotubes decoratedwith tungsten sulfide used in dye-sensitized solar cells”, Carbon V. 55, 2013, Pg. 1-9. DOI: 10.1016/j.carbon.2012.10.045.

264. Yue, G., Li, F., Yang, G. et al. “Efficient Nickel Sulfide and Graphene Counter Electrodes Decorated with Silver Nanoparticles and Application in Dye-Sensitized Solar Cells”, Nanoscale Res Lett 11, 239 (2016). DOI: 10.1186/s11671-016-1456-z.

265. J. Theerthagiri, R. A. Senthil, M. H. Buraidah, J. Madhavan, A. K. Arof and Muthupandian Ashokkumar. “One-step electrochemical deposition of Ni1−xMoxS ternary sulfides as an efficient counter electrode for dye-sensitized solar cells”, J. Mater. Chem. A, 2016,4, 16119-16127. DOI: 10.1039/C6TA04405K.

266. Jeng-Yu Lin, Shu-Wei Chou. “Highly transparent NiCo2S4 thin film as an effective catalyst toward triiodide reduction in dye-sensitized solar cells”, El.chem. Comm. 37: 11–14, 2013. DOI: 10.1016/j.elecom.2013.09.027.

267. Xiaojia Zheng, Jiahao Guo, Yantao Shi, Fengqiang Xiong, Wen-Hua Zhang, Tingli Ma and Can Li. “Low-cost and high-performance CoMoS4 and NiMoS4 counter electrodes for dye-sensitized solar cells”, Chem. Commun., 2013,49, 9645-9647. DOI: 10.1039/c3cc45064c.

268. L. Chen, et al. “Using natural language processing to extract clinically useful information from Chinese electronic medical records”, Mater. Lett., 235 (2019), p. 6. DOI: 10.1016/j.ijmedinf.2019.01.004.

269. N. Papageorgiou, W.F. Maier, M. Grätzel. “An iodine/triiodide reduction electrocatalyst for aqueous and organic media”, J. Electrochem. Soc., 144 (1997) 876-884. DOI: 10.1149/1.1837502.

270. Zhiqian Hou, Jianping Long, Chaozhu Shu, Ranxi Liang, Jiabao LiXin Liao. “Two-dimensional spinel CuCo2S4 nanosheets as high efficiency cathode catalyst for lithium-oxygen batteries”, J.All. and Comp., V 798, 2019, Pg. 560-567. DOI: 10.1016/j.jallcom.2019.05.131.

271. Jianhua Tang, Yuancai Ge, Jianfeng Shen and Mingxin Ye. “Facile synthesis of CuCo2S4 as a novel electrode material for ultrahigh supercapacitor performance”, Chem. Commun., 2016, 52, 1509-1512. DOI: 10.1039/C5CC09402J.

272. Minglong Lu , Dr. Xia Cui, Dr. Bo Song, Hongzhen Ouyang, Kunliang Wang, Prof. Yuqiao Wang. “Studying the Effect of CuCo2S4 Morphology on the Oxygen Evolution Reaction using a Flexible Carbon Cloth Substrate”, Chem.Electro.Chem.2020, 7, 1-5. DOI: 10.1002/celc.201902128.

273. Kiran Soni, Meenakshi Chauhan and Sasanka Deka. “Hydrothermally Synthesized CuCo2S4 Nanosheets as an Easily Accessible and Convenient Heterogeneous Catalyst for the Sonogashira Cross-Coupling Reactions”, Front. Mater. 6: 273. DOI: 10.3389/fmats.2019.00273.

274. Amare Aregahegn Dubale, Andebet Gedamu Tamirat, Hung-Ming Chen, Taame Abraha Berhe, Chun-Jern Pan, Wei-Nien Su and Bing-Joe Hwang. “A highly stable CuS and CuS–Pt modified Cu2O/CuO heterostructure as an efficient photocathode for the hydrogen evolution reaction”, J. Mater. Chem. A, 2016, 4, 2205-2216. DOI: 10.1039/c5ta09464j.

275. Haiguan Yang, Junqi Zha, Peng Zhang, Yuhao Xiong, Linjing Sua and Fanggui Ye. “Sphere-like CoS with nanostructures as peroxidase mimics for colorimetric determination of H2O2 and mercury ions”, RSC Adv., 2016, 6, 66963-66970. DOI: 10.1039/c6ra16619a.

276. Liang Chen, Yinze Zuo, Yu Zhang and Yanmin Gao. “Facile Synthesis of Ultrathin CuCo2S4 Nanosheets for HighPerformance Supercapacitors”, Int. J. Electrochem. Sci., 13 (2018) 1343 – 1354. DOI: 10.20964/2018.02.48.

277. Mengran Wang, Yanqing Lai, Jing Fang, Furong Qin, Zhian Zhang, Jie Lia and Kai Zhang. “Hydrangea-like NiCo2S4 hollow microsphere as an advanced bifunctional electrocatalyst for aqueous

metal/air batteries”, Catal. Sci. Technol., 2016, 6, 434-437. DOI: 10.1039/C5CY01656H.

APPENDICES

A. Appendices for Chapter 5

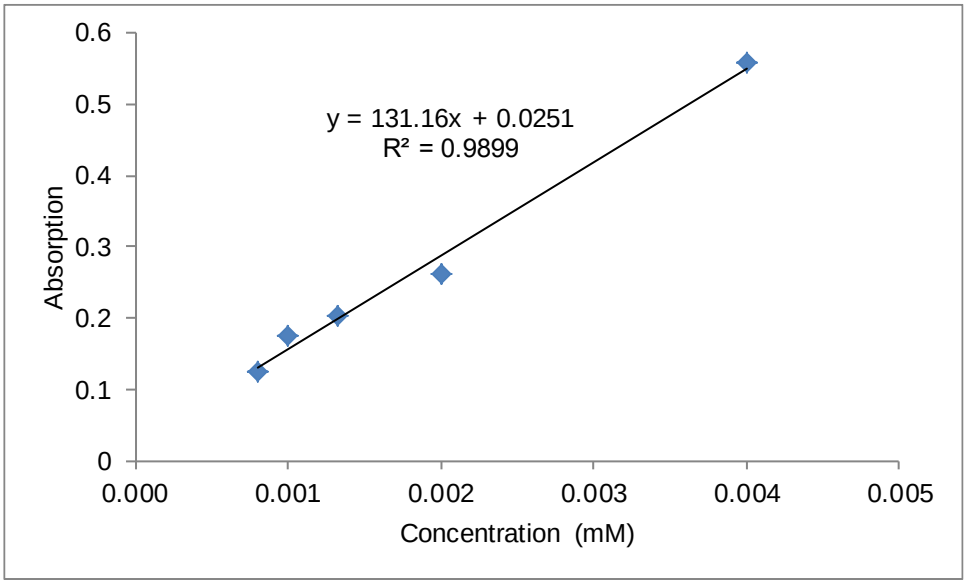

Figure A. 1 Calibration curve of UV-Vis absorption of ZnP in desorption solution

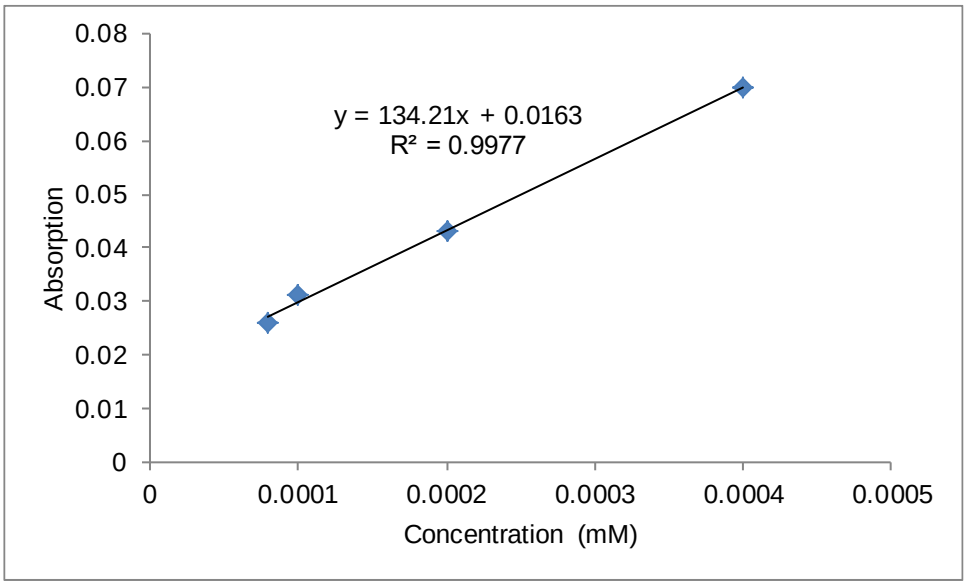

Figure A. 2 Calibration curve of UV-Vis absorption of ZnP:biPy (1:0.5) in desorption solution

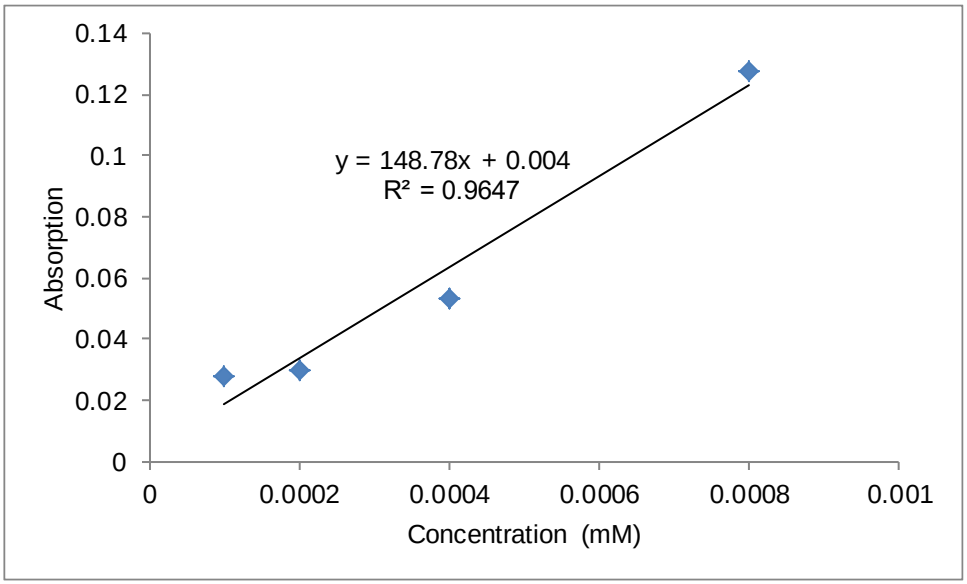

Figure A. 3 Calibration curve of UV-Vis absorption of ZnP:biPy (1:1) in desorption solution

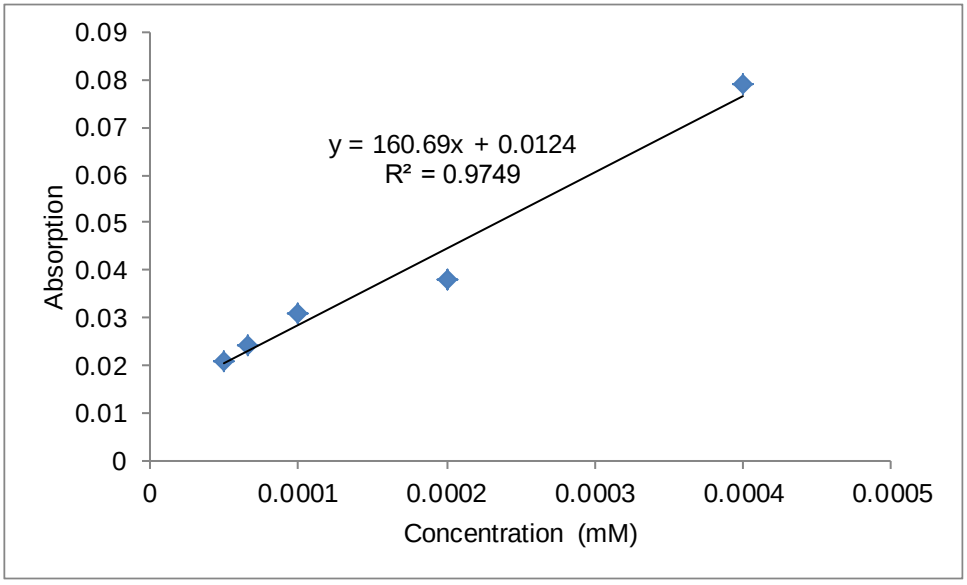

Figure A. 4 Calibration curve of UV-Vis absorption of ZnP:biPy (1:2) in desorption solution

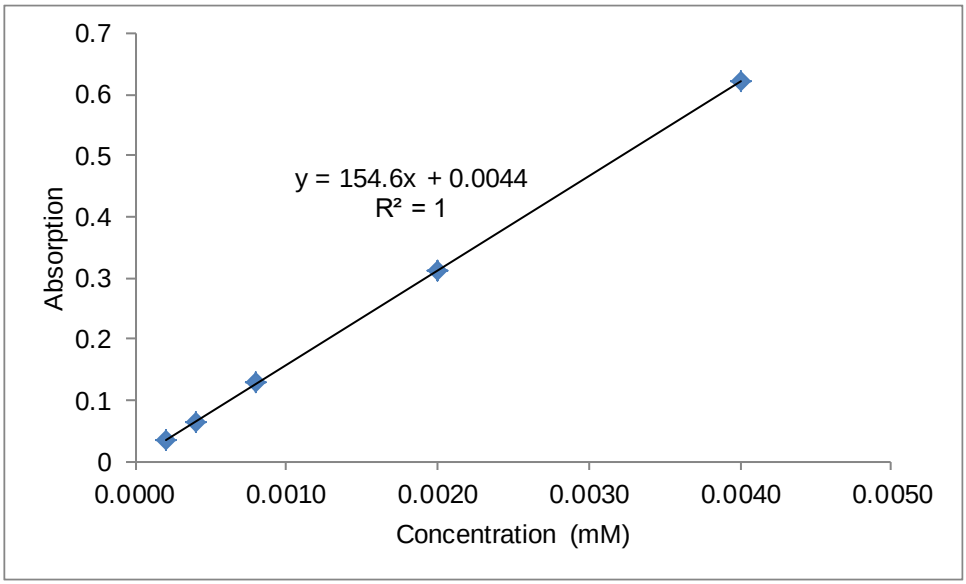

Figure A. 5 Calibration curve of UV-Vis absorption of ZnP:Py (1:0.5) in desorption solution

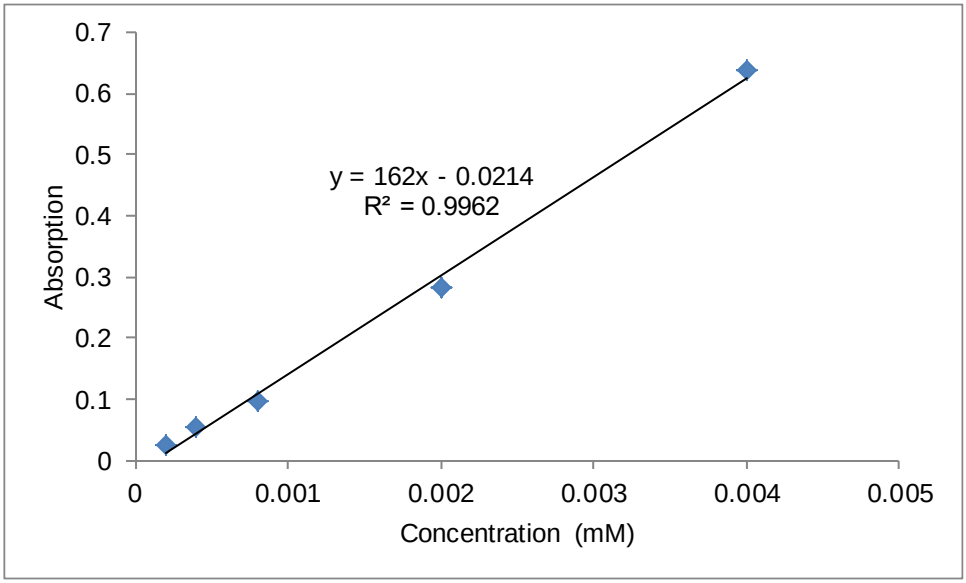

Figure A. 6 Calibration curve of UV-Vis absorption of ZnP:Py (1:1) in desorption solution

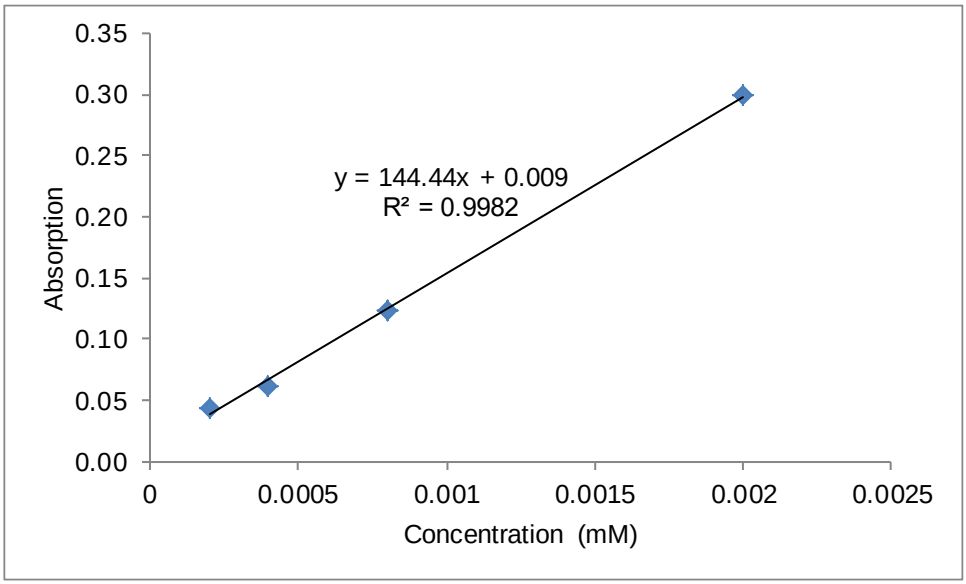

Figure A. 7 Calibration curve of UV-Vis absorption of ZnP:Py (1:2) in desorption solution

B. Appendices for Section 6.1

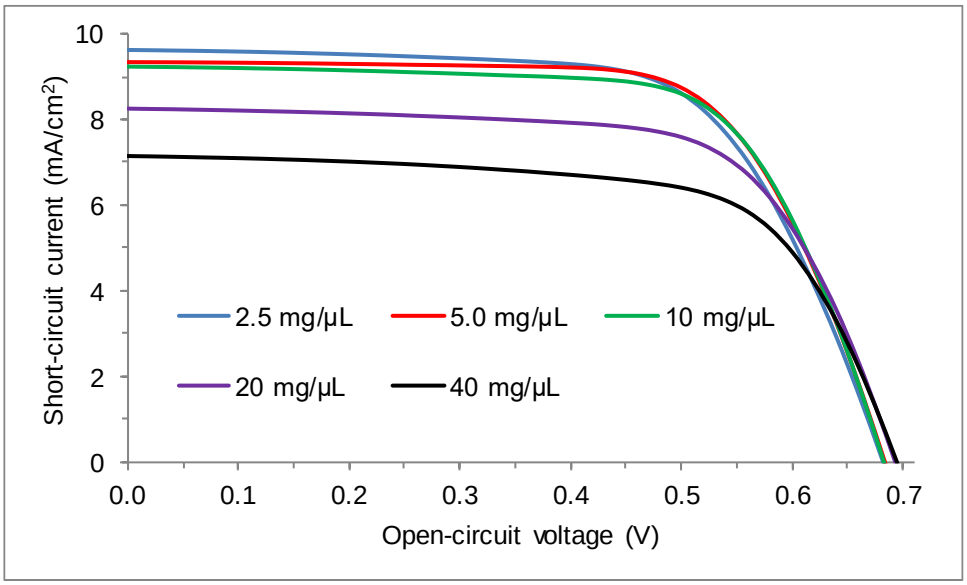

Figure B. 1 I-V curves of dye-sensitized solar cells with OFC@Co_xS_y-300 CE. WE – FTO / compact TiO_2 / opaque TiO_2 (Sigma Aldrich); Dye - N719; Electrolyte – iodide / triiodide electrolyte S104 (DN-OD05) [4];

Table B. 1 Photovoltaic parameters of dye-sensitized solar cells with OFC@CoxSy-300 CE. WE – FTO / compact TiO_2 / opaque TiO_2 (Sigma Aldrich); Dye - N719; Electrolyte – iodide / triiodide electrolyte S104 (DN-OD05) [4];

Concentration (mg/µL)	Eff (%)	Voc (V)	Jsc (mA/cm^2)	FF
2.5	4.31±0.03	0.68±0.00	9.63±0.07	0.66±0.01
5.0	4.39±0.07	0.68±0.00	9.34±0.18	0.69±0.00
10.0	4.34±0.10	0.68±0.00	9.24±0.18	0.69±0.00
20.0	3.85±0.06	0.70±0.00	8.26±0.11	0.67±0.01
40.0	3.30±0.03	0.70±0.00	7.15±0.08	0.66±0.00